UNIVERSITY OF CALIFORNIA, SAN DIEGO

Measurements of Primordial Deuterium and Lyman-Alpha Forest Evolution with High-Resolution Quasar Spectroscopy

A dissertation submitted in partial satisfaction of the
requirements for the degree of Doctor of Philosophy

in

Physics

by

Scott Matthew Gustafson

Committee in charge:

Professor David Tytler, Chair
Professor Farhat Beg
Professor Brian Keating
Professor Michael Norman
Professor Justin Roberts

2016

The Dissertation of Scott Matthew Gustafson is approved and is acceptable in quality and form for publication on microfilm and electronically:

Chair

University of California, San Diego

2016

EPIGRAPH

Scientific progress is the discovery of a more and more comprehensive simplicity...The previous successes give us confidence in the future of science: we become more and more conscious of the fact that the universe is cognizable.

Albert Einstein

TABLE OF CONTENTS

LIST OF FIGURES

LIST OF TABLES

ACKNOWLEDGEMENTS

I would like to acknowledge Professor David Tytler for his support, insight and helpful criticisms of my work and to the other members of my doctoral committee: Professors Brian Keating, Michael Norman, Farhat Beg and Justin Roberts for their time and energy in being part of my doctoral committee.

In addition to David Tytler, gratitude is due to John O'Meara and David Kirkman who performed observations for much of the data used in this dissertation and most of the data reduction for Chapter 6. The author extensively fitting software written by David Kirkman, without which much of this work would not have been possible.

Significant personal gratitude is due to the following persons in no particular order: To my family and to Annie Pham for much needed friendship and emotional support. To Chris Antonov for his friendship and challenging advice. To Eoin Moore for important discussions about life beyond physics. To my friends from choir and the Newman Center at large for being a supportive community, each deserving thanks in their own way. In no particular order: to Chris Chan, Maria Florendo, Gaby Perdomo, Dr. Robert Won, Coralys Munoz, Jennifer Kuo, Earl Lozada, C. Joshua Sykes, Vincent Fung, David Woo, Hanna Youngwirth, Tim Wiryaman, Seung-Keun Martinez, Sophia Barron, Vivian and Lillian Sun, Tammy Nguyen, Dr. Chris Villangco, Dr. Michael Conley, Ratnaganadi Paramita, Dr. Aaron Day. To Lauro Minimo and Neal Wilkinson for their mentoring and for providing an ear to listen and words of advice on life. Finally to all of those whose names I have forgotten to mention here.

The author wishes to recognize and acknowledge the very significant cultural role and reverence that the summit of Mauna Kea has always had within the indigenous Hawaiian community. We are most fortunate to have the opportunity

to conduct observations from this mountain.

The data presented herein were obtained at the W.M. Keck Observatory, which is operated as a scientific partnership among the California Institute of Technology, the University of California and the National Aeronautics and Space Administration. The Observatory was made possible by the generous financial support of the W.M. Keck Foundation.

Chapter 3 is adapted from work being prepared for publication under the working title *The Deuterium abundance in pristine gas towards QSO J1201+0116 : new evidence that we are observing the primordial D/H abundance*. The author of this dissertation is the primary author and David Tytler is co-author.

Chapter 4 is adapted from work being prepared for publication under the working title *The primordial Deuterium abundance in gas towards QSO J0744+2059*. The author of this dissertation is the primary author and David Tytler is co-author.

Chapter 6 is adapted from work being prepared for publication under the working title *New Statistics of the Lyα forest towards 25 Quasar Absorption Lines*. This work uses data first presented in Kirkman et al. (2005) and continua fit by four undergraduate researchers, discussed therein. The author of this dissertation is the primary author and David Tytler is co-author.

VITA

2008–2010	Research Assistant, Department of Physics University of California, San Diego
2010	Bachelor of Science, University of California, San Diego
2010–2016	Teaching Assistant, Department of Physics University of California, San Diego
2012	Master of Science, University of California, San Diego
2010–2016	Graduate Research Assistant, Department of Physics University of California, San Diego
2015, 2016	Associate in Teaching, Department of Physics University of California, San Diego
2016	Doctor of Philosophy, University of California, San Diego

FIELDS OF STUDY

Major Field: Physics (Observational Astrophysics & Cosmology)

ABSTRACT OF THE DISSERTATION

Measurements of Primordial Deuterium and Lyman-Alpha Forest Evolution with High-Resolution Quasar Spectroscopy

by

Scott Matthew Gustafson

Doctor of Philosophy in Physics

University of California, San Diego, 2016

Professor David Tytler, Chair

A precise determination of the light-element abundances produced during the epoch of Big Bang Nucleosynthesis (BBN) is an important probe of the early universe. The Deuterium-Hydrogen abundance ratio (D/H) is of particular importance due to its sensitivity to the cosmological baryon density, its use as a constraint of non-standard BBN scenarios and the fact that Deuterium is not created outside of BBN, but destroyed inside of stars at a predictable rate, so any Deuterium observed in interstellar or intergalactic gas is primordial. Due to the difficulty of measurements and relative rarity of appropriate conditions required to

observe D in quasar absorption systems, there are only 15 published measurements of the primordial D/H in literature. Here we examine the primordial Deuterium-to-Hydrogen abundance ratio using high-resolution optical spectroscopy of diffuse gas towards two quasars. We measure D I towards the bright Quasar J1201+0116 at moderate redshift ($z = 2.98$) in a Lyman-Limit system (N=$10^{17.41}$cm^{-2}) which exhibits very low metal content indicating pristine conditions ([Si/H]=-3.3 ± 0.8). This value, 10^5D/H=2.50 ± 0.18 is in complete agreement with D/H from the CMB and theory. We measure D I in one component of DLA towards quasar J0744+2059 (N=$10^{20.8}$cm^{-2}) and measure D/H to be 2.359 ± 0.095 —2σ lower than D/H from theory and the CMB. Additionally, we present measurements on the Lyα forest towards 25 high-resolution QSO. The statistics we report are suitable for comparison to simulations, which are the primary means of extracting physical information from the Intergalactic Medium.

Introduction

When the first measurements of the Deuterium to Hydrogen ratio (D/H) were first reported (Tytler et al., 1996) it was used to measure the baryon density of the universe, describing the amount of normal or *baryonic* matter in the universe, which stems from the fact that there was more matter than antimatter in the early universe. The baryon density was later independently measured by the subsequent studies of the Cosmic Microwave Background (CMB), showing good agreement (Hinshaw et al., 2013; Planck Collaboration, 2015). Estimates of cosmological parameters have continued to improve and Deuterium continues to be an important tool, especially as a constraint for non-standard cosmologies, since the nuclear reactions responsible for initially creating Deuterium (and Helium and Lithium) are sensitive to the cosmic expansion rate during the epoch of Big Bang Nucleosynthesis (BBN).

This chapter introduces preliminary material to the reader, providing a broad overview of the scientific goals of this dissertation as well as a primer for absorption lines. The goal of the preliminary information in this introduction is to motivate extragalactic Deuterium measurements as a cosmological tool and provide a brief primer of absorption lines. Portions of this introduction adapt material presented in relevant texts and reviews (Bechtold, 2001; Dodelson, 2003; Steigman, 2012), so for more complete detail and a more lucid presentation please see them.

In Chapter 1, we present our methods of observation and processing raw

data from the telescope into data suitable for high-precision spectroscopic measurements. In addition to standard methods, we develop a new technique for correcting wavelength errors thought to relate of object positioning in the slit of the spectrograph we use. We also develop a method to correct residual sky subtraction errors, which appear as residual flux in saturated line-cores, which should average to zero.

In Chapter 2, we report on model fitting methods, in which we now extract scientific information from HIRES spectra. We first fit the unabsorbed continuum level, which describes the spectrum of the light incident to the systems of diffuse gas we study. We then fit absorption lines using Voigt Profiles. To determine errors, we developed a method of randomly inputing continua and absorption parameter values to sample the parameter space of models which fit our data.

In Chapter 3, we present our measurements of a system of gas exhibiting deuterium towards quasar J1201+0116. This system has one of the lowest H I column densities and is one of the most metal poor in D/H literature, but yields a value in good agreement to theory and the CMB.

In Chapter 4, we perform measurements of Deuterium towards another quasar, J0744+2059. Conversely, this system exhibits a damped Lyman-α with the highest H I column density in D/H literature, allowing for a very precise determination of D/H due to its extended Lyα damping wings, matching the selection criteria discussed in Cooke et al. (2014), yet yields a D/H 2σ lower than the CMB. It is not clear if this discrepancy is real or due to a yet unaddressed measurement error.

In Chapter 5, We discuss our findings in light of D/H literature. The two objects reported in this dissertation, in addition to those of other authors (Riemer-Sørensen et al., 2015; Balashev et al., 2016) question whether the selection criteria

presented by Cooke et al. (2014) are, in fact, helpful in determining the accuracy of D/H measurements.

Finally, in Chapter 6, we report on our measurements on the Lyα forest towards a sample of 25 QSOs. The statistics we report are intended to be used as constraints on simulations of the Lyα forest .

A Time Line of the Big Bang and the Evolution of Matter

Quantum field theory holds that for every particle, there should be a corresponding antiparticle with identical mass and lifetime, but opposite charge, which mutually annihilate, releasing energy and radiation upon contact. Quarks and anti-quarks in the early universe thus mutually annihilated to produce photons, however the fact that matter remains suggests an initial over-abundance of matter over antimatter. This asymmetry is parameterized by the baryon-to-photon ratio,

$$\eta = \frac{n_b - n_{\bar{b}}}{n_\gamma} = \frac{n_b}{n_\gamma}, \tag{1}$$

where n_b,$n_{\bar{b}}$ and n_γ are the baryon, anti-baryon, and photon number densities respectively.

When the universe exhibited an average energy of 10^{12}eV—10^{8}eV corresponding ($1\mu s < t < 1s$), quarks remaining after the annihilation of all anti-quarks combined to form the first neutrons and protons, becoming the first baryonic matter. These nucleons freely exchanged such that,

$$n \longleftrightarrow p + e^{-} + \bar{\nu_e} \tag{2}$$

$$p + e^- \longleftrightarrow \nu_e + n. \tag{3}$$

Here the number ratio of neutrons to protons follow the relation

$$\frac{n_n}{n_p} = e^{(m_n - m_p)c^2/k_b T} \tag{4}$$

where m_n, m_p are the neutron and proton masses. At this point, the Lepton number (number of leptons minus anti-leptons) has not yet been fixed, since leptons and anti-leptons are still freely interchanging through the above mentioned beta interactions. At $t = 1$ s or $2 - 3$ MeV, the universe cools enough for neutrons and protons to stop interchanging, and so this ratio locks out at $n_n/n_p = 1/6$. Accounting for neutron decay, this number becomes $n_n/n_p = 1/7$ by the time all free neutrons incorporate into primordial nuclei.

During Leptogenesis, 10^8 eV—10^6 eV, Leptons and anti-leptons still freely interact for some time because their interactions require much less energy: pair production of an electron-positron pair, for instance, requires 511 keV. Before neutrino decoupling at 2-3 MeV, neutrinos are kept from free streaming by,

$$e^- + e^+ \longleftrightarrow \nu_e + \bar{\nu}_e. \tag{5}$$

However, when the expansion rate is greater than the reaction rate, neutrinos fall out of equilibrium with electrons, positrons and photons so $T_\nu \neq T_{\gamma,e}$. Neutrinos are now permitted to free stream, and this is the source of the yet unobserved cosmic neutrino background.

After electron-positron annihilation, the neutrino-photon temperature ratio becomes:

$$\frac{T_\nu}{T_\gamma} = \left(\frac{4}{11}\right)^{1/3}. \tag{6}$$

Lepton number is conserved in standard models of physics. Since the universe conserves charge, any excess of electrons will be equal to the excess of protons in the universe, so if there any violation of lepton number, this will be due to an asymmetry in neutrinos versus anti-neutrinos. Then the neutrino to photon ratio will be

$$\eta_\nu = \sum_{i\in\ e,\ \mu,\ \tau} \frac{n_{\nu,i} - n_{\bar{\nu},i}}{n_\gamma} \tag{7}$$

and the chemical potential will be non-zero. The different flavors of standard model neutrinos undergo mixing so we can assume they will be in equilibrium, so their chemical potentials will be equal. We parameterize this in terms of a chemical potential and the temperature:

$$\xi = \mu/k_b T, \tag{8}$$

where $\xi = \xi_e = \xi_\mu = \xi_\tau$. Which after applying some standard statistical mechanics,

$$\eta_\nu = \frac{\pi^3}{12\zeta(3)} \left(\frac{T_\nu}{T_\gamma}\right)^3 \left(\xi_\nu + \frac{\xi_\nu^3}{\pi^2}\right). \tag{9}$$

Big Bang Nucleosynthesis (BBN) occurs between 10 MeV and 100 keV, when the first atomic nuclei are formed. First Deuterium (D$\equiv^2$H) is formed when a single neutron binds to single proton. Off of this, more complex nuclei are formed such as Tritium (^{3}H), which is unstable, Helium (^{3}He and ^{4}H) and Lithium (^{6}Li and ^{7}Li).

The expansion of the universe and the subsequent drop in temperature have

an immediate effect on the progress of the nuclear reactions. When the expansion out competes the nuclear reactions at ≈ 100 keV, BBN comes to an end and the relative amounts of each nuclei becomes fixed until the first stars come to light much later.

Since the reaction rates of each of these is known from laboratory experiments, we can use these relative abundances to extrapolate information about the state of the universe and its makeup during earlier epochs.

Energy Density as a Cosmological Diagnostic

The expansion of the universe can be characterized by the scale factor $a = a(t)$. From the Friedmann equation,

$$H^2 = \left(\frac{\dot{a}}{a}\right)^2 = \frac{8\pi G\rho}{3} \tag{10}$$

where ρ is the energy density and G is the gravitational constant. This tells us that the any change to the expansion rate from what is expected from standard BBN (SBBN) is due to a change in the energy density or a change in the gravitational constant, G. Following Steigman (2012), we denote any change from currently accepted physics as a change in the expansion rate by some factor S:

$$H \rightarrow H' \equiv SH. \tag{11}$$

We continue this analysis on the assumption that G is indeed fixed and assume any perturbation S is due chiefly to a perturbation to the enery density, ρ. During BBN, the universe was radiation dominated so

$$\rho = \rho_{rad} \equiv \rho_e + \rho_\nu + \rho_\gamma. \tag{12}$$

This is important because even though neutrinos are very difficult to measure in the lab, they will have a measurable effect on the energy density of the universe, and thus the expansion rate.

Looking at the number of degrees of freedom for each contributor, we find $g_\gamma = 2$, one for each helicity, $g_e = 4$ from 2 helicities for both electrons and positrons, and $g_\nu = 2N_\nu$. If there are any yet undiscovered generations of neutrinos, then the effective number of neutrino generations is $N_{eff} = N_\nu + \Delta N_\nu$. $N_\nu = 3.046$ as opposed to 3 exactly to account for the fact that at decoupling, neutrinos are not instantaneously and completely decoupled from electrons, positrons, and photons, so neutrinos do contribute a bit more to the energy density (Mangano et al., 2005). Any deviation in the radiation density then becomes

$$\rho'_{rad} \equiv \rho_{rad} + \Delta N_\nu \rho_\nu \tag{13}$$

Taking $T_\gamma = T_\nu = T_e$ and $\mu_\gamma = \mu_\nu = \mu_e = 0$, we apply our energy density perturbation giving us an expected expansion-rate perturbation

$$S^2 = \left(\frac{H'}{H}\right)^2 = \frac{\rho'_{rad}}{\rho_{rad}} = 1 + \frac{7}{43}\Delta N_\nu. \tag{14}$$

This is the relation between the deviation of expansion rate to any deviation from our number of neutrino flavors. This is then also related to the lepton asymmetry:

$$\Delta N_\nu(\xi) = \frac{90}{7}\left(\frac{\xi}{\pi}\right)^2 \left(1 + \frac{1}{2}\left(\frac{\xi}{\pi}\right)^2\right) \tag{15}$$

The energy density during BBN, or alternatively the expansion rate, can thus be used to test alternatives to the standard picture of ΛCDM cosmology.

Extrapolating from results of BBN codes, Steigman (2012) provides a relation

between the primordial Lithium and Deuterium abundance ratios (Li/H and D/H), the primordial Helium mass fraction Y_p, baryon-to-photon ratio η_b, non-standard expansion factor, S, and neutrino degeneracy parameter, ξ:

$$\begin{aligned} \eta_D &= 10^{10}\eta_b - 6(S-1) + 5\xi/4 \\ \eta_{He} &= 10^{10}\eta_b + 100(S-1) - 575\xi/4 \\ \eta_{Li} &= 10^{10}\eta_b - 6(S-1) - 7\xi/4 \end{aligned} \tag{16}$$

where the light element parameters follow:

$$\begin{aligned} \eta_D &= \left(\frac{10^{-5}D/H}{45.7(1.00 \pm 0.06)}\right)^{1.6} \\ \eta_{He} &= \frac{Y_p - 0.2381 \pm 0.0006}{0.0016} \\ \eta_{Li} &= 6\sqrt{\frac{10^5 Li/H}{4.82(1.00 \pm 0.10)}} \end{aligned} \tag{17}$$

and the uncertainties listed here come from uncertainties in nuclear reaction rates from experiment. These extrapolations are valid in the range $5.5 < 10^{10}\eta_b < 6.5$ and $0.85 < S < 1.15$. The measured Lithium abundance is a factor of a few smaller than the expected abundance, leading the the notorious *Lithium Problem* (Fields, 2011), so we opt to eliminate out Lithium to produce a function of the remaining parameters which can be constrained by observation. Currently, an additional Neutrino species is disfavored by both CMB studies and by astrophysical studies (Planck Collaboration, 2015; Cooke et al., 2014; Balashev et al., 2016; Riemer-Sørensen et al., 2015). However, Mosquera and Civitarese (2015) show that including a heavy sterile neutrino keeps D/H in agreement with CMB, though this calculation still fails to account for the observed Lithium abundance.

D/H as a Cosmological Probe

Since the production of Deuterium is an intermediate step to all other light element reactions, so it forms what is often referred to as the 'Deuterium bottleneck'. Deuterium is then sensitive to the baryon number and is then a key piece of understanding the physics of this epoch.

The observed Deuterium abundance is comprised of any Deuterium that did not go into heavier elements. Deuterium can be produced inside of stars as an intermediate step in stellar fusion, but all of this Deuterium is converted to Helium, and so does not survive. No other known source can produce Deuterium in relevant amounts (Reeves et al., 1973), so any observed Deuterium is thought to be primordial. The local D/H from the local interstellar medium (LISM) is about a factor of two less than D/H measured at high-redshift towards quasars (QSOs), $\mathrm{D/H}_{LISM} \sim 1.6 \times 10^{-5}$ with much scatter along different lines-of-sight, consistent with D being incorporated into stars and destroyed (Linsky et al., 1993, 1995, 2006).

The abundance ratio of Deuterium to Hydrogen, D/H, has been historically used to measure the baryon abundance because all observed D is thought to be primordial, D/H varies monotonically with η_b, and D destruction is thought to be predicted as a function of metal abundance, though D destruction is insignificant when metal abundances are under 1% of the solar value (Prantzos, 1996; Tosi et al., 1998; Matteucci et al., 1999).

The cosmological Deuterium abundance is a number that has been known for some decades now, with the first measurements beginning in earnest in the nineties (Tytler et al., 1996; Burles and Tytler, 1998a,b; Burles et al., 1999). After two decades of measuring D/H in QSO absorption lines, the error on this number

is now down to just a few percent, in agreement with previous CMB measurements (Bennett et al., 2013; Planck Collaboration, 2015) and together, are consistent with standard Big Bang Nucleosynthesis entailing a standard expansion rate and neither extra neutrino degrees of freedom nor a varying gravitational constant, G. There remains, however disagreement with studies of the other primordial light elements, He and Li.

Due to an isotopic shift of $\Delta v \approx 82\mathrm{km\ s^{-1}}$ between H I and D I, D/H measurements require high-resolution spectroscopy. This science is obfuscated by the fact that Deuterium us typically hopelessly blended into related H I absorption. As of 2016, including the new objects reported in this dissertation, there are 17 objects which have been used to measure extragalactic D I/H I and three reporting extragalactic measurements of molecular $HD/2H_2$.

For D/H measurements along QSO sight lines, measurements are much more tightly constrained than in the past, but over all literature, the spread of values is still indisputable and worrying. Dvorkin et al. (2016) suggests that at least some of this dispersion may be due to differences in structure formation history between the systems studied, while many authors (Kirkman et al., 2003; Pettini et al., 2008b; Ivanchik et al., 2010; Srianand et al., 2010; Olive et al., 2012) have suggested that this dispersion is may come from underreported errors or simply poor measurements from data that is lacking.

Addressing this concern, Cooke et al. (2014) introduced a set of strict selection criteria in their study of what they call *The Precision Sample* for spectra which may be considered for D/H measurements:

- The H I Lyα line must exhibit Lorentzian damping wings, *i.e.* $\log \mathrm{N} \geq 19\mathrm{cm^{-2}}$, which allows the column density to be accurately determined independently of the cloud model, uniquely by the damping wings.

- These damping wings cannot be strongly blended with other strong absorption features.
- At least two optically thin transitions of D I should be visible in the data.
- The data must be high-resolution, such that FWHM$\leq$ 10km s^{-1}.
- In order to accurately determine the velocity structure of the gas, either (a) several unblended metal lines with a range of oscillator strengths for each species must be available in the spectrum or (b) the data must exhibit more than transition of D I.

Subsequent studies however, have questioned the helpfulness of these criteria. (Balashev et al., 2016) reports on a new D/H object that passes the criteria, but has a low D/H, increasing this data set's dispersion. Chapter 4 of this dissertation adds to this, yet again with low D/H. In Chapter 5 we discuss this in more detail.

We measure the D/H ratio by performing precision measurements of the column density ratio N(D I)/N(H I), which is a proxy to the total ratio of D/H, requiring no ionization correction for our level of precision. Cooke and Pettini (2016) introduced an ionization correction, which accounts for up to a 0.1% difference for metal-poor DLAs. This is 10-100$\times$ smaller than the currently accepted errors on D/H, and so can be safely ignored.

While Ω_b is thought to be known to good precision (<1%), an increasingly important source of error are nuclear reaction rates. Updated values of these reaction rates are incorporated into calculations by Cyburt et al. (2016) and Coc et al. (2015) finding $(D/H)_p = 2.58\pm0.13$ for $10^{10}\eta = 6.10$ and $(D/H)_p = 2.45\pm0.05$ for $10^{10}\eta = 6.09$, respectively.

Introduction to Absorption Line Analysis

Here we present a general introduction to atomic absorption lines for the reader.

An analysis of absorption spectroscopy involves taking a spectrum towards a bright object to be used as a back light, typically as quasar, and observing the attenuation of flux as a function of frequency or wavelength. The observed amount of absorption is called *optical depth*, symbolized τ. A line is said to be optically thick if it is saturated, or blocks all of the flux for some wavelength range, whereas it is optically thin if it blocks $< 30\%$ of the incident light. We then use an absorption model to fit the flux as a function of wavelength and attempt to glean physical insight on the absorbing or emitting gas.

Line Broadening

An ideal absorption (or emission) line would be a delta-function, having no width, with a wavelength purely dependent on the energy of the absorbing or emitting transition. However numerous physical effect will contribute to the shape of the line, adding a wealth of information to be extracted.

Typically, spectral lines are modeled as a Voigt profile Bechtold (2001): a convolution of a Lorentzian distribution, incorporating Natural and collisional broadening, with a Gaussian distribution, incorporating Doppler broadening from the thermal motion of the gas. There are other typically sub dominant contributions to line shape from a variety of physical phenomenae, but we will not treat them here.

Natural Line Broadening

One component of line broadening arises from the Heisenberg uncertainty principle, known as *Natural Line broadening.* There is an inherent uncertainty in the lifetime that any electron remains in a given state. With u and l referring to an upper and lower level, respectively, energy E, frequency $\nu = c/\lambda$, Planck's constant h, and τ referring to the uncertainty in occupation time of a given state:

$$\Delta E_u \Delta t_u = h\Delta\nu \times \tau \geq \frac{h}{2\pi}. \tag{18}$$

so we obtain a lifetime-limited uncertainty of

$$\Delta\nu_u = \frac{1}{2\pi\tau_{rad}}. \tag{19}$$

when allowing this to naturally return to our lower state, l, which is typically our ground state with $\tau_{l=0} = \infty$, we get our natural broadening uncertainty,

$$\Delta\nu_N = \frac{1}{2\pi\tau_u} + \frac{1}{2\pi\tau_l} = \frac{1}{2\pi\tau_u} \tag{20}$$

We then solve the harmonic oscillator equation about the line center, ν_0, with damping factor $\gamma = \Delta\nu_N$, and inverse Fourier Transform to get the amplitude as a function of frequency:

$$\phi(\nu) = \frac{\gamma}{4\pi^2} \frac{1}{(\nu - \nu_0)^2 + (\gamma/4\pi^2)^2} \tag{21}$$

where ν_0 is the line-center. The factor γ derives from spontaneous decay rates of each transition.

Collisional broadening

Collisions also limit the lifetime of a given atomic state, contributing to $\Delta\nu$. This is most significant for large wavelengths, low gas temperatures and high pressure. The frequency at which collisions occur can be treated as $\nu_{coll} = v_{th} n \sigma_{coll}$, with thermal speed $v_t h = \sqrt{2k_b T/m}$, number density n and collisional cross section, σ_{coll}. This contributes to natural broadening as $\Gamma = \gamma - 2\nu_{coll}$, and impacts equation 21 accordingly by replacing γ with Γ.

Gaussian Profile: Thermal Broadening

Thermal (Doppler) broadening arises from the random motion of the gas, causing Doppler shifts, which, for neutral Hydrogen (H I) are typically typically small (less than a few tens of km s^{-1}), but occasionally quite large (hundreds of km s^{-1}). This most significantly affects the line profile for low gas pressure, small wavelengths and high gas temperatures.

The Maxwell-Boltzmann distribution describes the velocities of a gas:

$$f(v) = \left(\frac{m}{2\pi k_b T}\right)^{3/2} 4\pi v^2 \exp\left(\frac{-mv^2}{2k_b T}\right). \tag{22}$$

Applying the Doppler effect where $\nu/\nu_0 = (1 - u/c)$ where ν and ν_0 are observed and emitted frequencies and u is the relative velocity, we find:

$$\phi(\nu) = \frac{1}{\delta\nu_D} \exp\left(\frac{(\nu - \nu_0)^2}{\delta\nu_D^2}\right) \tag{23}$$

where

$$\Delta\nu_D = 2\nu_0 \sqrt{\frac{2k_b T \ln 2}{mc^2}} \tag{24}$$

is full-width, half maximum (FWHM), describing the width of the line at half of the maximum height or depth.

The Voigt profile

Convolving these two line profile functions together, our line profile is expressed in terms of the Voigt function,

$$\phi(\nu) = \frac{1}{\Delta\nu_D\sqrt{\pi}} H(a, w) \tag{25}$$

with the Hjerting function, $H(a, w)$, defined as

$$H(a, w) \equiv \frac{a}{\pi} \int_{-\infty}^{+\infty} dy \frac{e^{-y^2}}{a^2 + (w - y)^2} \tag{26}$$

making use of the substitutions,

$$\begin{aligned} a &= \frac{\Gamma}{4\pi\Delta\nu_D} \\ w &= (\nu - \nu_0)/\Delta\nu_D. \end{aligned} \tag{27}$$

When a is small, the center region of the line will be dominated by the Gaussian contribution and the wings of the absorption line will be dominated by the Lorentzian contribution.

Absorption Line Parameters

Fitting absorption first involves fitting an unabsorbed continuum level, which describes the spectral behavior of the light incident to the absorbing medium. Then, absorption features are identifies and absorption models are tried. In studies of QSO absorption lines which use the above discussed Voigt profile decomposition, the absorption model is parameterized in terms of three parameters. Column density,

N, Doppler parameter, b, and redshift, z.

Column density, N, gives the number of atoms per square centimeter along the entire line-of-sight of the column, some distance s:

$$N = \int_0^s n ds' \tag{28}$$

with particle number density, n.

Our line-width parameter is written as

$$b = \sqrt{b_{th}^2 + b_{turb}^2} \tag{29}$$

with b_{turb} accounting for all non-thermal turbulent motion. Depending on the conditions of the gas or the observations, other contributions, such as instrumental broadening or Hubble broadening may also be needed. We define the thermal contribution as

$$\begin{aligned} b_{th} &= \sqrt{2k_b T/m} \\ &= \frac{c}{2\nu_0\sqrt{\ln 2}}\Delta\nu_D \end{aligned} \tag{30}$$

where, again, ν_0 is the line center frequency and $\Delta\nu_D$ is the FWHM from Doppler broadening. This parameter is commonly called the *Doppler parameter* because the thermal contribution causing Doppler broadening is commonly the most important contribution to it.

Redshift parameterizes the location of the line center in light of cosmology, following from Hubble's law, $v = Hr$, in which more distant objects tend to removing away with increasing speed, and thus being increasingly red shifted, due to cosmological expansion. We parameterize this in terms of the fraction change in

observed versus rest-frame emitted wavelength, λ and λ_r, respectively:

$$(1 + z_{abs}) = \frac{\lambda}{\lambda_r}. \tag{31}$$

Smaller changes in redshift are often described in terms of change in velocity required to produce the observed change in redshift. For non-relativistic velocities:

$$\frac{\Delta v}{c} = \frac{\Delta \lambda}{\lambda} = \frac{\Delta z}{1 + z_{abs}}. \tag{32}$$

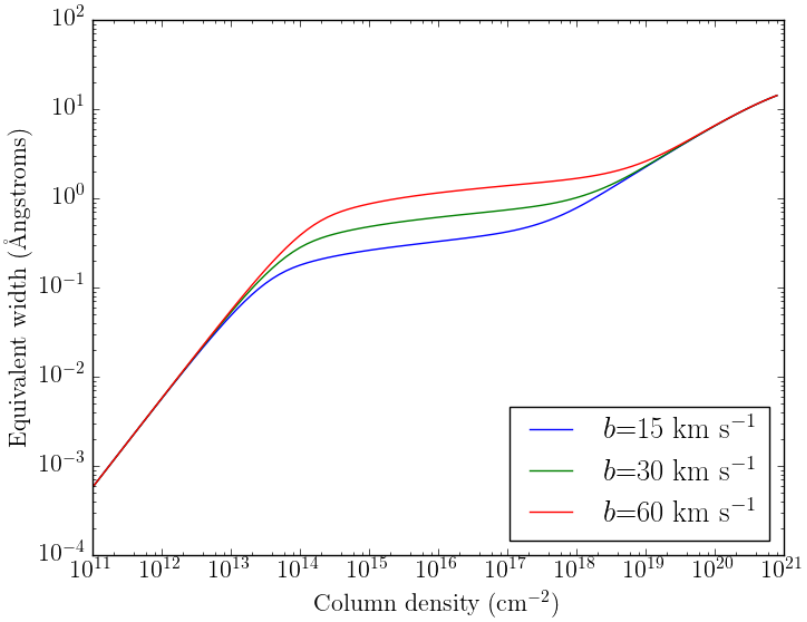

Figure 1. The Curve of Growth for an H I Lyα line with Doppler parameters 15,30 and 60 km s^{-1}. Note that the Doppler broadening parameter, b, has little effect on the equivalent width outside of moderate column densities.

Radiative Transfer and the Curve of Growth

The curve of growth describes the relation between optical depth and line strength, giving us a means to map physical conditions (density or number of

atoms) to observable quantities (optical depth).

We begin by considering Kirchoff's law of radiative transfer, which states

$$\frac{dI_\nu}{ds} = -\kappa_\nu I_\nu + j_\nu \tag{33}$$

where I is intensity, s is absorption distance, j is emissivity and our absorption rate is κI. The subscript ν indicates the frequency of the incident light. The spectral shape of the incident radiation is called the *continuum*. Substituting differential optical depth, $d\tau = \kappa ds$ and source function $S = j/\kappa$, and suppressing the subscript, this may be written as

$$\frac{dI}{d\tau} = -I + S \tag{34}$$

with solution,

$$I = I_0 e^{-\tau} + \int_0^\tau d\tau' S(\tau') e^{-(\tau - \tau')}. \tag{35}$$

Emissivity j is the rate of energy emission per unit volume, solid angle, frequency and time. The value of $\kappa = n\sigma$, comes from analysis of transition rates in light of the Einstein A and B coefficients. For more detail, refer to any text covering radiative transfer. The optical depth of our light passing through the gas is

$$\tau = \int n\kappa_{\nu_0}\phi(\nu)dl = \kappa_{\nu_0}\phi(\nu)\int ndl \tag{36}$$

The amount of absorption from our line is exactly equal to the area under a rectangle with height the same as our continuum and width equal to what is called the *equivalent width*:

$$
\begin{aligned}
W &= \int d\nu \, (1 - I_\nu / I_0) \\
&= \int d\nu \, (1 - \exp(-\tau)) \\
&= \int d\nu \, (1 - \exp(-N \kappa_{\nu_0} \phi(\nu)))
\end{aligned}
\tag{37}
$$

We now have a relation between equivalent width, column density, line broadening and optical depth.

In Figure 1, we show the relation between equivalent width and column density for Doppler parameters 10,30 and 60 km s^{-1}. For neutral hydrogen, H I, $b < 10$km s^{-1} is rare and in fact may often be attributed to fitting or instrumental error and $b > 60$km s^{-1} is also rare. b-value does not play a significant role for small N(H I) and large N(H I) systems, however, most neutral hydrogen absorption occupies the range N(H I)=$10^{13}-10^{18.5}$cm^{-2}, in which the b-value plays an important role in determining the line profile.

Chapter 1

Observations and Data Reduction

All data in this dissertation was obtained using the High-resolution echelle spectrometer (HIRES) on the Keck I telescope at W.M. Keck observatory (Vogt et al., 1994). We obtain the data over a number of observing runs and extract using Tom Barlow's MAKEE[1] and in-house code to facilitate the process and perform custom manipulations as needed.

Wavelength Calibration Error

In addition to the standard wavelength calibration to Thorium-Argon arc lamp spectra available for HIRES, we apply additional velocity corrections.

Unavoidable random velocity error comes from a combination of the small error introduced by the extraction procedure's pixel-to-wavelength conversion and from the fitting error when we determine the wavelength of a given feature in the QSO spectrum. The pixel-to-wavelength conversion error is typically few hundredths of an Ångstrom, which in terms of velocity means $\delta v = 1$ km s^{-1} at 5000 $\mathring{A}$ and $\delta v = 2$ km s^{-1} at 3000 Å.

The accuracy of the wavelength scale has an effect on the certainty with which we can identify absorption due to D, and with the column densities we

[1] `makee` is available at:
http://www.astro.caltech.edu/~tb/makee/

measure for D, H and other elements. After standard wavelength calibration procedures and heliocentric velocity corrections, we discovered that there were still small systematic velocity shifts of up to a few km s^{-1}, in excess of random errors, on several integrations of our object. A systematic velocity shift may be a cause for concern when co-adding many constituent integrations into a master spectrum, as they may artificially widen absorption lines or obscure certain spectral features, complicating the determination of the absorber velocity structure and column densities. We used a sample of metal lines distributed throughout the spectrum to measure this wavelength shift with respect to the mean wavelengths of each line over all integrations. After extraction, we corrected the wavelength scale of each integration before re-binning and combining.

Definition of Wavelength Scales

One dimensional spectra have a wavelength scale defined by the standard `fits` header cards for the fiducial wavelength λ_{ref}, reference pixel n_0 and pixel width Δ, named `CRVAL1`, `CRPIX1` and `CDELT1` respectively in the `fits` header. Log-linear wavelength scales are defined as a function of pixel n such that,

$$\log \lambda = \log \lambda_{ref} + \Delta(n - n_0). \tag{1.1}$$

Typical values for our fiducial wavelength and pixel-width in units of log-wavelength are `CRVAL1`$\simeq 3.5$ and `CDELT1`$\simeq 3 \times 10^{-6}$. In velocity, the pixel width is $\Delta = 2.1$ km s^{-1}.

Measurement and Correction of Velocity Drift

We have long known that the standard HIRES wavelength scale provided by Th-Ar arc spectra have errors that are a significant fraction of a pixel (Osterbrock

et al., 2000) and vary from integration to integration, which has been suggested to derive from errors in object positioning in the slit (Suzuki et al., 2003; Whitmore et al., 2010; Evans and Murphy, 2013; Whitmore and Murphy, 2015; Balashev et al., 2016). In a detailed study of 6 integrations of one QSO, Griest et al. (2010) found that absolute wavelengths drifted by 0.5 – 1.0 km s^{-1} over a few nights.

We implemented a velocity correction on each integration by comparing to velocities measured independently for a set of diagnostic lines we choose as a reference. In principle, any unsaturated, unblended line could be used, however, narrow lines—typically arising from metal absorption —are distinct enough to not be confused with neighboring lines by the person doing the fitting and furthermore tend to have smaller velocity uncertainty, so we limit our line selection to $b < 15 - 20$km s^{-1}. We do not care about their identification, and so fit them as Lyα lines, flagging them accordingly. We will call these lines *diagnostic metal lines*. Our process goes as follows:

- Select a number of diagnostic metal lines, encompassing the entire range of spectral range of the data, sufficient enough to adequately model the velocity shifting with respect to wavelength and integration.

- Perform a fit on each of these lines in each integration, being careful to throw out lines that could easily be confused for noise.

- Measure the shift of each line compared to the mean velocity of each line over the all integrations.

- Determine a velocity correction function as a function of wavelength. This was found to be linear.

- for each integration, correct the wavelength scale factors, `CRPIX1` and `CDELT1`,

according to our determined velocity correction function in the previous step.

The choice of diagnostic line is important. Lines that occur in low-SNR regions, such as the blue or near UV tend to be easily mistaken with noise, limiting our sample on the blue end. Lines that occur blended with other absorbers are also a poor choice as with lower SNR integrations, the lines become indistinguishable from their blending neighbors. We are thus careful to examine lines that are of a significantly poorer fit from the others and through out those that are more than 2σ from the fit.

This correction method was used to great success in our study of J1201+0116 (chapter 3), however this method produced little discernible improvement for J0744+2059, likely due to the fact that it is a dimmer object, so each integration tended to have poorer SNR than those of J1201+0116.

Flux Calibration

For each integration, we apply standard flux-calibration procedures, which involve taking a short integration of a star with well-known flux response, typically an O or B-type star exhibiting a minimal number of absorption lines, shortly before or after our integration of the QSO of interest. We then construct a smoothed flux-response function of the instrument and correct the QSO spectrum accordingly.

Even after such corrections, the flux response of HIRES is known to be unstable, which manifests as a series of flux jumps at echelle order edges. This can be most clearly seen be examining the spectrum of the standard star used. Suzuki et al. (2003) addressed this by correcting the flux response on each order to fit the flux response of another spectrum of the same object taken on a different instrument.

While these flux jumps were very noticeable in our study of J1201+0116, we determined that applying additional flux corrections such as those discussed in Suzuki et al. (2003) would not produce a measurable change in D/H. Our study of J0744+2059 did not exhibit the same magnitude of flux jumps as J1201+0116, however our spectra of J0744+2059 also had lower signal-to-noise, which may have concealed much of this effect.

Sky Subtraction Correction

Separately from standard flux calibration procedures, there was found to be non-zero flux in some saturated line-cores thought to have come from incomplete sky subtraction during extraction. This effect was small (less than a few percent of flux) but significant. We took a sample of 40 saturated absorption lines throughout the entire spectrum to characterize the effect. We took the average of 40 pixels surrounding the centers of each absorption line for each of the 40 absorbers. If the slope of the best fit line through this set of 40 means is significantly non-zero, and the correlation is significant ($p < 0.10$), then the best fit line is simply subtracted from the flux (See Figure 1.1). This correction was necessary for several, but not all of the integrations, to ensure that areas of spectra that were supposed to be zero flux actually exhibited zero flux.

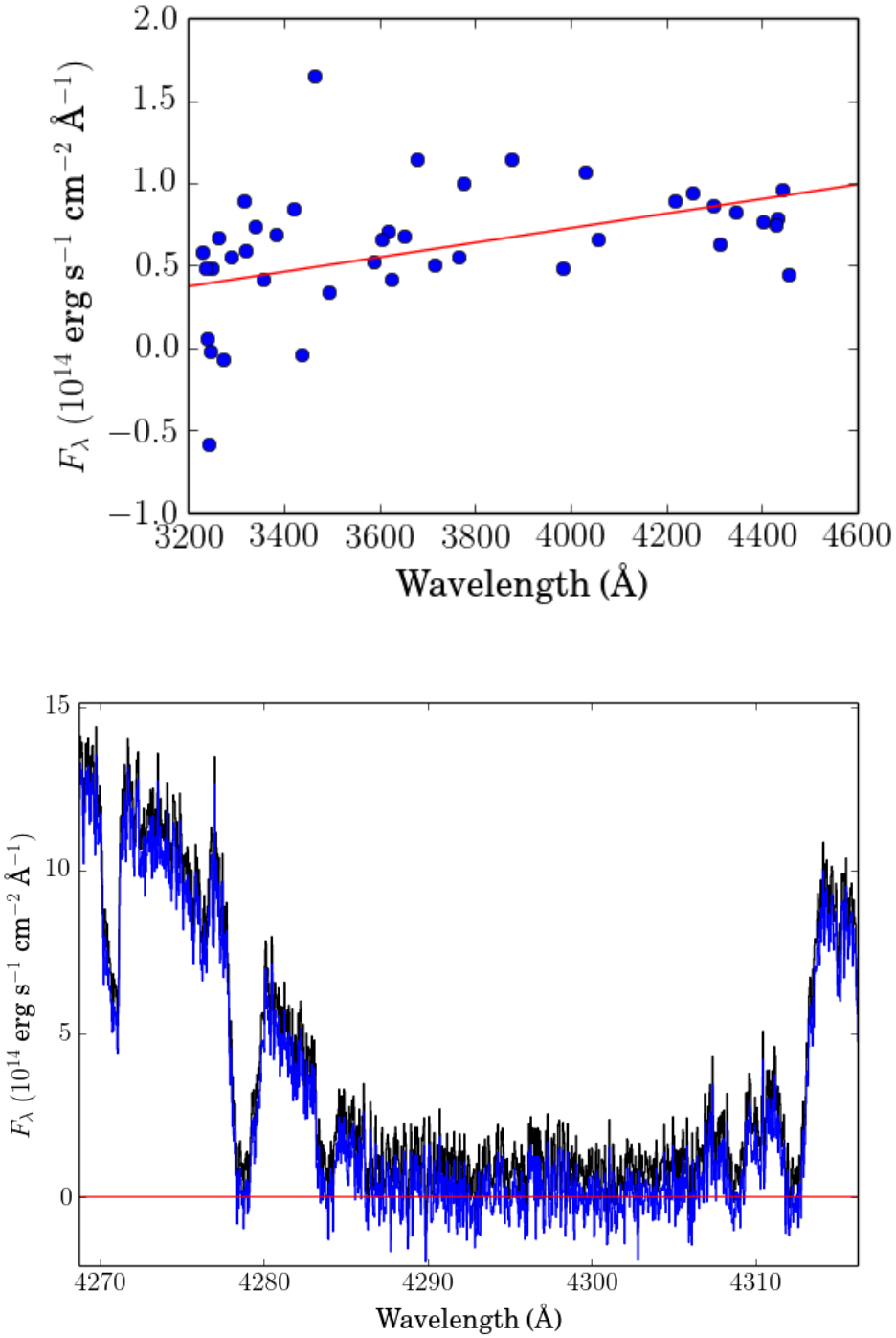

Figure 1.1. The linear regression through zero-flux regions of J0744+2059 (top) and the flux subtraction correction applied to the DLA at $z_{abs} = 2.5338$ towards J0744+2059 (bottom). The original spectrum is in black and the correction is in blue and the red line shows zero flux.

Chapter 2

Model Fitting Methods

Here we discuss the details of our model fitting method used in our precision estimates of D/H in chapters 3 and 4. For discussion of API and usage of relevant software, see our discussion of `dudeutils` in A.2.

Fitting Methods

Choice of Continuum

A potentially major source of error is determination of the continuum level. In regions with extensive absorption, such as Damped Lyman Alphas, this is particularly important. We use the minimum number of continuum control points to produce the desired continuum without unnecessary inflection points. Necessary inflection points which we account for include quasar emission lines and flux jumps caused by poor flux calibration, if these features have an effect on the absorption feature we are trying to measure. (See sections 1.1 and 3.1.1 for a discussion of flux calibration errors)

Flux jumps caused by flux calibration instabilities between echelle orders also have predictable locations, which can be seen by examining the standard star spectrum corresponding to the science spectrum taken. Standard stars, used for

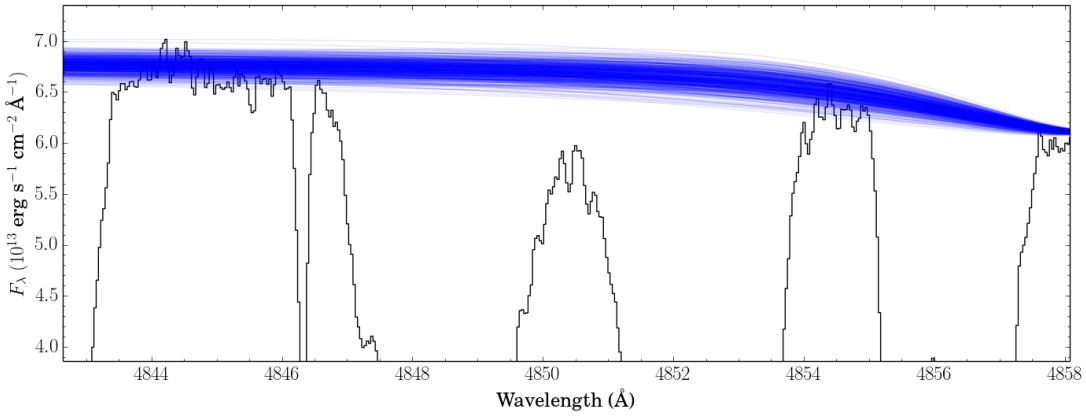

Figure 2.1. A sample of randomly generated continua about the Lyα transition at $z = 2.988$ towards J1201+0116. Each continuum was chosen independently of each other and without regard to their best fit value of D/H or goodness of fit. The difference in continuum level of these continua also roughly span the estimated flux calibration uncertainty expected in HIRES spectra: 4% difference at 4844 Å and 7% difference at 4848 Å). To estimate the error contribution to D/H, we take an unweighted standard deviation of all of the admitted values for D/H from each continuum here. Since this does not account for goodness of fit, and some continua are obviously much worse fitting than others, our error estimate is an overestimate.

fluxing spectra of other objects, are chosen because their flux is well known and they exhibit minimal absorption. This, incidentally, also makes them useful for examining the wavelengths of flux errors introduced by the instrument.

Continuum Statistics

To determine the effect of continuum level on D/H, we create a sample of continua. To get one sample, we randomly vary a set of continuum control points and the relevant fitting parameters and then proceed to alternate between optimizing over fitting parameters and continuum control points until we reach a locally best-fitting model. This is repeated hundreds of times to create a sample of continua used to measure the effect of the continuum on our absorbers. See figure 2.1 for one example used for our study of J1201+0116.

Statistical Parameter Errors

We use in-house software to fit our data (`dudeutils`, see section A.2), randomly sampling initial fitting conditions and then running `dude`'s built-in optimizer, which implements a Levenberg-Marquardt algorithm. This process is repeated until there are sufficient samples to perform our statistics.

We can estimate 1σ error on a parameter by locking the value an interesting parameter, allowing all other parameters to vary freely around it and then map the interesting parameter's effect on χ^2. The calculated confidence interval includes all of the values of that parameter such that $\chi^2 < \chi^2_{min} + \Delta$, where Δ is some number that depends on the number of interesting parameters and the desired confidence level (Avni, 1976). $\Delta = 1$ for one interesting parameter at a time with a 68% confidence level. Our software does this by randomly choosing input parameters and locking one at a time, optimizing all of the free parameters, and producing a map of each parameter value to χ^2. `dude` treats continuum points and absorption parameters N, b, and $z_{\rm abs}$ separately, so when considering all of these simultaneously, we alternate between optimizing the coordinates of continuum points and the values of these absorption parameters.

Without guidance, this method can introduce unphysical models, which can artificially inflate the error estimate. By not exploring enough of the parameter space, errors can be artificially deflated. It is thus important to have some physical intuition when examining these models. Model constraints must be chosen carefully so as to not bias the measurement, but the range of initial guess values should be wide enough to cover everything of interest.

Velocity Structure

Systems which are heavily blended can complicate the determination of velocity structure. While wider H I absorption lines may blend into each other, narrower metal lines associated with the system in question may exhibit less blending. Systems with many metal lines tend to be of even greater use, providing more degrees of freedom to determine the velocities.

Where the fits are more complicated by blending, we are forced to rely on statistical techniques to choose a best fitting model. If the number of blended systems is not obvious, we try fits by adding more absorbers until reduced-χ^2 shows minimal improvements. That is to say, find the minimal number of absorbers required to produce a sufficiently good fit. With this number of absorbers set, we then proceed to walk the absorbers through a range of locked velocities, using the method described in 2.2 to determine confidence intervals.

J1201+0116 had only two metal lines of questionable fit, so we relied on statistical methods to determine velocities of our neutral absorbers. see Figure 2.2 for our χ^2 on one of our contaminant absorbers blending with Lyα, which we determined was likely an unidentified metal line. J0744+2059, on the other hand, had many metal lines, however they were all fully saturated, so we instead relied on the velocity of unsaturated transitions of D I.

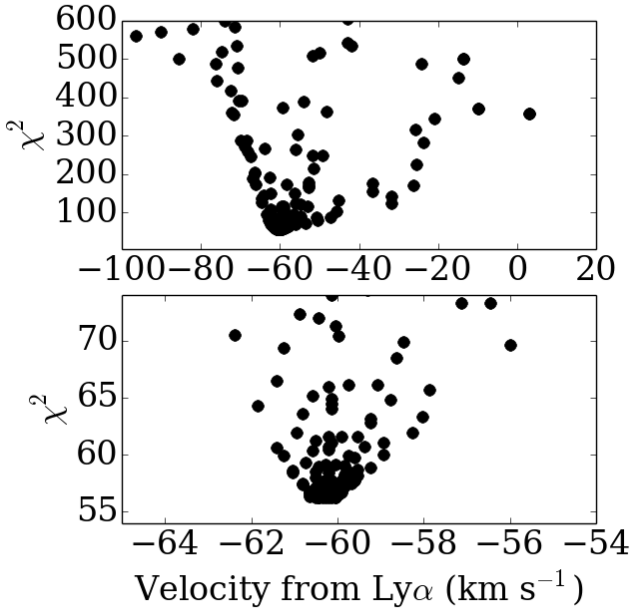

Figure 2.2. χ^2 versus velocity measured from an absorber contaminating the Lyα line at $z = 2.988$ towards J1201+0116. This plot shows typical usage of `dudeutils` for estimating the best parameter estimate and it statistical error. The bottom plot is top plot zoomed in to show best several models, so that a user can estimate the error.

Chapter 3

The Deuterium-to-Hydrogen Ratio Towards QSO J1201+0116

We report on the discovery of D/H towards a bright (17.4 mag, G-band) QSO exhibiting one system of D on the absorption edge of Neutral Hydrogen in the Lyα transition. Despite some blending with the H I, we are still able to determine D/H to 7% error, consistent with literature. This system exhibits the second smallest neutral column density in D/H literature at $N_{HI} = 10^{17.4} cm^{-2}$ (for references, see table 5.3), standing in contrast to the Cooke et al. (2014) selection criteria. This system is highly ionized and shows very little metal content, in fact, one of the lowest in D/H literature ($[Si/H[] = -3.3 \pm 0.8$, $[O/H]_{<-3.2}$, 2σ upper limit). Having such small metal content is important because it suggests that very little processing of gas has occurred for this system, thus, being representative of the primordial value of D/H. This object also continues to support the idea that there is no detectable evolution of D/H with decreasing metallicity among metal-poor systems. Also of note is that this system has one of the smallest neutral Hydrogen column densities in D/H literature, consistent to within errors with the H I at z_{abs}=2.50357 towards Q1009+2956 (Burles and Tytler, 1998b).

We report a value of 10^5D/H$= 2.50 \pm 0.18$, which is fully consistent with

expectations from Big Bang nucleosynthesis calculations (Cyburt et al., 2015), and the inferred D/H from the CMB (Planck Collaboration, 2015).

Observations

The earliest published reference to this object, under the B1950 name Q1159+01 appears in Lanzetta et al. (1991), who further reference the original discovery to have come from earlier unpublished work. This quasar was later reported as part of the Sloan Digital Sky Survey's first data release (Schneider et al., 2003) under the name SDSS J120144.36+011611.5. The full coordinates we used were 12:01:44.36+01:16:11.54.

We obtained 16 integrations of J1201+0116 from the High Resolution Echelle Spectrometer (HIRES) described in Vogt et al. (1994). The integrations were taken from 2008 to 2011 and total to 62760 seconds of integration time. A list of the individual integrations can be found in Table 3.1. All of the spectra were extracted and reduced with an automated in-house pipeline wrapping Tom Barlow's MAKEE[1] extraction and reduction code. We performed the typical suite of extraction and reduction procedures: flat field corrections, bias corrections, sky subtraction, wavelength calibration from Th-Ar arc lamp spectra, flux calibration using standard-star spectra and then aligned each integration and trimmed the ends of our resultant one-dimensional spectra to the same wavelength range, 3377 Å to 6200 Å [2]. Spectral regions where an integration does not have data are masked. Figure 3.1 shows the sum of these 16 integrations into a single master spectrum, which exhibits a signal-to-noise of 60 at the Lyα emission peak at 5144 Å and

[1] `makee` is available at:
http://www.astro.caltech.edu/~tb/makee/

[2] Regions of spectrum where a specific integration does not have data are retained as masked pixels, so that the pixel numbers still match between integrations

Table 3.1. Observations of J1201+0116 . All integrations used the C5 decker (7" × 1.148") and used a set-up producing a wavelength range of 3353-4282 Å, 4311-5280 Å, 5323-6200 Å for the blue, green and red CCDs respectively except for integration 257, which used the C1 decker (7" × 0.861") and had a wavelength range of 3538-4471 Å, 4521-5449 Å, 5522-6414 Å. All together, these spectra have 62135 seconds of integration time. The reported velocity is the mean velocity offset of each metal line in this integration from the mean wavelength of the corresponding metal line over the whole sample. $v < 0$ means that an integration has systematically lower wavelengths compared to the dataset as a whole. r is the correlation correlation for velocity offset of the metal lines of this integration versus the mean wavelengths of the metals for the whole dataset and p gives the probability of seeing a shift greater than that if there were no systematic shift.

				best fit of deviation from mean wavelengths		
id	Date Y-M-D	start time (UTC)	Integration Time (s)	velocity shift from sample mean (km s^{-1})	r	p
202	2008-01-13	13:59:19	600	1.41 ± 1.16	0.065	0.741
124	2008-02-20	10:39:44	3900	0.6 ± 2.2	0.030	0.865
125	2008-02-20	11:45:21	3900	0.16 ± 0.90	-0.049	0.800
227	2008-02-22	08:41:33	3600	-1.15 ± 1.09	0.083	0.680
228	2008-02-22	09:42:09	3600	-1.08 ± 1.07	0.116	0.547
230	2008-02-22	11:50:12	3600	-2.73 ± 0.79	0.044	0.827
231	2008-02-22	12:50:48	3600	-1.92 ± 1.12	0.485	0.008
091	2008-03-28	08:50:52	3600	0.99 ± 0.72	0.326	0.069
092	2008-03-28	09:51:35	3600	1.29 ± 0.80	-0.113	0.524
093	2008-03-28	10:55:20	3600	1.24 ± 0.73	-0.267	0.140
257	2009-12-12	14:28:02	4680	-3.11 ± 1.11	-0.634	0.00006
414	2009-12-13	14:35:36	4775	1.16 ± 1.67	0.130	0.448
548	2009-12-14	13:19:32	4500	2.29 ± 0.58	-0.225	0.315
549	2009-12-14	14:35:11	4500	2.02 ± 0.64	-0.351	0.072
1062	2011-01-27	13:36:40	5040	1.14 ± 0.90	-0.361	0.039
1177	2011-01-28	13:42:22	5040	-2.3 ± 7.6	0.022	0.895

SNR$\simeq$ 40 near our D I absorption line at 4847 Å.

Flux Calibration

After standard flux calibration procedures, HIRES spectra typically yield a 5-10% relative flux calibration error over wavelength scales of hundreds of Ångstroms. This is most apparent at the ends of echelle orders, where there are often sudden erroneous jumps in flux. This is a known problem and there exist non-trivial methods for correcting the relative flux calibration (Suzuki et al., 2003). Since

many of the order joins will be obscured by neutral Hydrogen absorption in the Lyα forest , the wavelengths of these erroneous jumps can be found by examining the corresponding standard star spectra, which have minimal absorption and a known flux behavior. Figure 3.2 shows the standard star spectra in the wavelength region near D. The H I and D I lines lie in the middle of an order join, at wavelengths sampled by two adjacent echelle orders. This overlapping region is co-added when summing the orders of our two-dimensional echelle spectrum into a single one-dimensional spectrum.

Additionally, the standard star spectra were masked at particular wavelength ranges during flux calibration, due to physical features in the standard star spectra that would complicate flux calibration. The flux is ignored here and interpolated through when a smoothed response function is calculated. $\lambda = 4847.00 - 4877.00$ Å was masked for Feige 67, λ =4849.40-4875.33 Å for Feige 34 and $\lambda = 4848.21 -$ 4877.00 Å for G191-B2B. The H I and D I Lyα absorption lies at the short wavelength end of the masked regions, where the stellar H-beta has no signification effect on the flux calibration. The value me measure for D/H can be sensitive to the accuracy of the relative flux at the positions of the H I and D I Lyα absorption lines, and across the surrounding region that we use to set the continuum level.

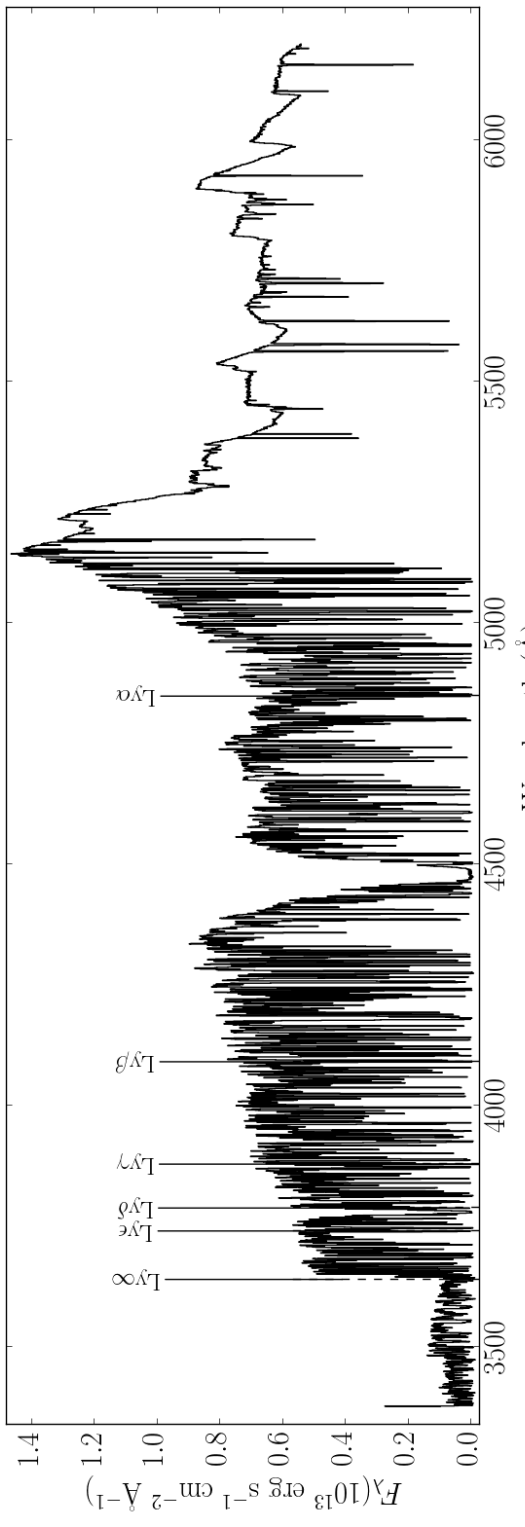

Figure 3.1. The full spectrum of J1201+0116 obtained from 16 integrations with HIRES on Keck I, rebinned for clarity. The position of the D I and H I Lyα lines are indicated, but both are too weak and narrow to see in this plot. The partial Lyman limit edge near 3641 Å is caused by the H in this same gas. There is a damped Lyα line at 4480Å caused by unrelated gas at $z_{\rm abs} = 2.685$. Flux jumps from flux calibration error at different echelle orders such as 5900 Å and 6000 Å can be seen red of the Lyman emission peak (5143 Å) where absorption is at a minimum. Other flux jumps occur to the blue of the Lyα emission peak in the Lyα forest , observed by examining standard star spectra of individual integrations, but are largely obscured by absorption here.

Wavelength Calibration Error

As discussed in section 1.0.1, wavelength calibration is sometimes problematic for Keck HIRES data. Our data is consistent with this effect, which may be seen under Table 3.1. Since we have 16 integrations on a bright QSO with good SNR on all but one integration, we were able to measure and correct these drifts.

We fit a sample of 37 metal lines throughout the entire spectrum for each of our 16 integrations separately and compared the velocity deviation for each metal line from the mean wavelength of that metal-line. We fit a regression line as a function of pixel-number to characterize each integration's deviation from the mean. The best fit parameters of a linear regression gives us factors by which to correct the wavelength scale for an individual integration; a non-zero slope means that the spectrum was stretched or compressed along the wavelength direction and a non-zero intercept is equivalent to an error in the fiducial wavelength for that integration. All of the lines were consistent with zero slope, meaning the wavelength scale is not being stretched or compressed, however 5 of the 16 integrations showed a significant velocity offset. We corrected all integrations by altering the fiducial wavelength `CRVAL1`. We then rebinned each integration into pixels with the same starting wavelength and pixel width before co-adding into a final master spectrum. In Figure 3.3 we plot the standard deviations of the wavelengths of the metal lines. Before the wavelegth corrections these averaged 2.06 km $s^{-1}$and after they were 0.69 km s^{-1}, consistent with measurement error.

Another problem we discovered was a constant, seemingly random velocity offset on the order of a few pixels, unique to HIRES' red CCD which appeared in integrations 257, 231 and 093. This correction involved shifting the data for the red CCD by one or two pixels in the spectral direction. This was accomplished

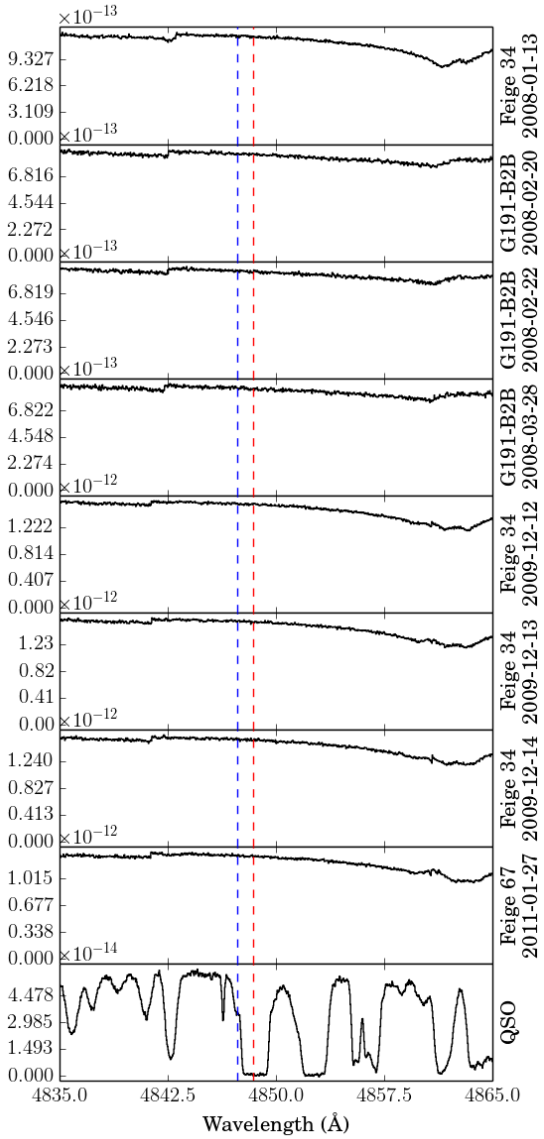

Figure 3.2. The standard star spectra used for each of our science integrations along with the QSO spectrum. Two orders contribute the flux from 4841.4 Å to 4861.8 Å, but only one order contributes outside this region. Erroneous jumps in the flux are visible at these transitions. The dashed lines depict the wavelengths of Lyα for D I (blue) and H I (red). The absorption line present in Feige 34 and Feige 67 integrations is H-β centered just to the red of a flux jump caused by the end of an echelle order. The wavelengths of D and H in our science spectrum lie on the edge of a region masked and interpolated through by the flux calibration routine in `makee` because of these H-β lines. Note also that the wavelengths of the flux jumps on the blue end of this plot appear to vary over time-scales of months, indicating a difference in echelle order coverage between observing runs (See section 3.2).

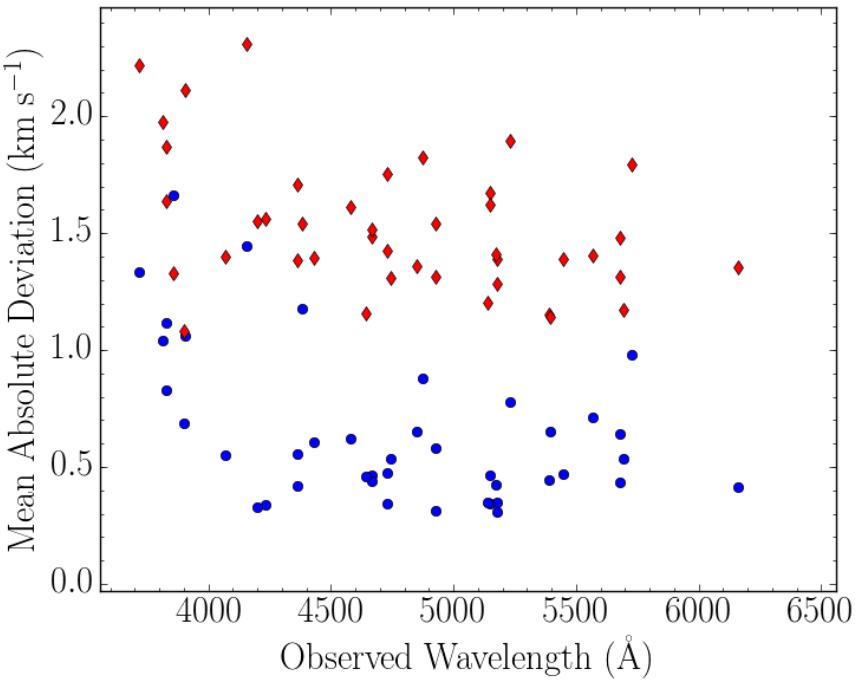

Figure 3.3. Metal line wavelength shifts in the 16 spectra, expressed as mean absolute deviation in velocity from the mean wavelength of a given diagnostic metal line before (red diamonds) and after (blue circles) corrections. When determining the correction factors to apply to the wavelength scales, outliers with an unusually large dispersion caused by poor fitting before the correction (not pictured) have poor diagnostic power of the velocity dispersion and so were eliminated from the correction procedure using simple 2σ clipping from the mean. The goal is to reduce the velocity offsets between integrations to the level where spectral features are lined up to within random error. The over all metal lines used, the overall mean went from 1.52 km s^{-1} before the correction to 0.65 km s^{-1} after.

separately from and prior to the above-mentioned procedure.

Echelle Order Wavelength Coverage

Among our standard star spectra, we discovered that the flux jumps caused by echelle-order ends did not line up in wavelength between all integrations. The absorption lines were found to be consistent within the error, suggesting that this error comes from echelle order wavelength coverage. While within a given observing run, the flux jumps lined up, over a period of months to years there was drift of up

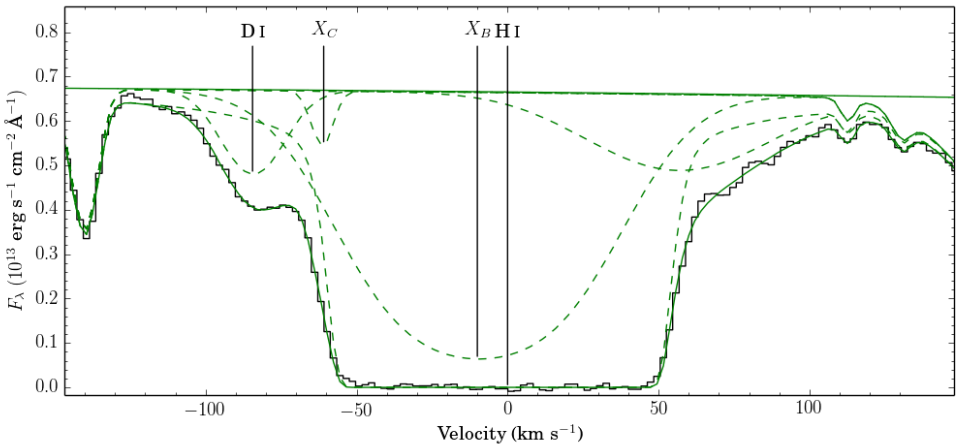

Figure 3.4. Model A of our Lyα system (see Table 3.2). Our two contaminants of interest are labeled 'X_C' and 'X_B'. An additional contaminant can be seen blending with the red edge of our main Lyα line, but does not have an effect on D/H and so is not studied in detail. Velocity here is defined as velocity from our dominant Lyα line at at λ =4848.6 Å.

to 1 Å despite using the same grating angles for all but one integration (see Figure 3.2). The flux error contribution to fitting D/H is addressed in section 3.4.1.

Measured Parameters

Here we report on measured parameters of our absorption system and methodology. For a detailed description of methodology, see chapter 2.

Velocity Structure

We found three models of contaminating absorption blending with Lyα, named models A, B and C in Table 3.2. Figure 3.6 shows that the there is a clear preference for a contaminant to lie at both -6 km s^{-1} and at -58 km s^{-1}, which we name X_B and X_C respectively, reflecting the model from which they arrive. Model A is the best fitting model, which includes both.

There was another absorber at about 55 km s^{-1} to the red of our H I, which

neither had an effect on N_{DI} nor on N_{HI}, since N_{HI} is already well constrained by many transitions of Lyman-series absorption and this absorber is too far in velocity from D I to have any effect. While it is included in the fit of all models, we do not include with with our analysis.

Model A

Model A was the best fitting, consisting of the one main velocity component that has by far the largest H I column and the only detectable D. It is distinguished from models B and C by having two additional contaminants that we name X_B and X_C. X_C is blended with the blue absorption edge of H I. X_B is much wider and much closer in velocity to H I, which we suspect to be an H I Lyα line with a column that is 10^3 times lower than the component that shows the D. Both X_C and X_B are fit assuming their oscillator strength is equal to that of the H I Lyα transition. Both of these contaminants are heavily blended into H I, however adding an absorber at these velocities produces a distinct improvement in the fit (see Figures 3.6 and 3.4).

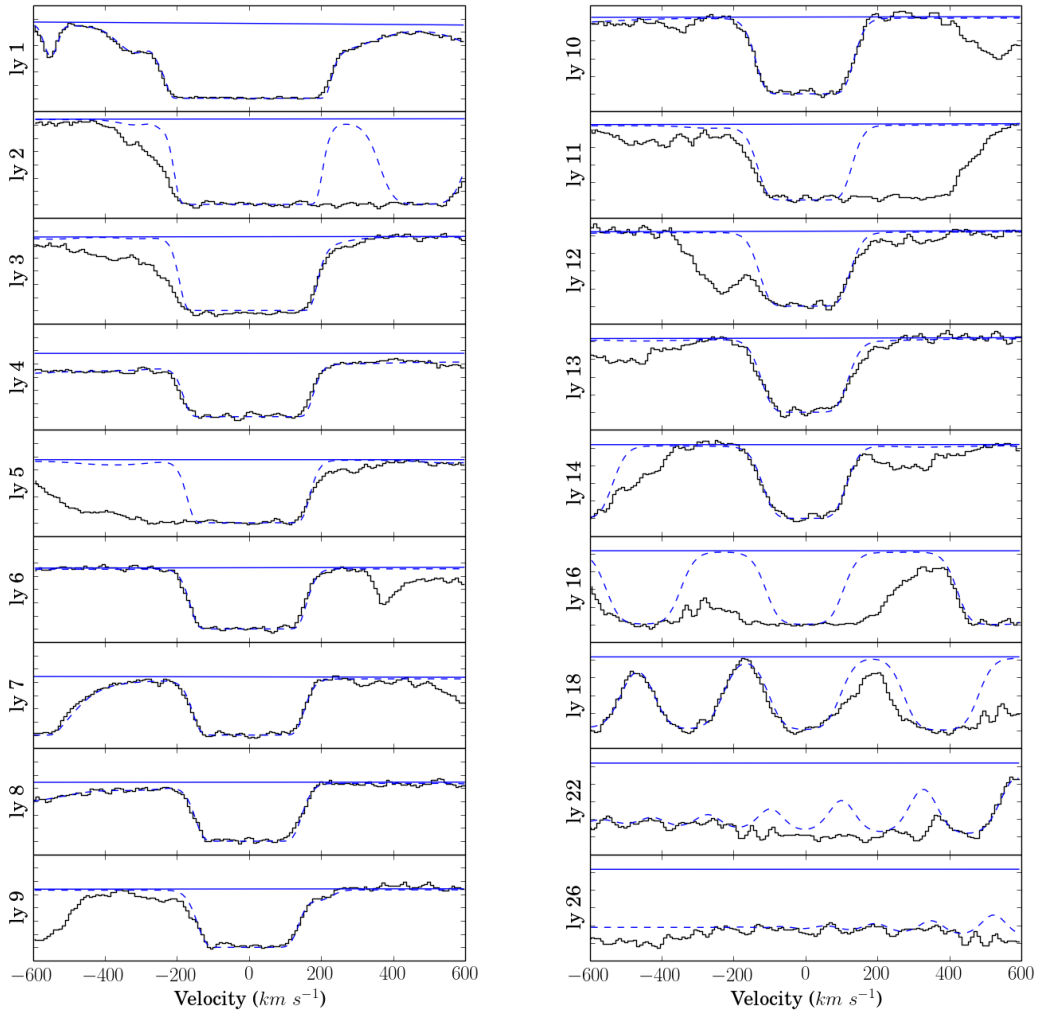

Figure 3.5. The Lyman-series for the $z_{\rm abs} = 2.98838$. The label on the y-axis represents transition such that 1 means Lyα, 2 means Lyβ and so forth. For fitting and parameter estimation, we optimized H I only over transitions exhibiting minimal blending.

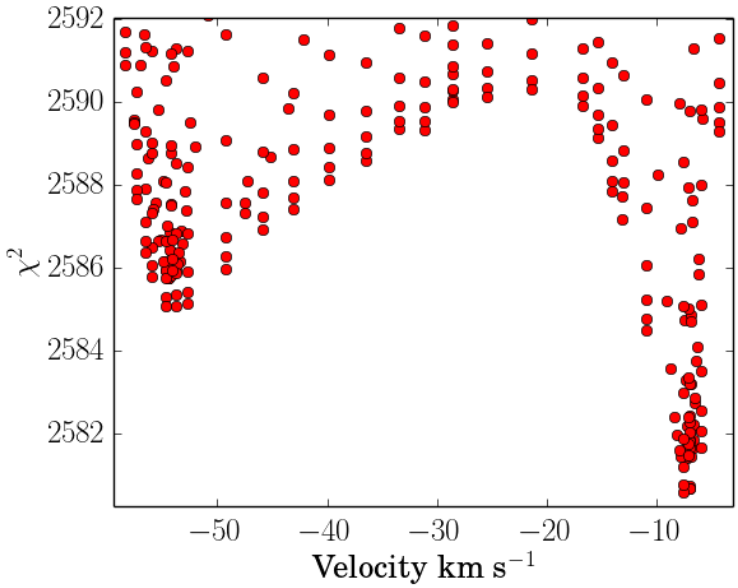

Figure 3.6. χ^2 versus the velocity of a single contaminating absorption line. The model includes 1108 pixels of Lyman-series absorption in the vicinity of the dominant Hydrogen at $z_{\rm abs} = 2.98838$, which we define as $v = 0$ km s^{-1}. We step the velocity of the single contaminant and at each velocity we optimize all free parameters to minimize the χ^2, using a best fitting continuum for each velocity. The rightmost minimum at -7 km s^{-1} corresponds to Model B and the leftmost minimum at -55 km s^{-1} to Model C. These values of χ^2 differ from those reported in Table 3.2 because they were fit considering many more degrees of freedom, including higher order Hydrogen Lyman-series absorption.

Table 3.2. Summary of our three fitting models for the D/H absorption system towards J1201+0116. Contaminants are unidentified absorption line that is likely a metal line, notated X_C and a Lyα line, notated X_B. Each model was fit using the same selection of spectrum as the optimization region during fitting which includes Lyα for D and H as well as select higher-order H I transitions, which exhibit clearly defined edges and minimal blending. Other contaminating absorbers blending with our selected transitions of H I contributed small amounts of absorption (equivalent to $N < 10^{13}$ if treated as Lyα lines) and were locked to a best fit value. If unidentified, a contaminant is fit as an absorber with the same oscillator strength as the Hydrogen Lyα transition. Each model fit its own best fitting continuum.

Model A ($\chi^2_{min} = 96$, 11 parameters, 100 pixels)

Ion	log N (cm^{-2})	1σ	2σ	b (km s^{-1})	1σ	2σ	velocity (km s^{-1})	1σ	2σ
H I	17.403	±0.006	±0.012	18.44	±0.04	±0.08	$z_{\rm H\,I} = 2.9883807$	$^{+0.0000006}_{-0.0000004}$	$^{+0.0000009}_{-0.0000013}$
D I	12.801	±0.030	$^{+0.055}_{-0.061}$	13.8	$^{+0.8}_{-0.7}$	$^{+1.1}_{-1.0}$	locked to $z_{\rm H\,I}$		
X_C	12.15	$^{+0.13}_{-0.19}$	$^{+0.25}_{-0.24}$	4.3	$^{+0.8}_{-1.2}$	$^{+1.9}_{-2.5}$	-58.9	±0.4	$^{+1.7}_{-1.5}$
X_B	14.10	$^{+0.13}_{-0.15}$	$^{+0.27}_{-0.38}$	37	$^{+3}_{-1}$	$^{+9}_{-4}$	-10	±2	$^{+4}_{-14}$

log D/H= -4.602 ± 0.031 (1σ) $^{+0.056}_{-0.062}$ (2σ)

Model B ($\chi^2_{min} = 112$, 8 parameters, 100 pixels)

Ion	log N (cm^{-2})	b (km s^{-1})	velocity (km s^{-1})
H I	18.403	18.45	z=2.9883806
D I	12.81	13.93	locked to H I
X_B	14.40	33.46	-7.0

Model C ($\chi^2_{min} = 124$, 8 parameters, 100 pixels)

Ion	log N (cm^{-2})	b (km s^{-1})	velocity (km s^{-1})
H I	17.347	18.81	z=2.9883782
D I	12.85	13.58	locked to H I
X_C	12.79	11.79	-58.2

Model B and C

Models B and C give similar χ^2, and both are significantly worse fits than Model A. Both Models B and C exhibit the need for both of these contaminants to be included in our reported velocity structure. As the column density of X_B decreases, the fits of the models converge to model C and N_{DI} is maximized. As the column density of X_B increases, the fits of the models converge to model B, which has a value of N_{DI} 1σ above that of model A.

Although we fit X_C in Table 2 using the oscillator strength it would have if it were H I, the fits find $b = 3.2 \pm 0.8$km s^{-1} (model A) and $b = 12.0 \pm 1.2$km s^{-1} (model C), both below the values normally found for H I lines, so it is likely that X_C is a metal line. We attempted to identify X_C by fitting all Lyα lines observable in our data with $N > 10^{14}$ cm^{-2} as well as major metal lines associated with the damped Lyman-alpha line at $z_{abs} = 2.68$. This includes all possible Lyα lines from the Lyman limit from our $z_{\rm abs} = 2.98838$ system to the Lyman emission peak of the QSO, corresponding to a redshift range of $1.9 < z < 3.2$. We then compared this information to a dictionary of all potential metal lines associated with each off these systems to within 50 km s^{-1} of the wavelength of X_C. We were unsuccessful at identifying the line, though it may be associated with Lyα absorption obscured by other Lyα forest absorption or absorption at a lower redshift than our data permits us to detect.

Both X_C and X_B effect N_{DI} by contributing a portion of the absorption near D. By comparing models B and C, we see that X_B contributes more of this absorption, since N_{DI}(model C)>N_{DI}(model B). In model A, both N(X_C) and b(X_C) are smaller than that of model C. This reflects the fact that in model C, X_C contributes more total absorption since X_B is not present. From model A to model

B, $b(X_B)$ decreases while N(X_B) increases in order to account for the different line profile required to fit the same data in the absence of X_C.

Other Models Explored

To ensure the no more complicated families were preferred, we iteratively added more absorbers at random velocities around Lyα until no further improvement in fit was possible. Other model families tested had a tendency to converge to model A. The fitting software throws out extraneous absorbers by either setting their column density below some detectable level (about N=10^{10} cm^{-2} for Lyα) or by shifting the velocity of the absorber to outside the optimization region. Some unsuccessful models included:

- Contaminants just blue of D on the absorption edge
- An additional contaminant between X_C and D in velocity
- An additional H I just red of our main H I system

The contaminants from the first two were spontaneously thrown out by our fitting program. The last of these was not thrown out, but had no effect on the fit, since it is so close in velocity to two stronger absorbers. Applying this last contaminant to model C (no X_B), the contaminant tended to shift to the velocity of X_B, when free to vary, showing that model A is indeed the preferred model.

Lines Blending with Other Transitions of HI

Due to the complex absorption of the Lyα forest , we should expect many absorbers to blend other observed transitions of H I. For the purpose of determining errors on H I, we only considered transitions where the line profile was dominated by H I. We iteratively added new absorbers until the fit ceased to improve or the software threw out absorbers. None of these had a significant effect on D/H.

Table 3.3. Summary of measured fitting parameters for metal absorbers observed towards J1201+0116 at $z = 2.988$. Errors reported here are statistical (1σ) fitted over a predetermined best-fitting continuum. The last table reports the maximum column density allowed for the absorber to remain below our detection threshold, due to noise and contaminating absorption. These undetected absorbers were locked to $z_{\rm abs} = 2.98838$ and a b-value which reflects the assumption that the thermal, turbulent and instrument contribution to the line width is the same as that of D and H.

No velocity assumptions made

	log N (cm^{-2})	b (km s^{-1})	velocity from H I (km s^{-1})
C III	12.4 ± 0.02	$11.9^{+2.6}_{-0.9}$	-4.3 ± 0.3
C III	11.81 ± 0.10	4.1 ± 0.7	-5.0 ± 0.4
Si III	$11.52^{+0.12}_{-0.10}$	6 ± 2	$+4.2 \pm 1.1$
Si III	11.82 ± 0.05	11 ± 2	-4.3 ± 0.6
	χ^2=47	55 pixels	9 parameters

Nearby Neutral Hydrogen and Effect on Continuum

$150 - 300$ km s^{-1} to the red of H I, there was a complex absorption system consisting of about 6 closely spaced absorbers with column densities in the range $11 <$log N$_{\rm HI} < 15.5$ cm^{-2} at redshift $z_{abs} \sim 2.991$. While their physics is not relevant to this paper, they did affect the continuum level to the red of our dominant H I absorber, so they were included with the fit, but not reported with our results. The velocities of the most important three of these absorbers were determined by best fit over Lyα, Lyβ and Lyγ absorption. N I absorption was detected for three of these systems, which provided some guidance as to their velocities, however no other metal absorption was immediately able to be detected for these blending systems. The associated N I were on the order of $b < 15.$ km s^{-1} and log N < 13.4 cm^{-2}.

Table 3.4. 2σ upper limits to column density estimated by measuring maximum possible equivalent width at the reported rest-frame wavelength at $z_{\rm abs} = 2.98838$. We assume at least half of the absorbed photons are absorbed due to our C III and Si III lines in order to set lower limits on column density.

2σ Upper limits on column density			
	log N (cm^{-2})	rest-frame wavelength (Å)	50% lower limit:
C I	< 13.27	1328.8	
C II	< 12.76	1334.5	
C III	< 12.26	977.0	> 11.88
C IV	< 11.63	1548.2	
Si II	< 11.65	1193.3	
Si III	< 11.40	1206.5	> 11.10
Si IV	< 11.38	1393.8	
O I	< 12.36	1302.2	
O VI	< 12.28	1031.9	

Sources and Analysis of Error in D/H

Systematic Errors from Continuum Level

We generate 523 random continua and find that the continuum level does not have an effect on our estimate of $N_{\rm DI}$. Since only the Lyα transition was observed in Deuterium for this system, we expected the column density of D I is sensitive to the continuum level here.

To generate continua, we perturb both continuum control points and parameter values for absorbers in the vicinity of Lyα along a Gaussian distribution with standard deviation equal to our previously determined parameter errors for parameters, and a conservative initial guess of 3% for continuum control points. We then alternate between optimizing continua and parameter values until the optimizer finds an approximate local minimum of χ^2. We have only one control point on either side of Lyα to prevent non-physical inflection points from appearing.

Figure 3.2 shows that the instrument has a well-behaved response in the

vicinity of Lyα, which is decreasing almost linearly, so there should be no flux artefacts introduced by the instrument. Furthermore, the quasar at $z_{em} = 3.233$ should not have any emission lines at these wavelengths. It is, therefore, reasonable to assume that the quasar continuum is flat within our spectral region of interest, 4844 Å and 4854 Å.

Since the fit of our dominant H I absorber is well constrained by many transitions of Lyman-series absorption, we lock N_{HI}, $b_{H\,I}$ and $z_{H\,I}$ to their respective best fit values. The continuum is constrained by unabsorbed flux to the blue of our D I Lyα line as well as 400 km s^{-1} to the red of D I. Contaminants X_C, X_B and other contaminants in the optimization region remain free to vary about model A throughout the continuum sample, since their fits have an effect on the continuum around Lyα.

Examining the relationship between our contaminating absorbers, continua and D we find the following:

- Increasing the amount of absorption by X_B in model A beyond the best-fit value did not change N_{DI}, but did cause the absorption by X_C to vanish, consistent with model B.

- Decreasing the amount of absorption by X_B in model A increased N_{DI} and the amount of absorption by X_C, consistent with model C.

- Models A, B and C all preferred similar continua around Lyα, well within the range presented in Figure 3.7.

- The effect of varying the continuum level was indiscernible from random measurement error.

Our continua sample show that the continuum contribution to error on

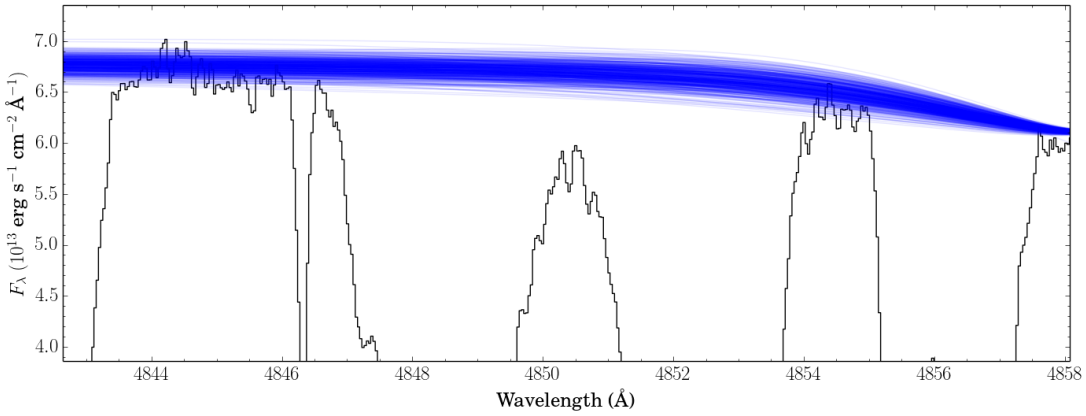

Figure 3.7. The 523 continua considered for estimation of the effect of continuum choice of D/H error in the vicinity of Lyα. The 2σ continua uncertainty is 3% at λ = 4847.25 Å, beyond which the goodness of fit suffered significantly. In determining these continua, the fitting parameters for H I were locked since its fit is already well constrained by many observed Lyman-series transitions (see 3.4.1).

Table 3.5. The effect of the continuum level of model A at the wavelength corresponding to the center of the D Lyα line at λ =4847.25 Å from a sample of 523 randomly generated continua. The 2σ continuum level uncertainty is 3%. The value of N_{DI} is almost exactly equal to our value reported considering only the best-fit continuum with almost identical errors (see Table 3.2), suggesting that the error is dominated by statistical error.

	best $\pm 2\sigma$	minimum	maximum
log N_{DI} (cm^{-2})	12.80 ± 0.07	12.69	12.87
$b_{D\,I}$ (km s^{-1})	14.2 ± 0.6	12.2	15.5

N_{DI} is completely consistent with the statistical error. We were unable to obtain more extreme values of N_{DI} by varying the continuum without the goodness of fit suffering significantly.

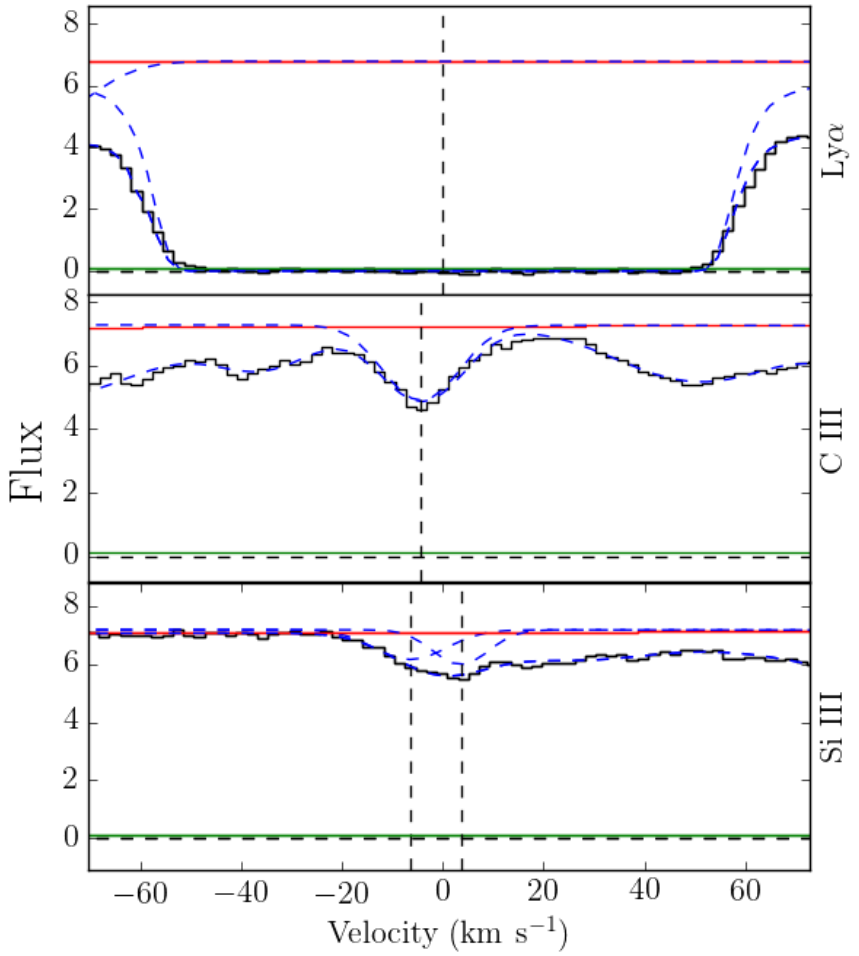

Figure 3.8. Observed metal lines towards J1201+0116 with velocities defined with respect to $z_{\rm abs} = 2.98838$, making no assumptions about velocity structure. The dotted line on the bottoms denotes zero flux, the green line the flux error in each pixel, the red line denotes continuum and the dotted blue lines indicate the fit to the absorption.

Gas Properties

Metal Abundances, Ionization and Inferred Gas Properties

We discovered no absorption for any common ions and instead fit upper limits to the column densities of ionizations of Si, C and O at redshift $z_{\rm abs} = 2.98838$ with b chosen under the assumption that it is part of the same gas as H I; specifically we set $b(C) = 8.1$ km s^{-1}, $b(Si) = 7.2$ km s^{-1} and $b(O) = 7.7$ km s^{-1}, where these values reflect the assumption that $b^2_{turb} + b^2_{inst}$ is unchanged and that the gas temperatures are the same as in H and D. These upper limits were determined by the amount of absorption present in regions where spectral lines would be expected. The tightest constraints were naturally found when an ion was expected to exhibit strong lines at wavelengths where our spectra showed no absorption whatsoever, such as with C IV.

C III and Si III Without Velocity Assumptions

There was absorption at the correct wavelengths to be C III $\lambda = 977.02$ Å and Si III $\lambda = 1206.5$ Å, however since these ions only exhibit one transition, this could not be corroborated. Nevertheless, we attempt to fit this absorption assuming all of it comes from C III and Si III(see Table 3.3).

C III is relatively simple with two components at near identical velocities. Our $v = -4.3$ km s^{-1} of C III has a column density consistent with our upper limits when locking velocity and b, however the best estimate is about 0.2 dex higher in column and b is significantly higher. The discrepancy in b-value would suggest that this component may be coming from different gas.

Si III can still fit it with two components; one to the red of $z_{\rm abs} = 2.98838$ and one to the blue, as well as several more less interesting components further off

to the red. None of the velocities for any of these components are consistent with our H I to within error, however the column and b-value of our $v = -4.3$ km s^{-1} is completely consistent with our estimate of the upper limit with locked b-value. However, since the velocity is not consistent, we cannot draw any conclusions.

Including these -4.3 km s^{-1} components to our fit of b^2 versus mass (Figure 3.9), we find that Si III agrees well with D I and H I, however C III disagrees by more than 2σ.

Further complicating our identification of C III, the wavelength at which we observe C III is also consistent with O VI $\lambda = 1032$Å associated with H I absorption at $z = 2.7749$ with $N_{HI} \sim 10^{14.4}$ cm^{-2} with the weaker $\lambda = 1038$Å line of the doublet unconstrained by unrelated absorption. Since no other common metals were observed in this system, it is difficult to estimate how much of the pollution in our C III line, if any, is due to O VI.

Due to the above complications, we use the simple assumption that half of the absorbed photons are absorbed due to our observed lines, corresponding to $N_{lower} = N/2$. Since these two lines are very strong, with oscillator strengths of $f(Si\,\mathrm{III}) = 1.67$ and $f(C\,\mathrm{III}) = 0.762$ (Morton, 1991), it would be odd for the absorption to not have any contribution from these lines.

Upper Limits on Metal Absorber Column Densities

We calculate 2σ upper limits on the column density of our metal lines using the equivalent width. For line on unabsorbed regions of spectrum, this is set by the S/N ratio, SNR.

Assuming Poisson statistics, mean counts for each pixel in a region without absorption is $\bar{n} = \mathrm{SNR}^2$. Comparing mean counts expected without absorption to counts from observed flux, we calculate an equivalent width, and thus a column

density under the approximation, $EW \propto N$.

The tightest constraints are set by those transitions with a greater oscillator strength and those in higher-SNR regions without absorption. Our upper limits of column density are reported in Table 3.4.

We calculate the total observed,

$$n_{obs} = \bar{n} \sum_i \frac{F_i}{\bar{F}_0} \tag{3.1}$$

where is the mean number of counts when no absorption is present, assuming they follow a Poisson statistics, F_i is the observed flux in pixel i, $\bar{F}_0$ is the average continuum-level and $EW(N)$ is the equivalent width of the line in question in pixels.

With no absorbers, we would expect to find $n_{exp} = n_{pix}\bar{n}$ counts, where n_{pix} is the number of pixels in our flux sample (spectral direction) and $\mathrm{SNR}^2 = (\bar{n}/\sqrt{\bar{n}})^2 = \bar{n}$ is the mean number of photon counts in per pixel at the wavelength in question in absence of absorption (flux in units of counts). This assumes that the small spectral region of the line being tested has a flat flux response. In pixels, our equivalent width of an absorber is then,

$$\begin{aligned} EW(n_{obs}, n_{exp}) &= \frac{n_{exp} - n_{obs}}{\bar{n}} \\ &= n_{pix} - \sum_i \frac{F_i}{\bar{F}_0}. \end{aligned} \tag{3.2}$$

and from this, we calculate a maximum allowed column density,

$$N_{max} = \frac{4\epsilon_0 m_e c^2}{f \lambda_{rest}^2 e^2} (EW + 2\sigma(EW)) \tag{3.3}$$

where m_e is the electron mass, e is the elementary charge, v_{disp} is the pixel width

in velocity and λ_{rest} is the rest frame wavelength of the line in question.

Estimating Temperature from Observed Line Widths

We attempt to estimate gas temperature using the different fits to our two observed metal lines.

Using the -4.3 km s^{-1} components of the models with no velocity assumptions made (see Table 3.3) we fit our observed widths (Figure 3.9) and find that Si III agrees with D I and H I, however C III disagrees by more than 2σ.

Using the models with no velocity assumptions made, using both the Si III and C III reported in Table 3.3 with velocities of 4.3 km s^{-1} from $z_{\rm abs} = 2.98838$, we estimate a temperature of 17100 ± 800 K and $\sqrt{b_{turb}^2 + b_{inst}^2} = 8 \pm 3$ km s^{-1}. Keck HIRES has a FWHM on the order of $6 - 8$ km s^{-1}, so b_{inst} is 3.6–4.8 km s^{-1} and b_{turb} is 3.6–9.3 km s^{-1}.

Photoionization Calculations

Photoionization calculations suggest a low metal abundance system with a high degree of ionization. We ran a grid of Cloudy simulations (version 13.01 (Ferland et al., 2013)) assuming plane-parallel geometry and an isotropic ionizing radiation field using a Haardt-Madau spectrum at $z = 2.988$ (Haardt and Madau (2012)). We assume pop II relative elemental abundances for our calculations, by taking solar relative abundances and boosting the relative Si abundance by a factor of two. Our models varied over different ranges of total Hydrogen number density ($n_{\rm H}$), H I column density and metallicity (Z). Results were constrained by observed values of $N_{\rm H\,I}$ and our upper limits of column density for different ionizations of C, Si, and O. See Table 3.6 for a summary of results.

Our upper limits of column density on C, Si and O suggest a highly ionized system and the high temperature inferred from H and D b-values are consistent

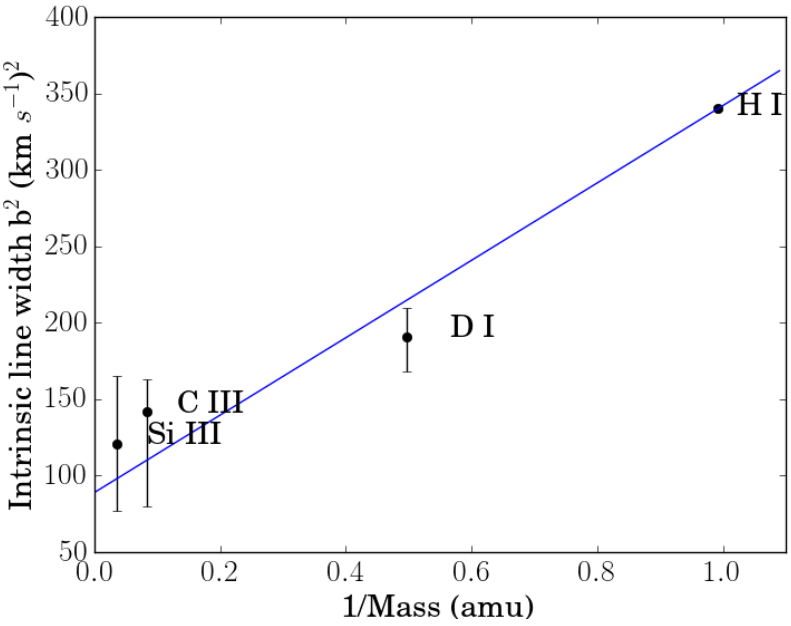

Figure 3.9. Observed line width versus inverse atomic mass. Line width is just the quadratic sum of thermal, instrumental and turbulent broadening. The slope of this line is then $2k_bT$ and the y-intercept is turbulent and instrumental broadening combined in quadrature. The slope of this line suggests $T = 30000 \pm 3000K$ whereas the intercept gives a non-thermal component of $b_{non-thermal} = 9.4 \pm 1.3 kms^{-1}$, where this contribution includes instrumental and turbulent broadening. The slope and intercept were calculated using simple linear regression weighted by $1/\delta b^2$. Si III was excluded from this calculation as it was more than 2σ from the best-fit line.

with this. The lower limits on C III and Si III helped to set a lower limit on n_H, upper limit on U and lower limit of Z, but did not contribute to our upper limit of Z, which was particularly constrained by the upper limits of Si II and Si III.

The unusually low metal abundance suggests a pristine system, which supports our value of D/H being representative of the primordial value. Since our value of D/H is consistent with other values from literature with much larger metal abundances, this supports the values of D/H reported in literature (Table 5.3) not changing with metal abundance.

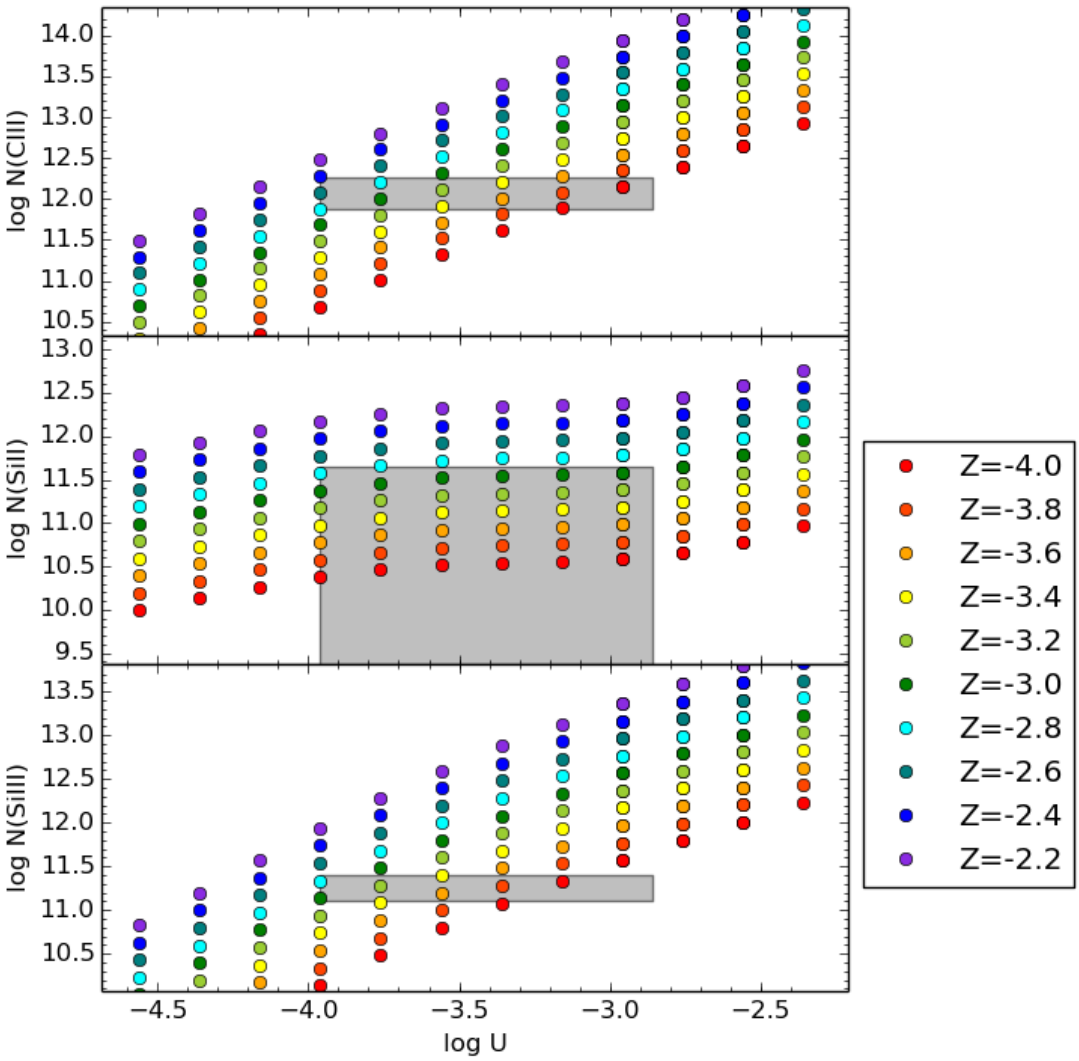

Figure 3.10. Log-column density versus log-ionization parameter for several different metallicities from Cloudy simulations. Models were constrained to fit the observed column density limits for the tested ions of Si, C and O, producing the allowed region (grey). The upper limits are emphasized with the dashed black line.

Table 3.6. The summary of gas properties from a running a grid of photoionization models (Ferland et al., 2013) and comparing to our observed values for column density and line width. All abundances are expressed with respect to solar abundances. These models yielding these parameters were constrained by observed values of line widths and column densities of Si III, C III and H I as well as the upper limits for column densities of unobserved ionizations of C and Si. The upper limits on C, Si and O content is to 2σ significance based on upper limits from measured column densities in the data and the lower limits assume that at least 50% of the observed absorption is due to gas associated with our system of interest (see Section 3.5.1). The ionization parameter, U, is defined as the number density ratio of ionizing photons to Hydrogen at the incident face: $U = n_\gamma / n_H$.

Quantity	Value
Temperature from observed widths	30000 ± 3000 K
Temperature from cloudy	15000 ± 2000 K
$\sqrt{b_{turb}^2 + b_{inst}^2}$	8 ± 3 km s^{-1}
turbulent contribution to line width	$3.6 < b_{turb} < 9.3$ km s^{-1}
[O/H]	< -3.2
[C/H]	-3.5 ± 0.8
[Si/H]	-3.3 ± 0.8
[H I/H]	-1.9 ± 0.6
$Z/Z_\odot$	$10^{-3.5 \pm 0.8}$
ionization parameter: log U	-3.4 ± 0.6
Total hydrogen number density	$10^{-1.5 \pm 0.6}$ cm^{-3}
length of line of sight through gas	0.3 ± 0.5 kpc

D/H Abundance Ratio

Statistical error was determined to be the dominant error component. Even having only one measurable transition of D I that is partially blended with a contaminant, our data permit us to estimate the D I column density of absorption to a few percent precision. We estimate a value of

$$\mathrm{D/H} = (2.50 \pm 0.18) \times 10^{-5} \tag{3.4}$$

$$\log\ (\mathrm{D/H}) = -4.602 \pm 0.031, \tag{3.5}$$

where our errors reported here are 1σ.

Due to the number of clear, uncontaminated Lyman-series transitions, our fit for H I can be constrained to excellent precision. Figure 3.5 shows the Lyman series for selected transitions. Unblended regions from selected transitions were used for the optimization and χ^2 analysis. Specifically, we chose transitions 1, 4, 6, 7, 8, 9, 10, 12, 13, 14, 15, 18, 19, and 20, where 1 corresponds to Lyα ($n = 1 \rightarrow 2$), 2 to Lyβ ($n = 1 \rightarrow 3$) and etc.

Acknowledgements

This chapter was adapted from work being prepared for publication under the working title *The Deuterium abundance in pristine gas towards QSO J1201+0116 : new evidence that we are observing the primordial D/H abundance*. The author of this dissertation is the primary author and David Tytler is co-author.

The author wishes to recognize and acknowledge the very significant cultural role and reverence that the summit of Mauna Kea has always had within the

indigenous Hawaiian community. We are most fortunate to have the opportunity to conduct observations from this mountain.

The data presented herein were obtained at the W.M. Keck Observatory, which is operated as a scientific partnership among the California Institute of Technology, the University of California and the National Aeronautics and Space Administration. The Observatory was made possible by the generous financial support of the W.M. Keck Foundation.

Chapter 4

The Deuterium-to-Hydrogen Ratio Towards QSO J0744+2059

This chapter reports on the measurement of D/H in a DLA towards a QSO with J2000 coordinates, 07:44:37.52+20:59:00.19. This object is somewhat dimmer than J1201+0116, with a V-band magnitude of 18.78, however, it exhibits many clear transitions of D I visible up to the Lyman limit and Lorentzian damping wings about Lyα, providing yet another object, which passes the selection criteria suggested by Cooke et al. (2014). It is also interesting to note that this system has the largest H I column density reported in D/H literature, slightly larger than the system at $z_{\rm abs} = 2.70242$ towards J1558–0031 O'Meara et al. (2006); Cooke et al. (2014).

We find a best fit with one component of D and H with 3.6% error on the abundance ratio, 10^5D/H$= 2.359 \pm 0.095$ (68 % CL). Despite this precision, our value of D/H is lower than the CMB value: ($2.606^{+0.051}_{-0.054} \pm 0.13 \times 10^{-5}$, (95% CL)) (Planck Collaboration, 2015) by about 2.1σ and 1.7σ lower than the combined value reported in Cooke et al. (2014): ($2.54 \pm 0.04 \times 10^{-5}$).

Observations

Quasar J0744+2019 was observed under several different observing programs using the High-Resolution Echelle Spectrograph (HIRES) at W.M. Keck observatory (Vogt et al., 1994). All observations made use of either the C1 or C5 deckers with slit widths of 0.861" and 1.148", respectively. Our combined spectrum has SNR=28 near Lyα, compared to SNR=40 for J1201+0116. See Table 4.1 for a summary of observations. We make use of Tom Barlow's MAKEE[1] for extraction and reduction and use in-house software for further corrections as needed. These further corrections include additional bias-level subtraction and small velocity corrections (sections 1.1.1 and 1.0.1). We combine 12 integrations of the QSO summing to a total integration time of 59250 seconds.

Table 4.1. Individual integrations of J0744+2059. We use 61 narrow metal lines spanning the entire spectrum to calculate the relative shift of each spectrum. The measured velocity shift had a linear relation to wavelength and so we applied the appropriate correction to the log-linear wavelength scale accordingly. r and p are the correlation coefficient and the Pearson p-value, respectively, for a linear fit to mean velocity versus wavelength.

		start time	Integration	mean velocity	best fit of shift from mean	
id	Date Y-M-D	(UTC)	Time (s)	shift (km s^{-1})	r	p
261	2009-01-20	08:11:32	5400	0.20 ± 2.59	0.04786	0.74665
086	2008-03-28	05:32:32	1400	-2.57 ± 15.73	-0.03288	0.81520
193	2008-01-13	08:20:16	3600	-0.85 ± 11.41	0.00547	0.96752
256	2009-12-12	12:57:49	5100	0.99 ± 2.32	0.30727	0.02996
087	2008-03-28	05:56:33	3600	-0.08 ± 2.56	-0.32757	0.02158
224	2008-02-22	05:23:39	3600	-0.21 ± 2.94	-0.40360	0.00490
260	2009-01-20	06:40:46	5400	0.77 ± 3.38	0.14390	0.33455
088	2008-03-28	06:59:29	3600	0.51 ± 2.20	0.05136	0.73464
225	2008-02-22	06:25:21	3600	-0.20 ± 3.08	-0.29591	0.05708
116	2008-02-20	05:41:34	3600	0.47 ± 3.94	-0.16012	0.28232
252	2009-12-12	11:07:54	5400	0.65 ± 2.32	0.21369	0.12822
413	2009-12-13	13:07:02	4950	0.30 ± 2.32	0.12024	0.40555

[1] `makee` is available at:
http://www.astro.caltech.edu/~tb/makee/

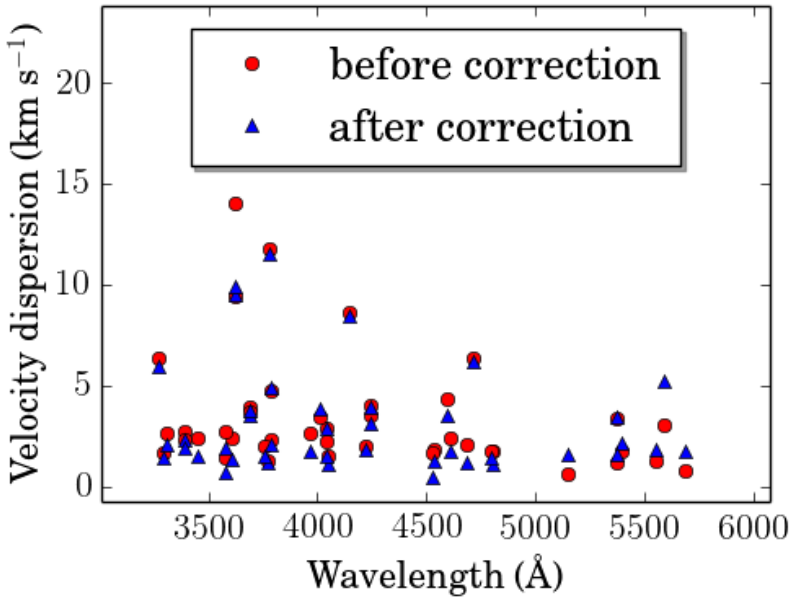

Figure 4.1. The velocity dispersion between integrations of J0744+2059 before and after our wavelength scale correction. The difference here is negligible, likely because this object is dimmer and thus has a lower SNR than J1201+0116, so the accuracy of the velocity estimates of each of our diagnostic metal lines suffered.

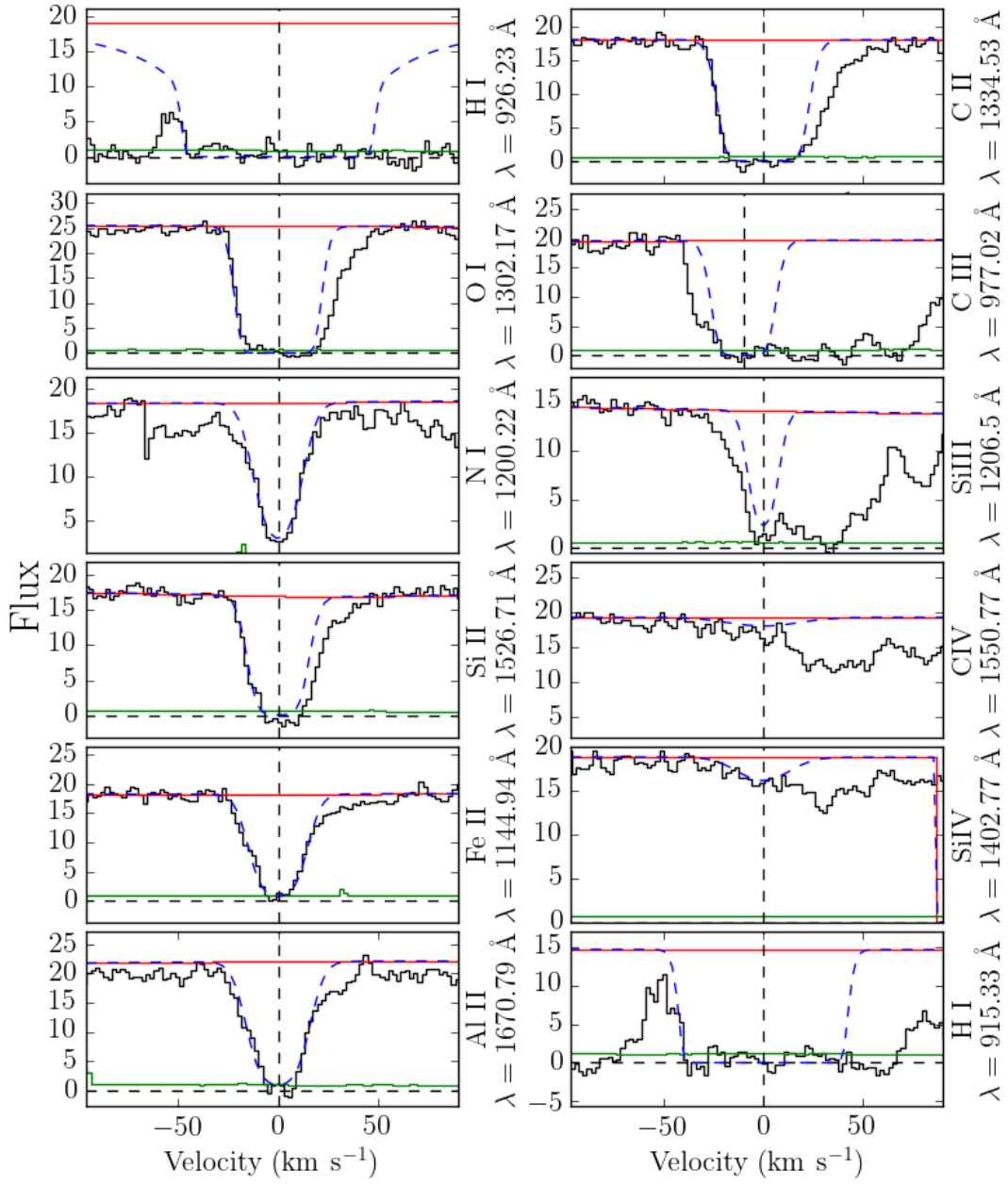

Figure 4.2. Selected metal lines in our spectrum as well as Lyα and our H I at $\lambda = 915.5\mathring{A}$ at $z_{\rm abs} = 2.98838$ towards J0744+2059. The dashed back lines represent the line centers, the dashed blue line represents the fit to absorption and the red line represents our continuum. We only fit all systems relevant to D/H, so we did not attempt to accurately measure H I blended to the red of our DH system for the purposes of this plot.

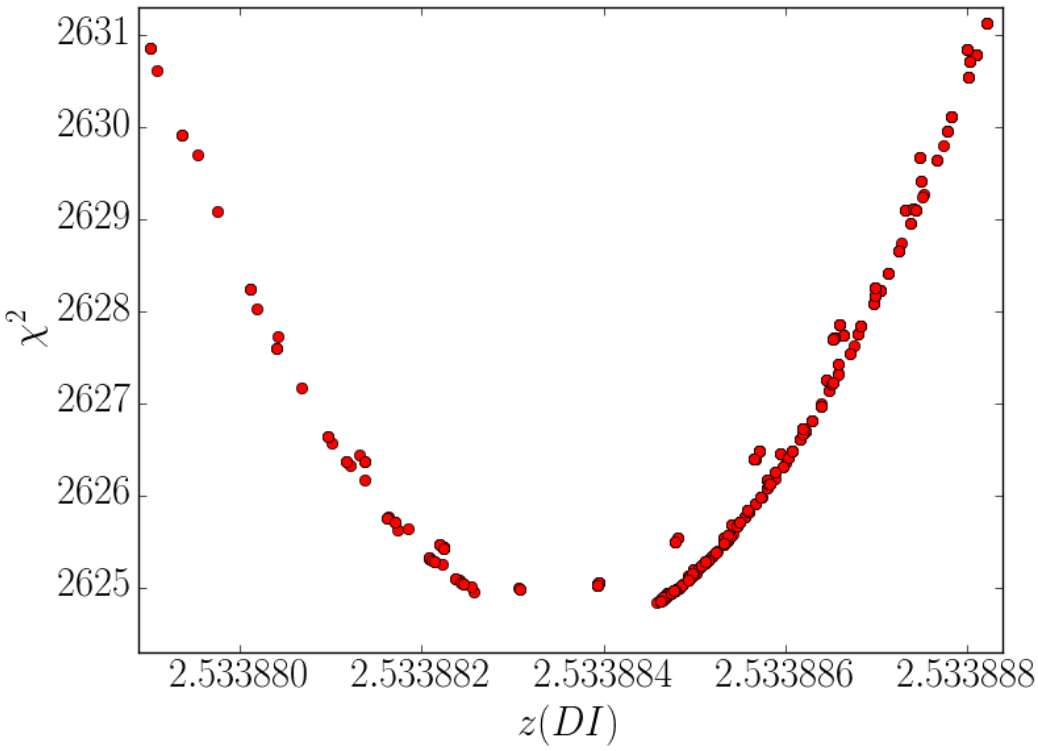

Figure 4.3. Redshift of our D I absorber. Using many transitions of D I up to the Lyman limit, some of which are unsaturated, allowing good precision, we find $z_{abs} = 2.5338836 \pm 0.0000015$ corresponding to an uncertainty of 0.25 km s^{-1}. We lock all metal lines and H I to this redshift for the remainder of the analysis.

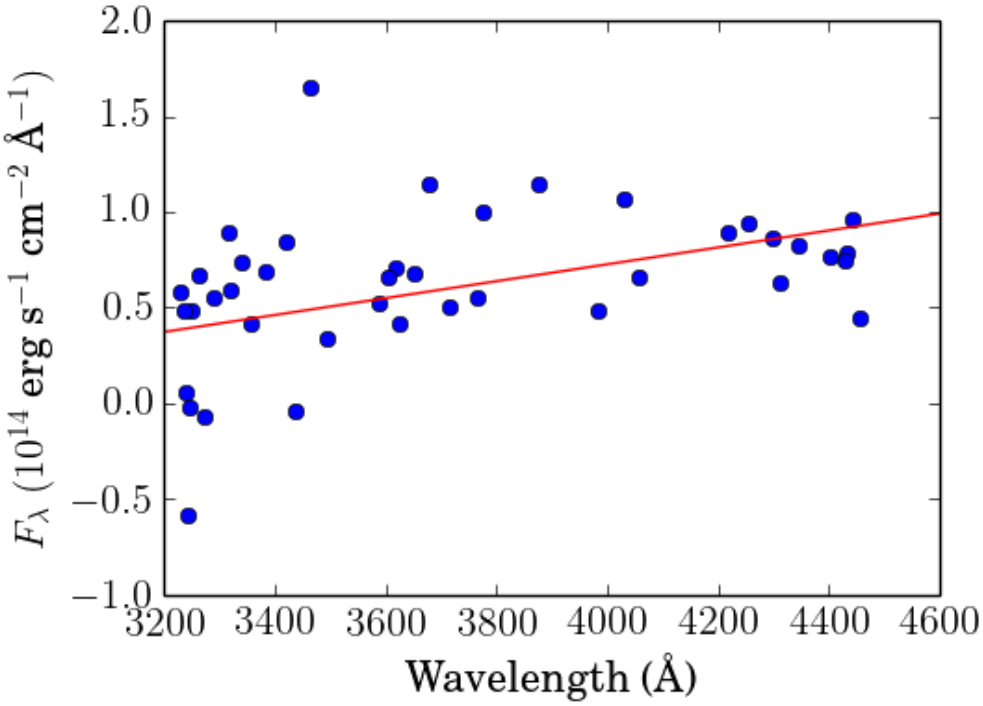

Figure 4.4. Residual flux in the cores of saturated Lyα forest lines versus wavelength from the Spectrum of J0744+2059. This is calculated to calculate a flux correction function to our spectrum to account for an anomalous flux discovered in line cores. This correction ends up being very small and does not effect our estimate of D/H.

We attempt to measure and correct for any velocity dispersion between integrations using 61 diagnostic metal lines and find that our velocity drift correction makes little difference (see section 1.0.1 and figure 4.1). The velocity dispersion improves from 4.10 km s^{-1} to 3.77 km s^{-1} and the change in line-width dispersion remains unchanged at $\sigma(b) = 13.74 - 13.73$km s^{-1}. With lower brightness, it was more difficult to fit these diagnostic metal lines, resulting in an inherently higher dispersion in these metal lines from integration-to-integration. Regardless, we apply what little correction we can.

Table 4.2. Summary of measured absorption parameters for the $z_{abs} = 2.5338836$ system towards J0744+2059. 1σ confidence intervals were estimated using χ^2 methods. Our H I and D I estimates include a freely varying continuum while confidence intervals on metals only include a best-fit continuum for simplicity. Errors on N(H I) were detemined using the extended Lorentzian damping wings after the best fit value was determined to be in agreement with other methods of estimating N(H I). All Absorbers were locked to $z_{\rm abs} = 2.5338836$, after having determined this value from unsaturated D I transitions

Ion	log N (cm^{-2})	b (km s^{-1})
H I	20.7903 ± 0.0038	14.06 ± 0.04
D I	16.163 ± 0.017	12.84 ± 0.16
O I	$15.73^{+0.03}_{-0.04}$	10.43 ± 0.11
C III	$13.84^{+0.04}_{-0.050}$	16.4 ± 0.5
N I	14.130 ± 0.006	$11.71^{+0.09}_{-0.23}$
C II	15.05 ± 0.6	$10.82^{+0.17}_{-0.32}$
Si II	14.34 ± 0.02	$10.63^{+0.12}_{-0.05}$
Si III	$12.74^{+0.04}_{-0.05}$	$8.2^{+1.0}_{-0.8}$
Fe II	14.277 ± 0.010	11.23 ± 0.15
Al II	12.84 ± 0.03	$13.1^{+0.5}_{-0.6}$
10^5D/H	2.359 ± 0.095	
log D/H	-4.627 ± 0.017	

Measurements

Velocity Structure

We find a simple one-component system fits our data well ($\chi^2/dof = 1.86$). Since since all well-determined metal lines and H I transitions are saturated, we use unsaturated D I lines nearing the Lyman limit to estimate the velocity of our system. (see figure 4.3). We find $z_{\rm abs} = 2.5338836 \pm 0.0000015$ or, expressing the uncertainty in velocity: ± 0.25km s^{-1}. For the remainder of this analysis, we lock all absorbers to this redshift.

There were several sub-dominant H I systems of higher ionization blended to the red of D/H system, inferred from observed C IV and Si IV absorption. We locked H I absorbers to the redshift indicated by C IV and Si IV and attempted fits. These strongest of these systems showed $\rm N_{C\,IV} < 10^{13.6}$ and $\rm N_{Si\,IV} < 10^{12.5}cm^{-2}$. The associated H I systems exhibit column densities that are negligible in comparison to the D/H systems, however, the strongest of these systems did contribute to the red edge of the Lyγ and higher transitions. It's column density was determined to be $N_{\rm H\,I} = 10^{17.3}{\rm cm}^{-2}$, and then locked for the remainder of the analysis.

Continuum Models

Following the methods discussed in Chapter 2, we study the impact of varying the continuum. Determination of continuum level about Lyα is of particular importance, since the damping wings of Lyα provide the tightest constraints on $\rm N_{HI}$. There are no known emission lines within range of our DLA from the Quasar ($z_{em} = 2.6786$), however there do exist echelle order joins, which can cause flux mismatches due to the flux calibration instabilities exhibited by HIRES (Suzuki et al., 2003). While we know the wavelengths of the order joins, having

taken standard star spectra with minimal absorption on the same night with the same setup as each integration, we fit our continuum under the assumption that the response is smooth. Of the surviving continua generated by our continuum generating procedure, we found that they varied by up to 1.1%.

Determination of N(HI) and N(DI)

We determine N_{HI} to good precision using the extended damping wings up to 5000km s^{-1} from the line center. These damping wings are not significantly blended with any other major systems and so serve as a good constraint. Considering only the damping wings, we find log $N_{HI}= 20.7903 \pm 0.0038$.

Due to the potential continuum error from the above mentioned flux instabilities, we also measure N_{HI} with many series of Lyman series absorption, which is less sensitive to the flux instabilities, though yields less precision. Considering only Lyman series absorption from Lyγ to the Lyman limit (915 Å), we find log $N_{HI}= 20.791 \pm 0.015$, which is in good agreement with our estimate using only the Lyα damping wings.

As a final check, we compare our value to two survey studies, both utilizing data from the Sloan Digital Sky Survey. Specifically, Prochaska et al. (2005) report log $N_{HI}= 20.80 \pm 0.15$, which agrees with our results, and Schneider et al. (2007) report log $N_{HI}= 20.672$, but did not estimate errors. This last value is not in agreement with our determination.

We determine N_{DI} using all transitions from Lyδ up to the Lyman limit of D I. Allowing the continuum to very did not have a discernible effect on our determination of N_{DI}. D I is fully blended into H I until ly4 and is saturated up until the ly8 transition. It can still be clearly seen and measured up until ly13 and less clearly to ly14. In total, there were 12 transitions that were of use for the

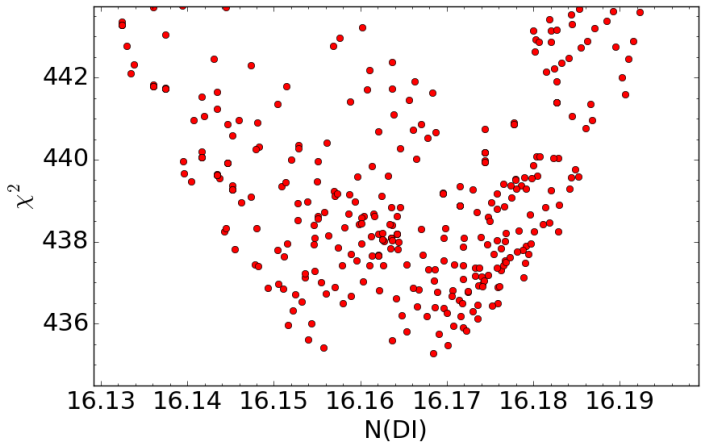

Figure 4.5. χ^2 versus N_{DI} for D I towards J0744+2059. Here we illustrate our usage of our optimization software to determine confidence intervals. We specify initial guess parameters and then, with a parameter of interest locked to some value, optimize all remaining free parameters to find a local minimum of χ^2. For one locked parameter at a time, a 68% confidence interval includes all values of the locked parameter such that $\chi^2 < \chi^2_{min} + 1$ (see Avni (1976)).

determination of N_{DI}.

We find a value of 10^5D/H2.359 $\pm$ 0.095, which is lower than the D/H value derived from the CMB and and Cooke et al. (2014). We report this result as our primary finding in this chapter, but it is important to note that when using only the DLA damping wings to determine N_{HI}, the continuum level is very important. Introducing continuum points to account for inflections at the wavelengths of suspected echelle order flux instabilities, we recover N_{DI} that is 0.12 dex lower, bringing D/H into full consistency with the CMB. However, we do not know the amount by which the flux levels differ here to within the required level of precision and these inflection points may not reflect the best possible continuum. Additionally, and most crucially, Lyman series absorption from Ly$\gamma$to the Lyman limit independently supports a nearly identical match to our estimate of N_{HI} from the DLA damping wings with a smooth continuum, though with larger error.

Table 4.3. Estimated metal abundances for the $z_{\rm abs} = 2.98838$ system towards J0744+2059 with respect to photospheric solar values (Asplund et al., 2009)

Element	[X/H] (solar units)
O	-1.91 ± 0.68
Si	-1.88 ± 0.69
C	-1.96 ± 0.69
Al	-1.86 ± 0.66
Fe	-1.96 ± 0.68

Inferred Gas Properties

Using the determined column-densities of our metal lines, we find a low-ionization system exhibiting 1/100 $Z_{\odot}$. We run a grid of photoionization models with `cloudy` (Ferland et al., 2013), using plane-parallel geometry and a UV background at redshift $z = 2.54$ according to Haardt and Madau (2012). We then simultaneously constrain the grid using purpose built software according to our observed column densities and setting upper limits on the gas temperature using our line widths, b.

We find Z= -1.9 ± 0.4 from the range of Z determined by Al II and O I since their column densities are precisely determined and due to their nearly flat response to the determined range of ionization parameters, U, they set tight constraints on Z. Si III and C III simultaneously constrain ionization parameter to the range $-3.6 >$log U> -3.1, and hydrogen number density to ($-1.8 <$ log $n_H < -1.3$).

Summary

We report D/H towards a new QSO exhibiting a DLA with a single dominant component H I with $N_{\rm HI} = 10^{20.79}$. This is on par with the densest of such systems in QSO absorption literature, with a slightly larger H I column than the system at $z_{\rm abs} = 2.70242$ towards J1558–0031 O'Meara et al. (2006); Cooke et al. (2014).

Our resulting value of D/H is 2.1σ below the CMB (Planck Collaboration, 2015), and 1.7σ below Cooke et al. (2014). Our D I lines were constrained by numerous clear transitions from Lyδ up to the Lyman limit. We measure N_{HI} from both the damping wings of the DLA to high precision, and independently, from Lyman series absortpion from Lyγ to the Lyman limit, both cases with continuum free to vary.

Acknowledgements

This chapter was adapted from work being prepared for publication under the working title *The primordial Deuterium abundance in gas towards QSO J0744+2059*. The author of this dissertation is the primary author and David Tytler is co-author.

The author wishes to recognize and acknowledge the very significant cultural role and reverence that the summit of Mauna Kea has always had within the indigenous Hawaiian community. We are most fortunate to have the opportunity to conduct observations from this mountain.

The data presented herein were obtained at the W.M. Keck Observatory, which is operated as a scientific partnership among the California Institute of Technology, the University of California and the National Aeronautics and Space Administration. The Observatory was made possible by the generous financial support of the W.M. Keck Foundation.

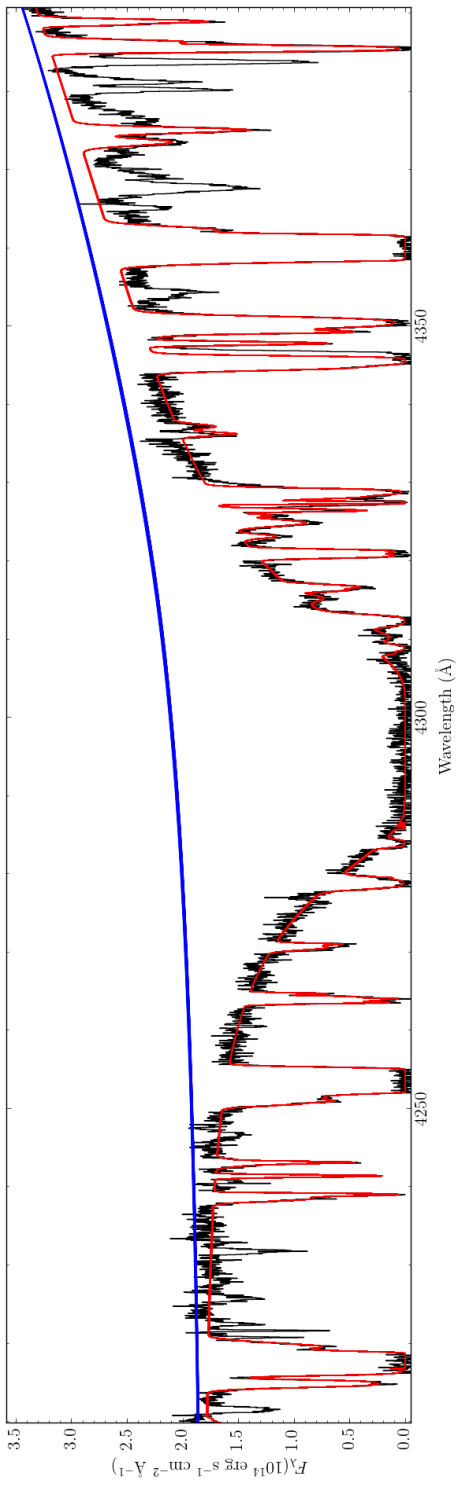

Figure 4.6. The Damped Lyα towards J0744+2059 at $z_{\rm abs} = 2.5338836$. The blue line consists of 387 continua generated by our random continuum generator. Continua were initially specified to vary by up to 3% from the best fit value, but were then free to vary as needed to fit the data as absorption parameters were also varied, after which the surviving continua varied by up to 1.1% around the center of Lyα. This is meant to show all likely best-fit continua. See chapter 2 for a discussion of this continuum generating procedure.

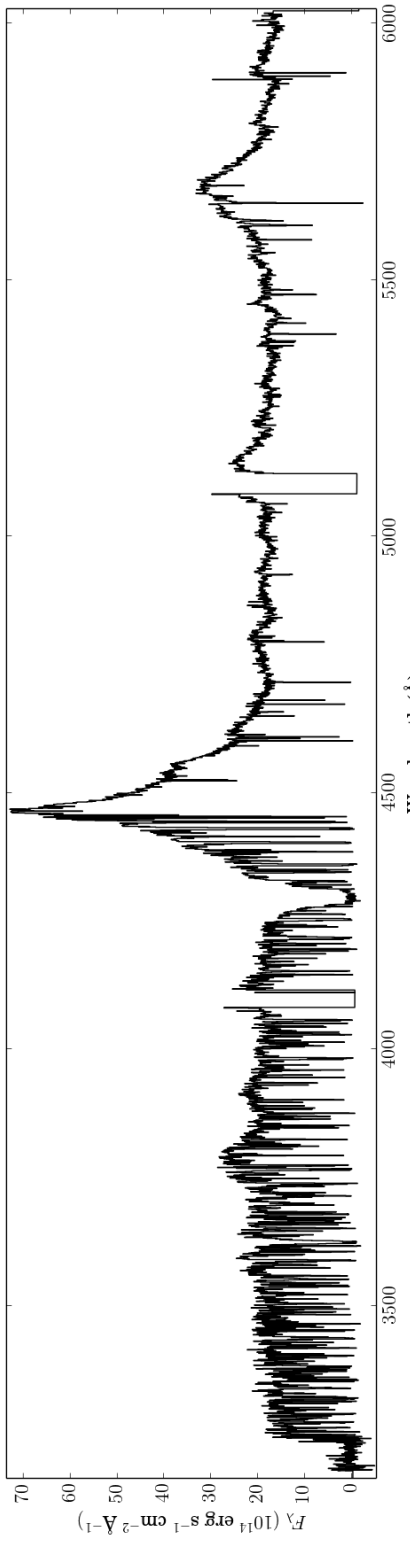

Figure 4.7. The full spectrum of J0744+2059. Here, we rebin the spectrum for for clarity.

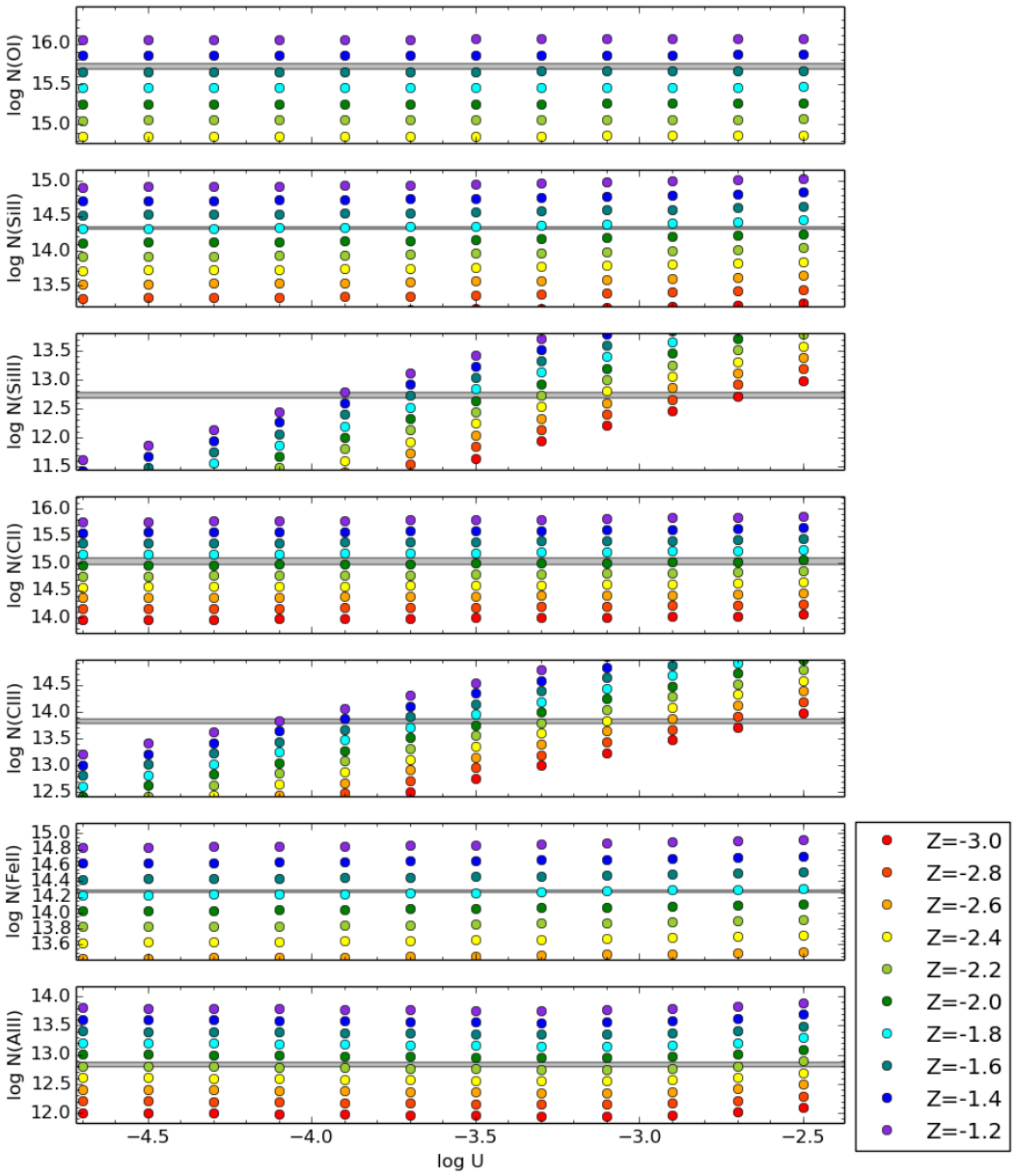

Figure 4.8. Column densities versus ionization parameter, U, for selected metals from the $z_{\rm abs} = 2.98838$ systems towards J0744+2059. The gray bar indicates the observed 1σ limits on column density. These quantities were calculated from running grids of photoionization simulations using `cloudy` (Ferland et al., 2013) and constraining using our observed column densities and observed line widths to set an upper-limit on gas temperature.

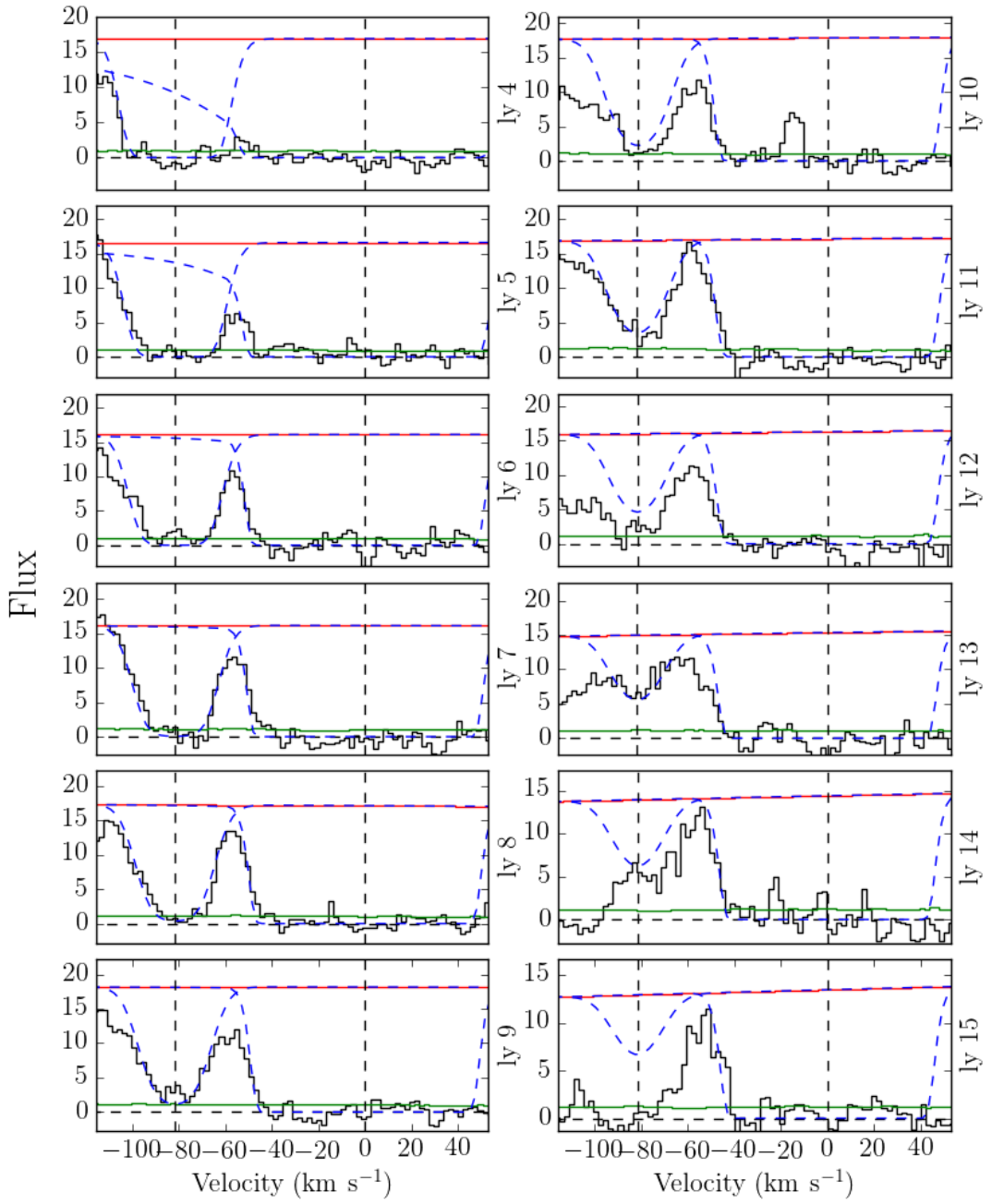

Figure 4.9. The Lyman-series for the $z_{\rm abs} = 2.98838$toward J0744+2059 from Lyδ (denoted ly4) up to ly15. The flux here is in units of 10^{14} ergs s^{-1} cm^{-2}Å^{-1}.

Chapter 5

D/H measurements: Results and Implications

We add two new systems to the current repertoire of published systems exhibiting Deuterium. One of these objects, J0722+2059, is consistent with the requirements of Cooke et al. (2014), but results in a low D/H. J1201+0116, on the other hand, does not fit these criteria, being of small column density $10^{17.4}\mathrm{cm}^{-2}$, and only one transition of D I, but is of significant interest since it has a very high signal-to-noise, and exhibits unusually metal poor. This latter objects yields D/H in full agreement with the the CMB and theory (Planck Collaboration, 2015; Cyburt et al., 2015).

Including estimates from literature, we calculate limits on the effective number of neutrino flavors, N_{eff}, neutrino degeneracy parameter $\xi_\nu = \mu_\nu/k_bT$, which is a measure of the degree of lepton asymmetry, and the baryon density, finding room for new physics, but not for new neutrinos. These estimates depend heavily on the value of the primordial Helium mass fraction, Y_p.

D/H from Literature

We examine values of D/H published in extragalactic literature and explore the effect of including D/H measured from Deuterated molecular Hydrogen towards DLAs as well as the effect of removing outliers. We find that including measurements from molecular hydrogen have an insignificant effect on D/H, but because of potential complications in the chemistry, leave only D/H towards quasars in our estimate of D/H.

Dispersion in D/H

One major concern in D/H literature is the observed spread in values. While destruction of D is expected to be low for Z<10% $Z_{\odot}$ and negligible for Z<1% $Z_{\odot}$ (Prantzos, 1996; Tosi et al., 1998; Matteucci et al., 1999; Romano et al., 2006). Dvorkin et al. (2016) explores this dispersion in light of differing structure formation histories, finding that for z$\sim$ quasars, this dispersion will never be lower than 1/3 of the primordial value and finding a tight correlation between D and metal content. However, in current D/H literature, there is neither a discernable trend in D/H and H I column density, redshift, nor a trend in metal content versus D/H. In fact, the three studies with the highest metal content show high D/H (O'Meara et al., 2006; Burles and Tytler, 1998a; Levshakov et al., 2002). While some of the dispersion may originate from physical conditions of the gas, the dominant source may come from measurement errors, either in methodology or quality of data.

Riemer-Sørensen et al. (2015) reanalyze a system first reported by Crighton et al. (2004), with much higher SNR, in which velocity structure can be more clearly discerned. Their value of D/H was significantly lower than that of Crighton et al. (2004), showing that choice of velocity structure has an important effect on

the estimate of D/H. Furthermore, implementing micro/mesoturbulent models in the fit of D/H as opposed to the typical Voigt-profile may produce a significant difference (Levshakov et al., 1998a,b). Another source of error is contamination by unrelated absorption lines (Kirkman et al., 2003). The study of J1201+0116 in this dissertation found that, especially for small-column systems, contamination needs to be considered. Finally, continuum error is often underestimated or not treated at all, due to the difficulty in accurately estimating it, particularly among absorbers with large regions of absorption, like DLAs, which rely on the the precise determinations of N_{HI} from their damping wings, upwards to 1000 km s^{-1} from the line center. Having regions free of absorption are important in estimating the continuum level (e.g., Cooke et al. (2014); Riemer-Sørensen et al. (2015)) and other authors have used automated procedures to generate continua to estimate the statistical effect (e.g. this dissertation and Kirkman et al. (2003)). Exacerbating the difficulty of continuum estimation is the flux calibration, which is particularly problematic for the high-resolution echelle spectrographs needed to do D work. This problem is particularly pronounced for DLAs, where the flux upwards of 1000 km s^{-1} red and blue of the line center along the damping wing is used to tightly constrain the Hydrogen column density. With this wide array of errors, it is likely that the main component of this dispersion in D/H is due to measurement errors or systematic effects.

Including Molecular HD/2H_2

As of August 2016, there are 3 published systems used for measuring extragalactic HD/2H_2 (Klimenko et al., 2015; Noterdaeme et al., 2008; Ivanchik et al., 2010; Varshalovich et al., 2001). Incorporating these studies has little effect on our mean. While still too small of a sample size to speak definitively, two of

these studies reports a high value of D/H. One of these (Klimenko et al., 2015), reports errors about half the size of similar studies, putting its mean 3.6σ from the CMB result. Tumlinson et al. (2010) however questions whether the chemistry has an effect on the value of D/H estimated from this method. As such, we are careful to treat this method independently from measuring neutral atomic H and D, and include the combined results with a note of caution.

Incorporating these studies does neither affects the weighted nor unweighted means, though they do increase the dispersion a bit for the unweighted calculation.

Selection Criteria

The selection criteria suggested by Cooke et al. (2014) was able to produce a small error on D/H at the cost of only including a handful of viable QSOs absorption systems. The idea was to introduce systematized quality control into the data, which would ensure the most precise measurement. Since this has been introduced, Balashev et al. (2016) introduced an object fully passing these criteria, but exhibiting low D/H, questioning the usefulness of the selection criteria. Riemer-Sørensen et al. (2015) introduced another system which did not pass the criteria, but nonetheless produced D/H in good agreement with commonly accepted values.

This dissertation reports on two new objects. J0744+2059 has a large column with Lorentzian damping wings allowing for a very precise determination of column density. It also has many metal lines and clear transitions of D, yet it produces a low D/H: 2σ below widely accepted values. J1201+0116 has one of the smallest column densities and only one transition of D, which disqualifies it, however it exhibits high SNR, clear unblended Lyman-series absorption with a clear Lyman-limit, and is very metal poor, meaning it is likely primordial gas.

Of particular note are the H I column density requirements that N(H I)$\geq$

10^{19}cm^{-2}. While Lorentzian damping wings may allow for precise determination of column density, they are more susceptible to flux calibration errors, which are ubiquitous among echelle spectrographs providing the resolution needed for D/H work, which in turn lead to significant continuum errors. They are susceptible by virtue of their width: a typical DLA can have damping wings thousands of km s^{-1} wide over a device that may have fluxing problems over the scale of hundreds of km s^{-1}. Conversely, lower column density systems do not exhibit these extended wings is determining continuum level is much easier, and typically more accurate[1]. In short, we argue for a more holistic approach when looking at D/H literature.

Mean D/H

A simple mean of all studies together gives $10^5 D/H = 2.533$ with a standard deviation $\sigma = 0.641$, and $\chi^2/df = 6.62$; the mean is then a poor fit to the data.

In addition to this, we calculate weighted and unweighted means with and without clipping criteria (see Table 5.1). To account for remeasurements of the same system while bootstrapping, we randomly select the results of one study for each reported system per iteration. It should be noted, however, that two of the remeasurement studies are inconsistent with the original works showing that indeed, the discrepancy is more than statistical error (Burles and Tytler, 1998a; Cooke et al., 2011, 2014; Crighton et al., 2004; O'Meara et al., 2006; Pettini et al., 2008a,b; Riemer-Sørensen et al., 2015).

We then apply our statistic on the sample and append to the bootstrap distribution we used to estimate confidence intervals. We create a sampling distribution with $n = 1500$ and find that removing outliers which are more than 2σ

[1]While the same flux calibration issues will exist for smaller column density systems, D/H measurements rely on relative flux, not absolute flux, the the measurement can still be done with accuracy.

Table 5.1. The mean of D/H from measurements in literature. Each element of each column below shows a different calculation of the mean and 68% confidence intervals calculated using bootstrap methods. The first column indicated the clipping method, if any: 2σ corresponds to 2σ clipping during each resampling of the bootstrap and 2MAD similarly indicates clipping items more than 2 mean absolute deviations (MAD) from the mean during each iteration. To account for replication studies on the same system, we randomly select one of each study for each system, to prevent over-representation of one system over another. This is performed prior to each resampling.

clipping	unweighted D/H	weighted D/H
-	$2.537^{+0.175}_{-0.172}$	$2.516^{+0.045}_{-0.044}$
2σ	$2.473^{+0.143}_{-0.141}$	$2.502^{+0.037}_{-0.039}$
2MAD	2.500 ± 0.173	$2.507^{+0.046}_{-0.045}$

from the mean or more than 2 MAD (mean absolute deviations) from the mean creates virtually no difference in our sampling distribution compared to no outlier rejection. Calculating a weighted mean from our bootstrap distribution, selecting randomly from re-measured studies, we find 10^5D/H$= 2.50 \pm 0.04$ (68%CI) when clipping studies more than 2σ from the mean and clipping those more than 2 mean absolute deviations, we see 10^5D/H$= 2.51 \pm 0.05$. Of course these weighted means should be taken with a grain of salt because some studies may include poor data or measurements.

Including selected measurements due to quality of data (Burles and Tytler, 1998a,b; O'Meara et al., 2001; Kirkman et al., 2003; Fumagalli et al., 2011; Cooke et al., 2014; Riemer-Sørensen et al., 2015; Balashev et al., 2016) with our studies of D toward J1201+0116 and J0744+2059, we find estimates of mean D/H (see Table 5.1). From these studies, we find an unweighted, unclipped mean yields high D/H, while everything else (clipped and unclipped, weighted and unweighted) appears consistent with each other. This gives χ^2/df=2.21.

Table 5.2. Published values of D/H from Deuterated Molecular Hydrogen detected in DLAs towards high-redshift QSOs.

QSO	log HD/2H_2	z_{abs}	reference
J2123–0050	-4.37 ± 0.06	2.059	Klimenko et al. (2015)
SDSS J143912.04+111740.5	$-4.82^{+0.17}_{-0.12}$	2.418	Noterdaeme et al. (2008)
Q1232+082	$-4.44^{+0.23}_{-0.13}$	2.3377	Ivanchik et al. (2010)

Table 5.3. The Deterium-Hydrogen ratio (D I/H I) measured towards QSOs in literature.

QSO	log (D/H)	$z_{\rm em}$	$z_{\rm abs}$	[X/H]	X	log $N_{\rm HI}(cm^{-2})$	reference
J1201+0116	-4.602 ± 0.031	3.231	2.98838	< -3.2	O	17.403 ± 0.006	this work
J0744+2059	-4.639 ± 0.015	2.67	2.5338836	-1.9	O	20.790 ± 0.004	this work
HS0105+1619	-4.6 ± 0.04	2.640	2.53600	-1.73	O	19.422 ± 0.009	O'Meara et al. (2001)
HS0105+1619	-4.589 ± 0.026	2.652	2.53651	-1.77	O	19.426 ± 0.006	Cooke et al. (2014)
Q0347–3819	-4.426 ± 0.029	3.23	3.025	0.98[a]	Zn	20.626 ± 0.005	Levshakov et al. (2002)
J0407–4410	$-4.55^{+0.12}_{-0.09}$	3.02	2.621	-1.99	O	20.45 ± 0.10	Noterdaeme et al. (2012)
Q0913+072	-4.56 ± 0.04	2.785	2.61843	-2.40	O	20.34 ± 0.04	Pettini et al. (2008b), Pettini et al. (2008a)
Q0913+072	-4.597 ± 0.018	2.785	2.61843	-2.40	O	20.312 ± 0.008	Cooke et al. (2014)
Q1009+2956	$-4.40^{+0.06}_{-0.08}$	2.640	2.50357	-2.5	Si	17.39 ± 0.06	Burles and Tytler (1998b)
J1134+5742	-4.69 ± 0.13	3.522	3.41088	-4.2	Si	17.95 ± 0.05	Fumagalli et al. (2011)
Q1243+307	-4.62 ± 0.05	2.558	2.52566	-2.79	O	19.73 ± 0.04	Kirkman et al. (2003)
J1337+3152	-4.93 ± 0.15	3.17447	3.16768	-2.68	Si	20.41 ± 0.15	Srianand et al. (2010)
J1358+6522	-4.588 ± 0.012	3.173	3.06726	-2.33	O	20.495 ± 0.008	Cooke et al. (2014)
J1419+0829	-4.596 ± 0.009	3.030	3.04984	-1.92	O	20.391 ± 0.008	Pettini et al. (2008a) Cooke et al. (2011)
J1419+0829	-4.601 ± 0.009	3.030	3.04973	-1.92	O	20.495 ± 0.008	Cooke et al. (2014)
J1444+2919	-4.706 ± 0.067	2.66	2.437	-2.04	O	19.983 ± 0.010	Balashev et al. (2016)
SDSS 1558–0031	-4.48 ± 0.06	2.823	2.70262	-1.49	O	20.67 ± 0.05	O'Meara et al. (2006)
SDSS 1558–0031	-4.619 ± 0.026	2.823	2.70242	-1.55	O	20.75 ± 0.03	Cooke et al. (2014)
PKS 1937–101	$-4.8^{+0.07}_{-0.08}$	3.787	3.25601	-2.0	Si	18.25 ± 0.02	Crighton et al. (2004)
PKS 1937–101	-4.61 ± 0.05	3.787	3.256	-1.87	O	18.10 ± 0.08	Riemer-Sørensen et al. (2015)
PKS 1937–101	-4.48 ± 0.04	3.787	3.57220	< -0.9	O	17.86 ± 0.02	Burles and Tytler (1998a)
Q2206–199	-4.78 ± 0.09	2.559	2.07624	-2.05[b]	O	20.43 ± 0.04	Pettini and Bowen (2001)

[a] measured by Ledoux et al. (2003).
[b] measured by Pettini et al. (2008b).

Cosmology

While the dispersion in D/H remains at large, there exist other issues in setting astrophysical constraints on BBN. Independent of the determination by CMB studies, current astrophysical estimates of the Helium mass fraction, Y_p, disagree enough to produce tension in BBN (see Figure 5.3). Additionally, measurements of primordial Lithium are still in conflict with theory (Fields, 2011; Cyburt et al., 2015). For BBN constraints from Deuterium, a big source of uncertainty comes from the experimental errors on nuclear reaction rates (Nollett and Holder, 2011; Coc et al., 2015; Cyburt et al., 2016).

Assuming standard BBN and using Planck's inferred Y_p: ($N_{eff} = 3.046$, $\xi_\nu = 0$), we recover $\eta_{10} = 6.12 \pm 0.33$ and $\Omega_b h^2 = 0.0219 \pm 0.0012$. If we set $\xi_\nu = 0$, use Planck's Y_p, but allow for deviation from the standard N_{eff} get $N_{eff} - 3.046 = -0.087 \pm 0.062$, which, while not admitting another species of neutrino, does imply some change to the deviation from the standard $N_{eff=3.046}$, where this 0.046 is a correction to account for the fact that neutrino decoupling is not instantaneous, and so takes part in some of the energy released during $e^{\pm}$ annihilation (Mangano et al., 2005).

Our calculations follow Steigman (2012), who extrapolates a set of linearized equations from BBN codes, valid for expansion rate deviations in the range$0.85 < S < 1.15$ and baryon-to-photon ratio in the range $5.5 < 10^{10}\eta_b < 6.5$. These equations are reproduced in Equations 16 and 17.

Our calculations leave room for new physics, but no new neutrinos. There is room for a small deviation of N_{eff} from the SBBN value of 3.046 (Mangano et al., 2005), and some deviation of the neutrino degeneracy parameter, ξ_ν, however this depends heavily on the choice of primordial Helium mass fraction, Y_p, which has

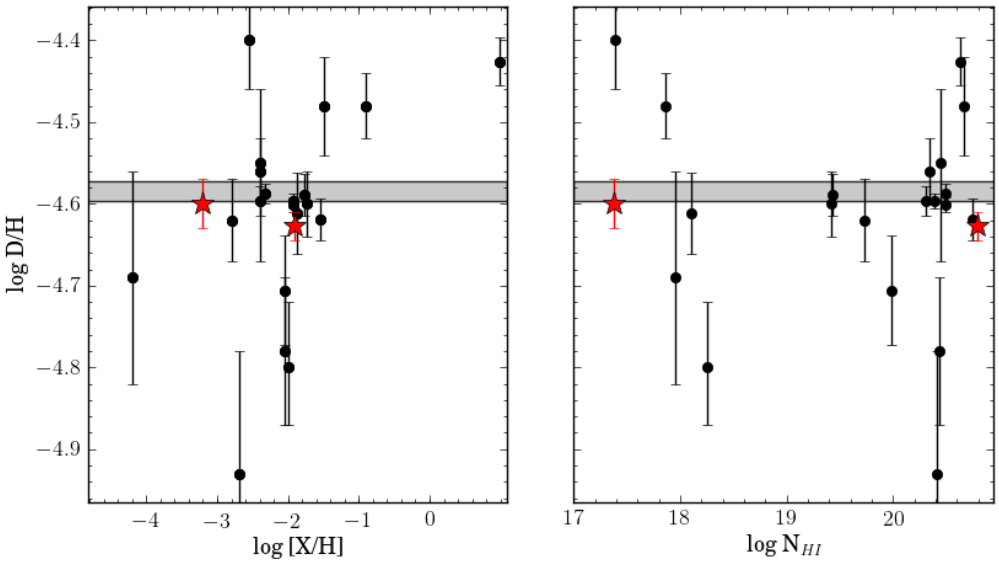

Figure 5.1. Here we show D/H for all QSOs exhibiting Neutral Deuterium versus N(H I) and relative metal abundance [X/H], where X refers to a selected metal, typically O or Si. The dispersion between studies is very clear. The red points indicate the two systems reported in this dissertation.

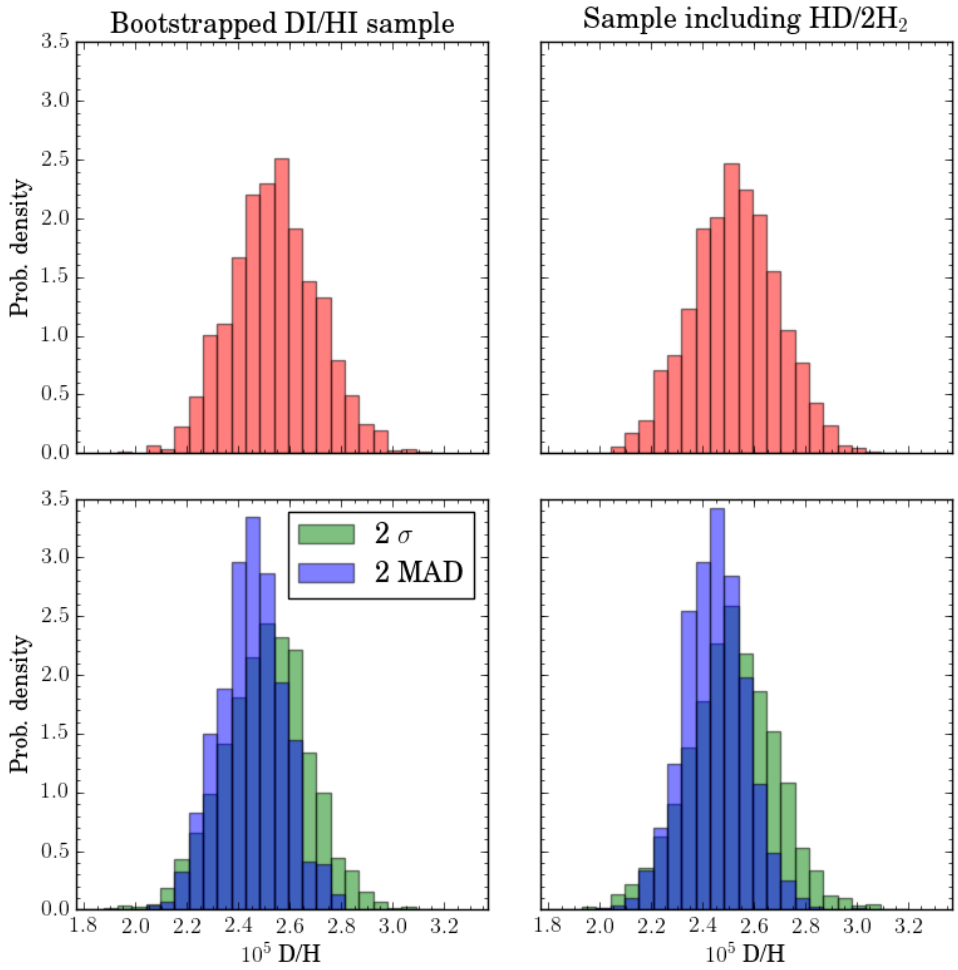

Figure 5.2. Bootstrapped samples ($n = 1500$) of D/H in literature. Since there are so few objects reporting D/H from molecular hydrogen (3 as of July 2016), their effect on the bootstrap sample is minimal. For cases where there is more than one study published on a specific system, we randomly select from published values during each sampling.

Table 5.4. Cosmological parameters estimated from different measurements of Y_p and using the unclipped, unweighted D/H from Table 5.1. Errors are reported as 1σ.

quantity	Planck	Y_p estimated from Izotov et al. (2014)	Aver et al. (2015)
η_b	6.11 ± 0.32	6.15 ± 0.34	6.10 ± 0.33
ξ_ν	0.005 ± 0.011	-0.031 ± 0.015	0.012 ± 0.014
$N_{eff} - 3.046$	-0.087 ± 0.062	0.53 ± 0.18	-0.21 ± 0.15

shows a significant tension (See Table 5.4 and figure 5.3). Using Y_p inferred from Planck or Aver et al. (2015), there is a slight preference for a small, but positive ξ_ν, though just beyond 1σ significance when assuming a $N_{eff} = 3.046$. Conversely, Izotov et al. (2014) seems to suggest a negative ξ_ν for the same N_{eff}.

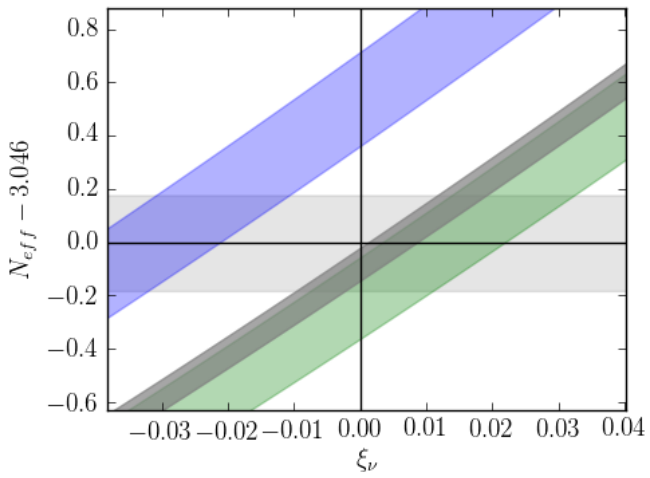

Figure 5.3. Limits on N_{eff} versus ξ_ν using 10^5D/H=2.52 ± 0.21 from Table 5.1. Here we adopt $Y_p = 0.24668 \pm 0.00062$ (2σ) from *Planck TT,TE,EE+lowP+BAO* (dark grey), Izotov et al. (2014) (blue) and Aver et al. (2015) (green). The light-grey horizontal bar indicates limits imposed by the value for N_{eff} from *Planck TT,TE,EE+lowP+BAO*. $N_{eff} = 3.046$ is the value we expect if there are no additional neutrinos and a $\xi_\nu = 0$ means there is no lepton asymmetry, so a non-zero value on either axis implies new physics.

Chapter 6

Statistics of the Lyman-α Forest Towards 25 QSOs

The low-density intergalactic medium (IGM) acts as a cosmic record keeper. Since the adiabatic cooling timescale is long (Hui and Gnedin, 1997), the thermal impact of important cosmological events leave their mark for a long time in diffuse gas before it disperses. This can be probed by observing the absorption of neutral gas towards quasars, where the quasars act as a back light. Using high-resolution optical spectroscopy, we can directly observe absorption of the Lyα forest the numerous collection of low-column density ($N_{HI} \simeq 10^{12-14}$) neutral hydrogen $n = 2 \rightarrow 1$ absorption lines. Taking statistics on an ensemble of these lines allows us to glean an understanding of the bulk evolution of the universe. Such statistics set contraints on simulation, which is required for understanding the physical implications of observations. This chapter reports on new statistics of the Lyα forest .

Shortly after recombination at $z = 1090$, the universe is entirely cold neutral gas and thus begins the cosmic *dark ages*. Gravitation causes gas to clump together, eventually forming the first stars and galaxies. Subsequently, heating thought to be driven predominantly by pop II stars, ionized all of the H I and He I gas in the universe with Lyα forest measurements suggesting this is complete by $z \approx 6$

(Fan et al., 2006; McGreer et al., 2015). This is called Hydrogen *reionization*. By redshift $z \approx 3$, It is thought that quasar photoheating has fully ionized all of the He II gas (McQuinn et al., 2009; Shull et al., 2010; Worseck et al., 2011). All the meanwhile, the expansion of the universe causes most of this intergalactic gas to become increasingly less dense with time, with much of this gas being incorporated into overdense filamentary structures.

Tytler et al. (2009) presented an analysis of simulated spectra of the Lyα forest , noting that (1) the simulated spectra produced lines that were too wide, (2) had too many small (log N(H I)<14 cm^{-2}) lines and too few larger lines, (3) yielded a power spectrum with too low of amplitude. The argument was that the data is correct, but its the simulations that were lacking.

We report on the results of a study of absorption systems towards 25 QSOs, encompassing absorbers from $z_{\rm H\,I} = 1.8 - 4.6$. The goal of this chapter is to report on data and present an analysis to set further constraints for use with simulation. We will not do an exhaustive comparison to literature, but we will compare a few key parameters. In section 6.2.1, we present a Voigt-profile analysis of the temperature density relation from over this redshift range and the proceed to discuss our distribution of line widths. In section 6.3 we report on our column-density distribution and in section 6.4 we report on the Lyα forest optical depth. Where relevant, we assume a ΛCDM cosmology assuming a flat universe with $H_0 = 70$ km s^{-1}, $\Omega_m = 0.27$, and $\Omega_\Lambda = 0.73$.

Data

Kirkman et al. (2005) reports on the Opacity of the IGM towards 25 QSOs. This paper calculated the amount of absorption, D_A, statistically removing metal lines. We use very nearly the same data, with a one more high-redshift QSO. (See

Table 6.1) with the same continua reported there. We fit each absorption system that could be identified between 2009 and 2010 using the fits of three undergraduate researchers, BO, JL and SG (the author), who had received dedicated training on fitting QSO absorption lines using known spectra. Their fits were assisted by the use of optimization software to determine a best fit (see chapter 2). The students were instructed to fit metals and any suspected metal they flagged as such. Anything fit as an H I absorber with $b < 10$km s^{-1} was automatically flagged as a metal.

Analysis of the data was then performed later by the Author in 2016. In total, this data-set includes 9448 H I absorbers and 2356 positively identified metal absorbers. For a discussion of continuum error, see Kirkman et al. (2005).

For our analysis of the Lyα forest , we only consider spectra in the range 1070-1170Å, with respect to the Lyα emission of the quasar. We start at 1070 Å to ensure we are not including any Lyβ lines and we end at 1170Å, as opposed to 1216Å to ensure that none of our absorption systems are spatially close enough to be effected by quasar emission.

Measurements

b-N distribution

As energy enters into a system through photoheating, this heating competes with adiabatic cooling caused by continued expansion. Underdense regions are less gravitationally bound than overdense regions and so are expected to experience more rapid cooling, while overdense regions experience less expansion, but also have faster recombination time-scales, yielding a greater photoionization cross-section and thus more heating, so temperature should directly trace density. At its simplest,

Table 6.1. Our 25 QSO sample used for our study of the Lyα forest .

coordinates (B1950)	V	z_{em}	wavelength range (Å)
07:47:25.62+42:59:58.5	15.80	1.900	3053.19 —4546.53
07:57:29.24+52:18:52.7	17.50	3.240	3575.37 —5128.10
11:07:48.10+48:47:33.0	16.70	2.960	3725.95 —6189.69
06:36:47.61+68:01:27.3	16.46	3.180	3539.09 —5055.09
01:19:16.21+14:32:43.2	16.70	2.870	3200.55 —4718.59
01:00:33.38+13:00:12.1	16.57	2.681	3392.58 —4913.15
04:49:59.00−16:45:9.0	17.00	2.677	3574.87 —5127.42
10:17:30.85+10:55:8.1	18.40	3.152	3893.78 —6293.79
03:22:11.18−32:13:34.6	17.95	3.302	3831.90 —5355.65
10:05:44.13+36:38:2.4	17.85	3.125	3536.07 —5057.47
13:37:47.92+21:23:54.1	17.90	2.700	3272.42 —4783.79
15:17:8.11+23:56:52.0	16.40	1.898	3121.13 —4629.90
15:00:58.81+04:31:30.7	19.30	3.670	4610.03 —7057.52
00:14:4.45+81:18:28.6	16.50	3.366	4000.03 —5360.90
20:38:16.60−01:16:21.0	19.10	2.783	3338.94 —6184.40
19:46:41.00+76:58:26.0	15.85	2.994	3469.94 —6299.17
07:41:42.05+47:41:53.4	17.50	3.210	3574.75 —7472.83
12:43:44.90+30:47:54.0	17.00	2.560	3159.87 —5883.36
01:05:26.97+16:19:50.1	16.90	2.640	3188.78 —6639.47
01:30:50.28−40:21:51.0	17.02	3.023	3419.51 —4916.07
16:45:54.03+55:20:1.1	18.10	4.037	4540.89 —6063.86
11:22:12.28−16:48:47.4	16.50	2.400	3179.61 —4721.77
12:02:49.20−07:25:50.8	18.70	4.694	4978.07 —7304.37
13:37:46.22+28:32:3.4	17.10	2.517	3179.68 —4721.87
03:24:28.59−40:47:16.3	17.60	3.056	3611.90 —6084.84

the $T - \rho$ relation is typically modeled to follow a power-law:

$$T = T_0 \left(\frac{\rho}{\bar{\rho}} \right)^{\gamma - 1} . \tag{6.1}$$

where we have mean IGM density $\bar{\rho}$ and respective characteristic temperature T_0 with power-law index γ (Hui and Gnedin, 1997; Schaye et al., 1999).

This relation has been measured many times using QSO spectroscopy of the Lyα forest , and among these measurements, there has been significant disagreement. A handful of studies using different methods found a significantly *inverted* $T - \rho$ relation, one where increased density leads to a cooler temperature ($\gamma < 1$), (Becker et al., 2007; Viel et al., 2009; Bolton et al., 2008; Calura et al., 2012; Lidz et al., 2010; Garzilli et al., 2012), while others have found the converse ($\gamma > 1$) (Schaye et al., 2000; Ricotti et al., 2000; Bryan and Machacek, 2000; McDonald et al., 2001; Rudie et al., 2012).

It is thought that the well known cutoff in b-N distribution of low-N QSO absorption lines is one manifestation of this $T - \rho$ relation and so finding a cutoff function has been a subject of significant study (Schaye et al., 1999; Rudie et al., 2012; Bolton et al., 2014). Since temperature is not directly measured, studies using Voigt profile analysis use the lower envelope of the b-N distribution to set a minimum temperature:

$$\frac{b_{min}}{b_0} = \left(\frac{N_{\mathrm{H\,I}}}{N_{\mathrm{H\,I},0}} \right)^{\Gamma - 1} . \tag{6.2}$$

Γ here is another power law index related, but different from γ, b_0 and N_0 are characteristic b and N and b_{min}. In order to connect this to temperature and density, it is necessary to run simulations (Schaye et al., 1999; Rudie et al., 2012; Bolton et al., 2014). We attempt to measure a cutoff function for the log

Table 6.2. Results of b_{min} absorbers for H I absorbers. Here we use the power-law clipping algorithm described in Schaye et al. (1999) $\gamma - 1$ is the power-law index for the temperature density relationship (equation 6.1), in which for simplicity, we follow the assumption of Rudie et al. (2012), that $\gamma - 1 = 3(\Gamma - 1)$.

$z_{\rm H\,I}$ range	$\langle z_{\rm H\,I} \rangle$	total absorbers	b_0 (km s^{-1})	T_0 (K)	$\Gamma - 1$	$\gamma - 1$
$1.8 \leq z_{\rm H\,I} < 2.2$	2.103	268	16.743 ± 0.416	16900 ± 800	0.047 ± 0.017	0.142 ± 0.051
$2.2 \leq z_{\rm H\,I} < 2.6$	2.437	1799	11.820 ± 0.158	8400 ± 200	0.007 ± 0.012	0.022 ± 0.036
$2.6 \leq z_{\rm H\,I} < 3.0$	2.788	2074	12.195 ± 0.309	9000 ± 500	0.003 ± 0.024	0.010 ± 0.073
$3.0 \leq z_{\rm H\,I} < 3.4$	3.150	955	17.324 ± 0.389	18000 ± 800	0.109 ± 0.018	0.327 ± 0.054
$3.4 \leq z_{\rm H\,I} < 3.8$	3.594	348	13.694 ± 0.362	11300 ± 600	-0.019 ± 0.023	-0.058 ± 0.070
$3.8 \leq z_{\rm H\,I} < 4.2$	3.940	249	17.464 ± 0.528	18400 ± 1100	0.102 ± 0.025	0.309 ± 0.075

N=12.5-14.5 Lyα forest and use the approximation $\gamma - 1 \approx 3(\Gamma - 1)$ to relate to temperature and density using findings from Rudie et al. (2012).

We measured the b-value lower cutoff in or b-N distributions using an iterative power-law clipping algorithm described in Schaye et al. (1999). For $N(\mathrm{H\,I}) = 10^{12.5-14.5}\mathrm{cm}^{-2}$, it is thought that most absorbers are dominated by the thermal contribution to b (Bryan and Machacek, 2000), so we restrict our sample to this range. Additionally, to avoid poor identifications, we only consider lines with SNR>20.

We chose $N_{\rm H\,I,0}$ to be the median of our sample, $10^{13.33}\mathrm{cm}^{-2}$, though the choice is arbitrary. (Schaye et al., 1999) compare thermal models to data finding that the power-law indices for equations 6.2 and 6.1 are related by $3(\Gamma - 1) \approx \gamma - 1$. We find much scatter among the points using an iterative power-law clipping so it is difficult to draw firm conclusions, however the points tend to scatter slightly above zero (Figure 6.3). This may indicate an isothermal, or nearly isothermal ($\gamma = 1$) relation. Furthermore, we see no convincing signs of redshift evolution of this parameter.

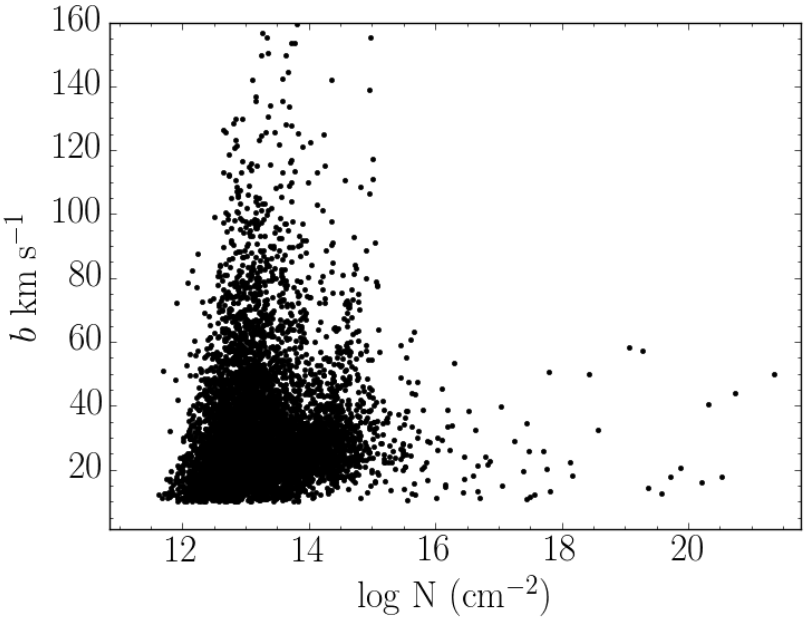

Figure 6.1. b versus N over all z for SNR> 20.

Line Width Measurements: b_σ

We fit line widths of our data in bins of redshift (Fig. 6.6) and column density (Fig. 6.5) bins as a Hui-Rutledge distribution characterized by the characteristic line width parameter, b_σ (Hui and Rutledge, 1999). We find b-values that are consistently smaller than those of other studies (Kim et al., 2002; Lu et al., 1996). We find that it b_σ peaks at redshift $z = 3$, which may indicate a temperature peak at He II reionization. This is consistent with analysis by Upton Sanderbeck et al. (2016) and with Lyα forest measurements at moderate redshifts (Schaye et al., 2000; Lidz et al., 2010; Becker et al., 2011; Garzilli et al., 2012; Bolton et al., 2014; Boera et al., 2014). We summarize our b_σ measurements in Table 6.3, also separating by SNR.

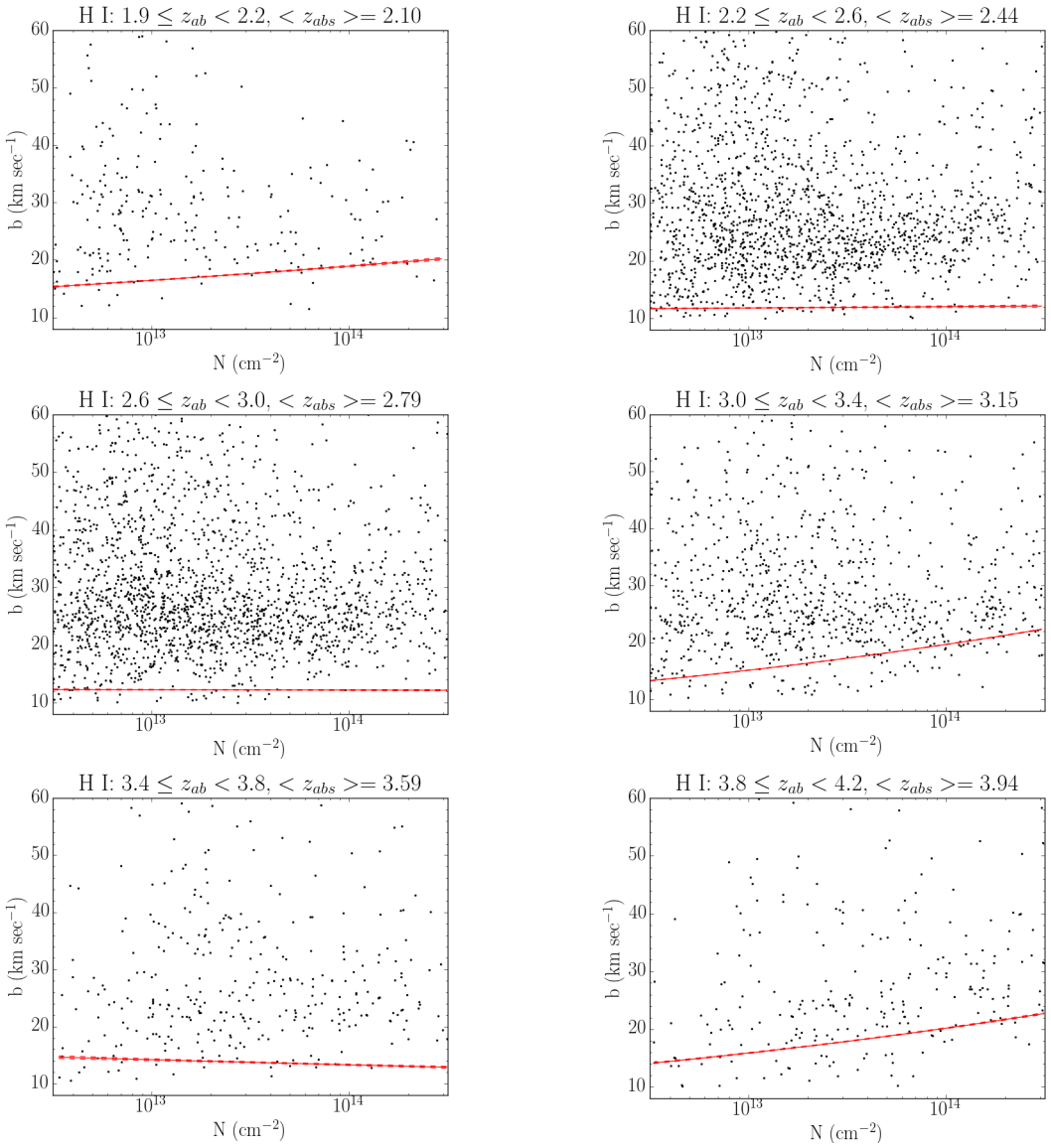

Figure 6.2. *b*-N distributions and our estimate of the *b*-N minimum cutoff using the the methods described in Schaye et al. (1999).

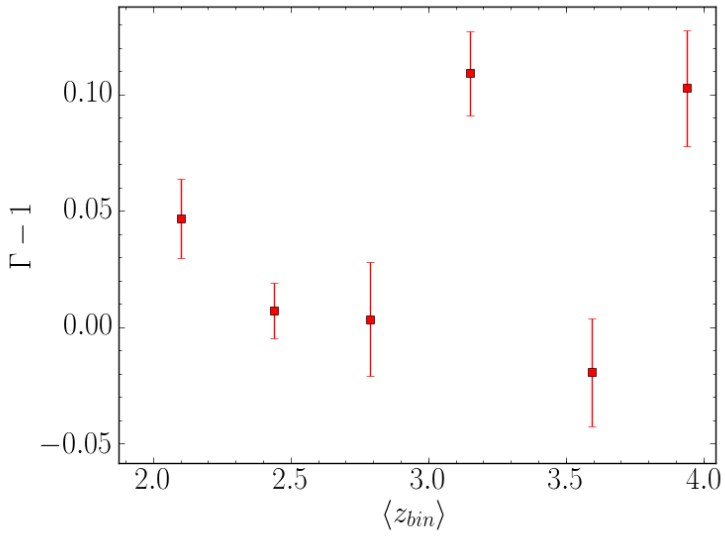

Figure 6.3. $\Gamma - 1$ versus redshift for H I absorbers in our sample.$\Gamma - 1$ is the power law index for fitting equation 6.2, where b_{min} is the minimum line width at any column density in a b-N distribution. We report $\Gamma - 1$ as opposed to γ because $\Gamma - 1$ does not require comparison to models. We perform this calculation using the power law clipping method introduced by Schaye et al. (1999). The points tend to scatter slightly above zero, so if this is any indicator of the $T - \rho$ relation, then it may suggest a nearly isothermal relation with no redshift evolution.

Table 6.3. Here we present our estimates of b_σ and the number of absorbers for bins of SNR and absorber redshift, z_{ab}. Errors are estimated using maximum-likelihood methods corresponding to 68 % confidence intervals to the fit. Bins where b_σ could not be fit were left blank.

	b_σ (km s^{-1}) and number of lines in given bin											
z_{ab} \ SNR, n	0-10		10-20		20-40		40-80		80-160		>160	
1.6−2.0	46	-	110	23.26 ± 29.73	26	-	0	-	0	-	0	-
2.0−2.4	6	-	638	21.73 ± 5.14	547	21.24 ± 7.49	523	21.86 ± 6.91	23	-	0	-
2.4−2.8	91	-	522	22.91 ± 4.31	1170	22.69 ± 2.33	1079	23.43 ± 4.52	432	22.33 ± 17.19	14	-
2.8−3.2	122	18.34 ± 27.77	642	21.58 ± 6.72	668	23.62 ± 7.67	749	23.06 ± 6.80	459	23.97 ± 10.84	31	-
3.2−3.6	1	-	221	-	417	21.06 ± 5.96	122	21.07 ± 23.17	14	-	0	-
3.6−4.0	3	-	21	-	391	20.96 ± 10.31	15	-	0	-	0	-
4.0−4.4	0	-	6	-	162	15.60 ± 13.05	7	-	0	-	0	-
4.4−4.8	0	-	0	-	106	15.89 ± 24.39	54	15.54 ± 28.19	8	-	0	-

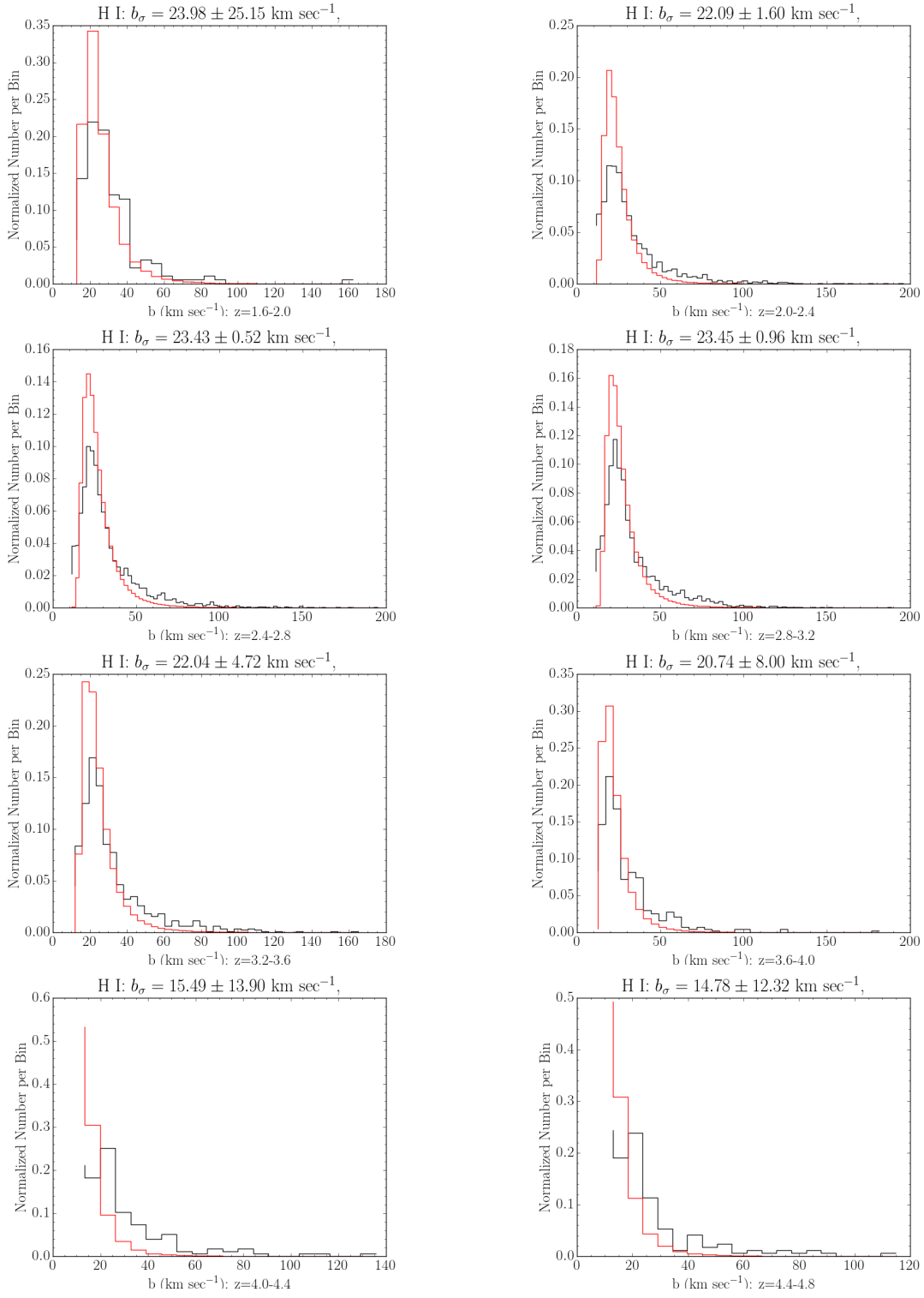

Figure 6.4. b_σ distribution functions for eight redshift bins ranging from $z = 1.6 - 4.8$. These fits include all SNR. For b_σ incorporating SNR cutoffs, see Table 6.3. The reported errors are 68% confidence intervals. The large errors on redshift bins beginning with 1.6, 4 and 4.4 are due to a paucity of data in these ranges, preventing an adequate fit, however we include them for completeness.

Table 6.4. Best fits to the H I column density distribution per absorption distance. This statistic is calculated as Equation 6.3 The fitting function used is of the form found in Equation 6.5.

	$10^{13.3} < N_{\rm H\,I} < 10^{16}$ cm^{-2}		$10^{17} < N_{\rm H\,I} < 10^{19.5}$ cm^{-2}	
redshift	β	log A cm^{-2}	β	log A cm^{-2}
2-2.4	-1.727 ± 0.062	13.56 ± 0.86	-1.04 ± 0.30	2.2 ± 5.3
2.4-2.8	-1.741 ± 0.049	14.02 ± 0.68	-0.98 ± 0.20	1.2 ± 3.6
2.8-3.2	-1.719 ± 0.049	13.64 ± 0.68	-1.04 ± 1.31	2.1 ± 24.1
3.2-3.6	-1.621 ± 0.077	11.84 ± 1.07	-0.49 ± 0.73	-7.6 ± 12.9
3.6-4	-1.602 ± 0.078	11.31 ± 1.10	-0.76 ± 1.78	-3.0 ± 32.0

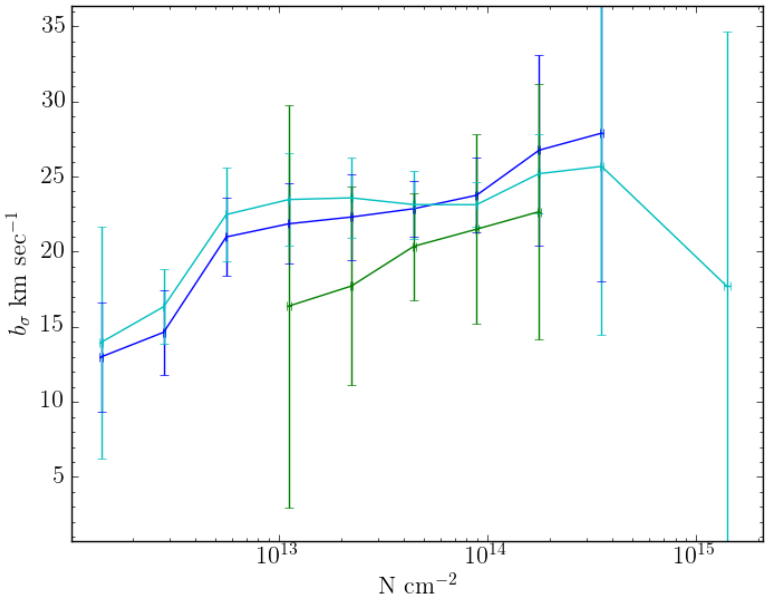

Figure 6.5. b_σ versus log N for all H I absorbers with different z cutoffs. The blue, cyan and green points are: $1.6 < z < 2.6$, $2.6 < z < 3.6$ and $3.6 < z < 4.6$ respectively. Errorbars are one standard deviation. We find broadly that b_σ goes up with N, similar to the b-N distribution lower-envelope, and that there is no discernible difference between $1.6 < z < 2.6$ and $2.6 < z < 3.6$, however the highest redshift bin is shifted down a bit.

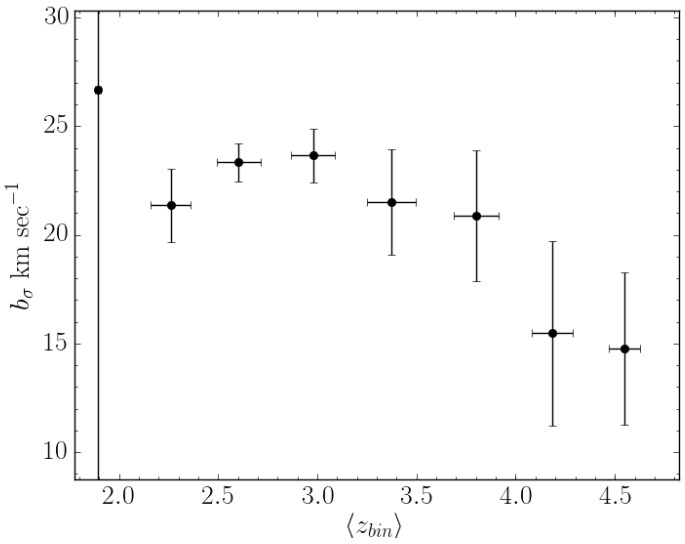

Figure 6.6. b_σ for H I absorbers in our sample versus redshift. b_σ was calculated by fitting a Hui-Rutledge distribution to our b-values over redshifts binned from $z_{abs} = 1.6 - 4$. The errors on b_σ come from a covariance matrix estimate of the error from python's `scipy.optimize.curve_fit` function and the errors on z_{abs} are a simple standard deviation of redshifts the set of absorbers within that bin centered on the mean.

HI Column Density Distribution

The H I column density distribution is a useful tool describing the distribution of gas in the IGM. Here we report the incidence of absorbers with respect to column density, line width, and redshift. Higher column-density systems correspond to denser gas, which tends to also lie closer to a galaxy, and thus experience to effects of galactic physics, whereas lower column density gas will be more diffuse.

We measure the frequency distribution of, f, of H I absorbers per unit absorption distance, dX which is defined as

$$f = \frac{\partial^2 N}{\partial X \partial N(\mathrm{H\,I})} \tag{6.3}$$

where N is the number of H I absorbers in a given bin between $N(\mathrm{H\,I})$ and $N(\mathrm{H\,I}) + dN(\mathrm{H\,I})$ and

$$dX = \frac{H_0}{H(z)}(1+z)^2. \tag{6.4}$$

We fit this as two power-laws, each having the form,

$$f = A\mathrm{N}(\mathrm{H\,I})^{\beta} \tag{6.5}$$

finding the data fits

$$\begin{aligned} \log f(N_{\mathrm{H\,I}}) &= (-1.72 \pm 0.06) \times \log \mathrm{N_{HI}} + 14.24 \pm 0.81 \ (10^{13.3} < N_{\mathrm{H\,I}} < 10^{16}\mathrm{cm}^{-2}) \\ \log f(N_{\mathrm{H\,I}}) &= (-1.10 \pm 0.20) \times \log \mathrm{N_{HI}} + 3.65 \pm 3.60 \ (10^{17} < N_{\mathrm{H\,I}} < 10^{19.5}\mathrm{cm}^{-2}). \end{aligned} \tag{6.6}$$

Absorbers with log N$<$ 13 tended to be under-detected because low SNR

Table 6.5. Broken power law fits to the column density frequency distribution per unit absorption length

	$10^{13.3} < N_{\rm H\,I} < 10^{16}$ cm^{-2}		$10^{17} < N_{\rm H\,I} < 10^{19.5}$ cm^{-2}	
z	β	A	β	A
all z	-1.72 ± 0.06	14.24 ± 0.81	-1.10 ± 0.19	3.65 ± 3.60
2-2.4	-1.73 ± 0.06	13.56 ± 0.86	-1.04 ± 0.30	2.16 ± 5.35
2.4-2.8	-1.74 ± 0.05	14.02 ± 0.68	-0.99 ± 0.20	1.20 ± 3.64
2.8-3.2	-1.72 ± 0.05	13.64 ± 0.68	-1.04 ± 1.31	2.07 ± 24.09
3.2-3.6	-1.62 ± 0.08	11.84 ± 1.07	-0.49 ± 0.73	-7.62 ± 12.89
3.6-4	-1.60 ± 0.08	11.31 ± 1.10	-0.76 ± 1.78	-2.98 ± 32.05

obscures these absorbers, artificially reducing their frequency and introducing the roll off seen in Figure 6.7. These values are consistent with similar results for large-N (Péroux et al., 2003) and low-N (Kim et al., 2002).

The flattening at 10^{17}cm^{-2} is due to self-shielding (Zheng and Miralda-Escudé, 2002), since this column-density is on the order of the inverse cross section of H I at the ionization energy. For the highest-column density systems, there is another roll-off—which we do not recover here —but is thought to be due to incorporation into molecular gas and stars (Schaye, 2001; Altay et al., 2011).

We see (Figure 6.8) that there is no compelling evidence for redshift evolution of these absorbers for high-N (Lyman limit systems and DLAs), however the errors are large. Prochaska and Wolfe (2009) finds no evidence for evolution of this $f(N)$ with redshift from a survey of DLAs. We do, however, find growth of the column densities starting at $z = 3$. This study is limited in scale so it remains difficult to draw firm conclusions.

The Lyα Forest Optical Depth

The effective optical depth of the Lyα forest ($\tau_{eff} = -\ln\langle F \rangle$), where F is normalized flux, is sensitive to many important cosmological parameters such as Ω_b,

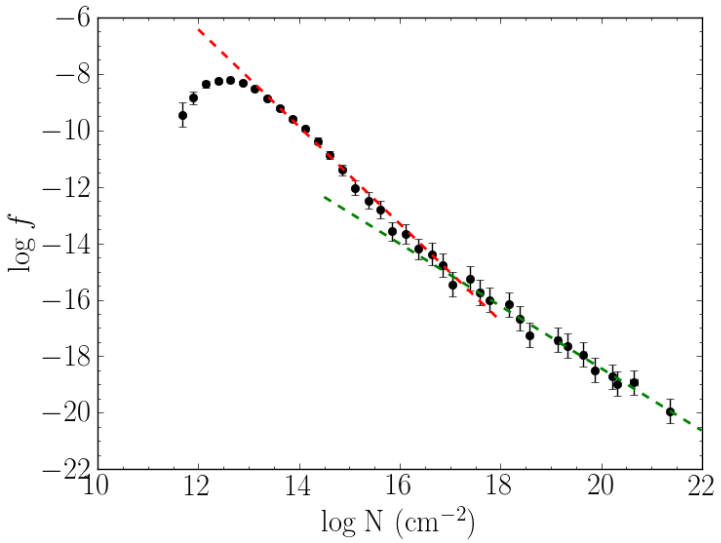

Figure 6.7. H I absorber frequency versus log N per unit absorption distance, dX. The errors on the bins were estimated assuming the number of occurrences of absorbers were Poisson in nature. The roll-off at low-N is due to low-SNR obscuring these absorbers, so they appear less abundant artificially. We fit two power-laws: N= $10^{13.3-16}$ has a power-law slope of $\beta = -1.72 \pm 0.06$ and N= 10^{17-21} fits $\beta = -1.10 \pm 0.20$.

Table 6.6. τ_{eff} with metals flagged and removed binned into $\Delta z = 0.1$.

$1+z$	τ_{eff}	$\delta\tau_{eff}/\sqrt{n}$	$1+z$	τ_{eff}	$\delta\tau_{eff}/\sqrt{n}$
2.95	0.0559	0.0116	4.15	0.4684	0.0159
3.05	0.1822	0.0056	4.25	0.4759	0.0444
3.15	0.1589	0.0034	4.35	0.6236	0.0498
3.25	0.2653	0.0043	4.45	0.6283	0.0453
3.35	0.3324	0.0036	4.55	0.7953	0.0389
3.45	0.2242	0.0024	4.65	0.7139	0.0550
3.55	0.2338	0.0026	4.75	0.7448	0.0475
3.65	0.3070	0.0034	4.85	0.5852	0.0529
3.75	0.3066	0.0036	5.05	1.5134	0.3625
3.85	0.3830	0.0050	5.15	1.3833	0.4132
3.95	0.3622	0.0066	5.25	1.0872	0.2783
4.05	0.4943	0.0083	5.35	1.3639	0.5288

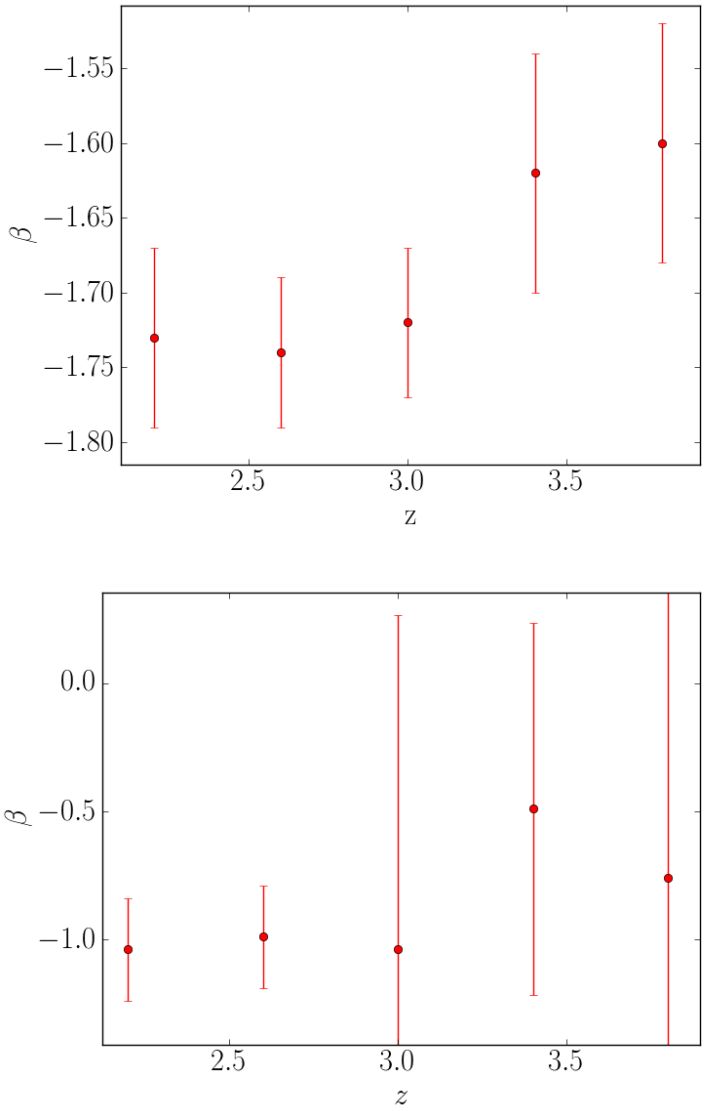

Figure 6.8. H I column density frequency distribution power-law index, β, versus redshift for N= $10^{13.3-16}$ (top) and N= 10^{17-21} (bottom). See Equation 6.5. Lower column densities than $10^{13.3}$ were not considered due to a significant roll-off of detections below N=$10^{13.3}$ caused by under-detection in lower SNR regions of spectra (See Figure 6.7). The low number of large-column systems, at higher redshifts prevent any determination of redshift evolution, however among low-column systems (N= $10^{13.3-16}$), we clearly see growth of our power-law index, β with redshift.

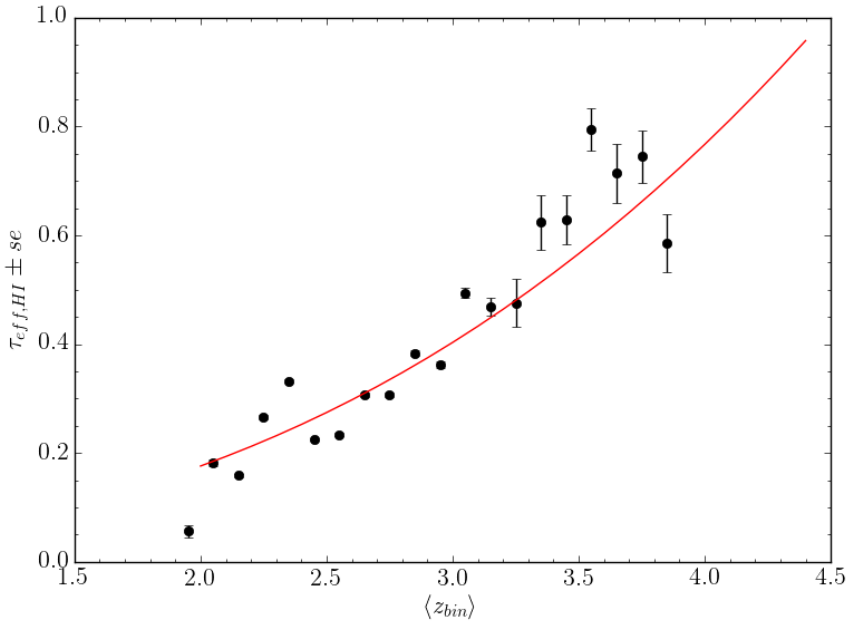

Figure 6.9. τ_{eff} versus redshift in bins of $\Delta z = 0.1$. The error-bars are standard errors calculated from our combined continuum error of 1.2% Kirkman et al. (2005), intrumental error and the standard deviation of flux in $\Delta z = 0.1$ bins. The red curve is the best fit assuming a power-law (see equation 6.8). As for spectral lines suspected of or identified to be metal lines, we removed the corrsponding region of spectrum following equation 6.7. For a tabulated list of these points, see Table 6.6.

Ω_m, Ω_Λ, and parameters which are used in determination of the primordial power spectrum of density fluctuations (Tytler et al., 2004; Viel et al., 2004; Lidz et al., 2006). Additionally it is sensitive to the intensity of spectrum of the metagalactic ionizing background, which is a key parameter for models (Rauch et al., 1997; Bolton et al., 2005).

By Reionization of H I and He II the universe becomes transparent to UV, increasing the power of the metagalactic ionizing background. Bernardi et al. (2003); Faucher-Giguere et al. (2008); Dall'Aglio et al. (2008) reported a dip at $z = 3.2$, which was initially attributed to being a signature He II reionization Theuns et al. (2002). This now stands in contrast to more recent works both in theory and observation (Bolton et al., 2009b,a; McQuinn et al., 2009; Becker et al., 2013).

In Kirkman et al. (2005), the authors calculate the related statistic, $D_A = 1 - \langle F \rangle$ from the same dataset and same continua and attempt also to account for the amount of metal absorption without explicitly identifying metal line absorption. We repeat the analysis, including one more higher-redshift QSO. We bin the dataset into segments of spectrum $\Delta z = 0.1$ wide, considering only the Lyα forest : $\lambda_{rest} = 1070 - 1170$ Å. We cutoff our data at 1170 Å to avoid any impact the QSO may have on the gas and at 1070 Å to avoid any contribution from the Lyβ forest. Unlike Kirkman et al. (2005), we explicitly mask identified metal lines and suspected metal lines by masking wavelength regions in the range:

$$\lambda_{cent}\left(1 - \frac{2b\sqrt{\ln 2}}{c}\right) < \lambda < \lambda_{cent}\left(1 + \frac{2b\sqrt{\ln 2}}{c}\right) \tag{6.7}$$

Propagating flux errors on our data with the reported 1.2% continuum error from Kirkman et al. (2005), we find:

$$\tau_{eff} = A(1+z)^{\gamma} = (0.0074 \pm 0.0022) \times (1+z)^{2.88 \pm 0.22}. \quad (6.8)$$

The power-law index is in good agreement with Kirkman et al. (2005). We are consistent with much of the literature on the matter, though there is some scatter: Press et al. (1993) finds $\gamma = 2.46 \pm 0.37$, Zuo (1993) finds $\gamma = 2.87 \pm 0.23$ from a D_A measurement, Kim et al. (2007) finds $\gamma = 3.61 \pm 0.25$ and Becker et al. (2013) finds $\gamma = 2.90 \pm 0.02$. (See figure 6.9.)

Summary and Conclusions

We report on an updated analysis of the Lyα forest toward 25 QSOs using data from HIRES. Specifically, we measure the temperature-density relation, the distribution of b-values with respect to H I column density and redshift, the H I column density probability distribution and redshift-evolution, and measure the redshift evolution of optical depth.

Using Voigt-profile decomposition of H I absorption lines, we find a nearly flat line width-column density (b-N) distribution. We make no exhaustive effort to map this onto temperature, however, using calculated parameters from Rudie et al. (2012), we find our this is consistent with a $T - \rho$ relation with a positive power law slope, though with some scatter as it was binned into redshift. We performed this test using an established method to trace b Schaye et al. (1999). There is no discernible redshift dependence within the range of our data $z = 1.6 - 4.8$.

We measure the statistic, b_σ, and find a clearly discernible peak at $z = 3$ when binned into redshift. If this can be taken to trace temperature, then this peak is consistent with He II reionization at $z = 3$.

We also measure the column density frequency distribution per absorption

distance (f(N)) for neutral Hydrogen. We find power law slopes $\beta = 1.7$ and $\beta = 1.1$ for log N=$13.3 - 16$ cm^{-2}and log N=$16 - 21$ cm^{-2}, respectively. We find evidence for evolution for the lower column density sample, but due to large errors cannot make any claims about the high column sample.

Lastly, we fit the optical depth of the Lyα forest of our spectra, finding a redshift evolution fitting $\tau_{eff,\mathrm{H\,I}} = (0.0074 \pm 0.0022) \times (1+z)^{2.88\pm0.22}$.

Acknowledgements

This chapter was adapted from work being prepared for publication under the working title *New Statistics of the Lyα forest towards 25 Quasar Absorption Lines*. This work uses data first presented in Kirkman et al. (2005) and continua fit by four undergraduate researchers, discussed therein. The author of this dissertation is the primary author and David Tytler is co-author.

The author wishes to recognize and acknowledge the very significant cultural role and reverence that the summit of Mauna Kea has always had within the indigenous Hawaiian community. We are most fortunate to have the opportunity to conduct observations from this mountain.

The data presented herein were obtained at the W.M. Keck Observatory, which is operated as a scientific partnership among the California Institute of Technology, the University of California and the National Aeronautics and Space Administration. The Observatory was made possible by the generous financial support of the W.M. Keck Foundation.

Appendix A

Software

In this chapter we present a brief overview of selected software packages developed for use in this dissertation.

Spectrum Fitting Software: `dude`

David Kirkman's `dude` was the primary model fitting software used for fitting QSO spectra (see the appendix of Kirkman et al. (2003) for a more in-depth discussion of some of the algorithms involved). It primary capabilities are reading 1D `.fits` or text-based data files and fitting models to the data, guided by human interaction with its graphical interface, which then read and write the resulting model into a human-readable xml format. The user chooses a continuum created with cubic B-spline interpolation specified by user-placed control points. On top of this, the user may fit absorption lines as a Voigt profile. The fit is then optimized using a Levenburg-Marquardt algorithm. This software was found to fit models with hundred of parameters among highly-blended Lyα forest absorbers, with little problem, however with too little guidance, resulting models can be unphysical, so scientific intuition is required. To get a reasonable fit, the user must provide reasonable guess parameters, where 'reasonable' depends on the nature of the data and the number of parameters.

`dude` stores its models in an `.xml` documents as follows:

```
<?xml version="1.0"?>
<SpecTool version="1.0">
<CompositeSpectrum id="/path/to/fits_source.fits">
<!-- pixels and params are number of pixels highlighted for optimizing and
    number of freely-varying params.  This is so the user can get degrees of
    freedom if desired -->
<Spectrum spec="fits_source.fits" error="fits_source_error.fits"
          chi2="123.45" pixels="197.0" params="5"/>
<!-- xError and yError are not implemented in dude.
     y is in flux units, x in Angstroms
    if id is not specified, leave as "null"-->
<ContinuumPoint x="3050.1" y="1.23E-14" xError="0.0" yError="0.0"
                xLocked="true" yLocked="true" id="optional id"/>
<ContinuumPoint x="3057.2" y="1.34E-14" xError="0.0" yError="0.0"
                xLocked="true" yLocked="true" id="null"/>
<!-- add as many ContinumPoint or AbsorberTags as your model requires. -->
<!-- ionName needs to be as entered in dude's atom.dat.
    *Error is not implemented, so needs to stay "0.0".-->
<Absorber ionName="C IV" N="12.90" b="6.01" z="1.9"
          NError="0.0" bError="0.0" zError="0.0"
          NLocked="false" bLocked="false" zLocked="false"
          id="null"/>
</CompositeSpectrum>
<!-- custom velocity plots can be made by editing dude's velplots option-->
<VelocityView id="name" redshift="2.5" minWave="-125.0" maxWave="125.0"
              minFlux="-1.63E-15" maxFlux="5.795E-14"
              restWaves="1215.6701:1025.7223:972.5368:949.7431:926.2257:"
              labels="Ly-1:Ly-2:Ly-3:Ly-4:Ly-7:"/>
<!-- regions which are highlighted for optimizing-->
<Region start="4338.307117" end="4342.921744"/>
```

```
</SpecTool>
```

QSO Spectrum Model Framework: `dudeutils`

`dudeutils` is a Python framework developed to interface with David Kirkman's `DUDE` spectrum fitting software and to manipulate models. At its most basic, it parses the xml file output by `DUDE` for more convenient usage outside of `DUDE`. More typical usage invokes `dudeutils`'s ability to estimate errors using χ^2 or maximum likelihood methods and to construct a covariance matrix from stochastically sampled models.

`dude` stores fitting information in an `.xml` file, which provides human-readable structured data. `dudeutils` takes advantage of this, by storing its own output in an `.xml` database of modified `dude` fitting models. This is useful for quickly iterating through or searching through many models.

One goal of this project, was to be able to visualize model parameters and their effect on χ^2, without having to recalculate a Voigt-profile for hundreds of absorbers. A specialized version of `dude` was modified to allow the user to store model data for each iteration of an LM optimization sequence. This allows the user to store hundreds of models in our database after only a few passes of the optimizer.

Data Structures and API

The most primitive data structures implemented are those individual elements of data, each a subclass of `Data`: absorbers (`Absorber`), continuum control points (`ContinuumPoint`), optimization regions (`Region`) and the spectrum views implemented in `DUDE` (`SingleView` and `VelocityView`). Note that `DUDE` makes use of the same names for objects of the same use. These are merely reimplementations

that can be used outside of the DUDE environment. While typically not necessary, each of these may be implemented as in the following example:

```
>>> from dudeutils.data_types import *
>>> import xml.etree.ElementTree as et
>>> #create a typical xml node that dude would create
>>> string="""<Absorber ionName="C IV" N="11.8" b="4.7" z="1.9"
...            NError="0.0" bError="0.0" zError="0.0"
...            NLocked="false"  bLocked="false" zLocked="false" id=""/>"""
>>>
>>> node=et.fromstring(string)
>>>
>>> #use the factory method to instantiate new data elements
>>> absorber=Data.factory(node=node)
>>> str(absorber)
'C IV  id=       N=11.80000 b= 4.70000 z=1.90000000'
>>>
>>> #or specify an xmlfile and an id
>>> cont_point=Data.factory(xmlfile="this.xml",tag="ContinuumPoint",id="the_id")
```

These elements, in turn, are composed into list-like of objects for each model, each a subclass of `ObjList`. Each `Model` instance will have no more than one instance of these subclasses: `ContinuumPointList` a container for `ContinuumPoint`, `AbsorberList` a container for `Absorber`, and similarly for our list of optimization regions `RegionList`, list of spectrum views in wavelength `SingleViewList`, and list of spectrum views in velocity, `VelocityViewList`.

When these are created, they are automatically inserted into a common pool of these `ObjList` subclass instances. This is necessary to avoid having numerous copies of the same data list, since often times, the only thing changing between two models are a few absorption parameters.

```
>>> from dudeutils.data_types import *
>>> import xml.etree.ElementTree as et
```

to create a new list from a list of Data subclass instances:

```
>>> objlist= [Data.factory(item, 'Absorber', 'an_id') for item in iterable_data]
>>> new_list=ObjList.factory(objlist)
```

if `id` is specified, then ObjList.factory will instead search `ObjList._pool` for the entry and return that instead.

```
>>> other_list=ObjList.factory(id=new_list.id)
>>> other_list is new_list
True
```

Typically the user will only ever need to interface with the `Model` and `ModelDB` instances from `model.py`. The `Model` allows direct interaction with a `DUDE` model, providing methods for reading, writing, and getters and setters for the different attributes of the models.

```
>>> from dudeutils.model import *
>>> model=Model(xmlfile='/path/name/filename.xml')
>>> len(model.AbsorberList)
36
>>> model.AbsorberList
'43a7c1e4-d0a2-49f1-9bd2-df21d1781a5a'
>>> Model.get(model.AbsorberList)
<data_types.AbsorberList object at 0x7f0f4c442080>
>>> str(Model.get(model.AbsorberList)[0])
'C IV  id=CIV7   N=12.90636 b= 6.01024 z=1.92197100'
>>> model.get_datum(iden='DIA',tag='Absorber')
<data_types.Absorber object at 0x7f0f4c419a20>
>>> model.get_datum(iden='DIA',tag='Absorber',param='N')
```

```
15.902669
>>> model.chi2, model.params, model.pixels
(2709.740602, 11, 1951)
>>> model.get_vel('DIA','DIB')
-12.215886992744391
```

or to re-read the `xml` or write our model back to source we use the

```
model.read()
```

and

```
model.write()
```

respectively.

A list of models can then be described as a `ModelDB` instance, which provides a handy list-like data structure for models with some extended functionality.

```
>>> from dudeutils.model import *
>>> db=ModelDB(models=[Model(xmlfile=item) for item in file_list])
>>> len(db)
2454
>>> db.constrain(some_constraints)
```

We also provide an interface to facilitate pickling and unpickling:

```
>>> ModelDB.dump_models(db,fname="binary_object_dump_name.obj")
>>> new_db=ModelDB.load_models(fname="binary_object_dump_name.obj")
```

Of particular note is the data constraining utility, which is widely used throughout processing of model databases:

```
>>> from dudeutils.constraints import Constraints
>>> constraint_dct = {"chi2":1234,                #upper limit for chi2
```

```
...                 "params":3,"pixels":2345, #filter only model with these
...                                           #exact number of params and pixels
...                 "D":{"N":(12.3,14.3),"b":(15,16)} #abs_id:{param:(limits)}
...                 "H": {"b":(11.,15.)}
...               }
>>> constraints=Constraints(**constraint_dct)
>>> db.constrain(constraints)
>>> len(db)
543
```

Many of the most frequently used utilities are implemented in `utilities.py`.

```
>>> from dudeutils.utilities import *
>>> from model import Model, ModelDB
```

Here we call a commandline option to optimize some xml model with dude

```
>>> run_optimize("model.xml",step=True, method='dude',timeout=30)
```

if optimization is stepped, then a number of files `iteration_*.xml` will be written to the working directory, so we use `populate_database` to load them to a `ModelDB` instance.

```
>>> db=populate_database(path="/path/to/iteration_steps/")
>>> type(db) is ModelDB
True
```

Or alternatively, it may be advantageous to only add the final result of the optimization.

```
>>> run_optimize("model.xml",step=False, method='dude',timeout=30)
>>> model.read()  #re-read in order to reflect changes from dude
>>> db.models.append(model.copy())
```

This just appends the best model to our `ModelDB` instance need to append a copy, so we don't have two references to the same object

Determining Parameter Errors

While `DUDE` does find a locally best-fitting model, it does not attempt to estimate parameter errors, since errors in this line of work come from multiple, sometimes poorly understood sources. In `dudeutils`, however, we provide an interface for estimating a set of parameter errors and statistical correlations by randomly sampling a user defined section of parameter space.

As discussed in Section 2.2, we use χ^2 methods methods to estimate the errors of the parameters where our errors are determined by parameter values from models with χ^2 within $\chi^2(model) < \chi^2_{min} + \Delta$, where Δ depends on the number of interesting parameters and desired significance level.

These methods are implemented in `random_sampling.py`, which uses Monte Carlo methods to sample different parameters when the parameters of interest are locked to a particular value. In order it,

1. randomly vary all parameters of interest within a range specified in the config file.
2. lock parameter(s) of interest to the locked values
3. optimize dude around the locked values
4. repeat until a sufficient portion of parameter-space is explored
5. find the values of each locked parameter required to yield models within $\chi^2(model) < \chi^2_{min} + \Delta$

A script to estimate errors may look like

```
from dudeutils import random_sampling, utilities, model
from dudeutils.plot_distribution import plot_chi2
```

```
"""
Here we perform random_sampling on an already existing model database,
all_db, and then plot out the results.
"""

if __name__ == "__main__":
#parse configuration files
    ab_cfg=random_sampling.parse_config("data/random_sampling_config.cfg")
    cont_cfg=ab_cfg.pop('continuum',None)
    glob=ab_cfg.pop('config',None)

    all_db=utilities.load_models('model_db.obj')
    model=all_db[0]

    all_db=random_sampling.random_sampling(
                all_db, model, ab_cfg, cont_cfg, **glob)
#filter out results
    all_db=random_sampling.filter_bad_models(all_db, ab_cfg)

#to write out results
    dudeutils.dump_models(all_db,'model_db.obj')

# now plot out results
    for key, val in ab_cfg.items():
        for attr in list(val.keys()):
            plot_chi2(all_db, iden=key, attr=attr,
                      xlabel="x label",
                      constraints={})
```

Determining Continuum Level

Besides varying parameter values, we can also choose a random selection of continua, which is use to observe the effect of continuum level on our other parameters. To find each continuum, the program randomly varies each parameter value and continuum control point as specified in `data/random_sampling_config.cfg`. Then the code proceeds to alternate between optimizing over absorption parameters and continuum control point locations until the fit arrives at a local minimum of χ^2, at which point the new continuum is returned. A script to vary the continua may look something like:

```
from dudeutils import model, utilities, random_sampling
from dudeutils.spec_parser import Spectrum

if __name__ == "__main__":

    #prep these config dicts
    ab_cfg=random_sampling.parse_config('config_file.cfg')
    cont_cfg = ab_cfg.pop('continuum')
    glob=ab_cfg.pop('config')

    spec=Spectrum.sniffer('source_file.xml')
    db=utilities.load_models('pickled_ModelDB.obj')

    #to initially ensure that all continuum_points are locked prior to
    #running random_sampling.vary_cont
    toggle_cont_lock(src_model,list(cont_cfg.keys()),True,param='x')

    models=[]
    #find n_continua
    for i in range(n_continua):
```

```
        #choose initial guess continuum and guess value for parameters
        #then alternate between optimizing continua and parameters until
        #dude can no longer improve fit.
        new_model=random_sampling.vary_cont(model,ab_cfg,cont_cfg)
        models.append( new_model )
```

yielding continua such as in Figure 3.7.

Extended `Makee` Pipeline Software: `hires-extract`

Motivation

`hires-extract` was initially intended as a simple wrapper to Tom Barlow's `MAKEE` extraction code for HIRES and ESI spectra, but since it's inception had been extended to allow for a number of general tools on data including several post-processing utilities. At its core, `hires-extract` organizes source `.fits` files and assembles all of the requisite input for `MAKEE` extraction and reduction.

Workflow

After specifying all requisite data into the config file, `data/input.cfg`, The user may then inialize and run whichever utilities they need. For most purposes, (extraction and reduction) the following minimal pipeline script will suffice:

```
#!/usr/bin/env python
from hiresExtract import makeeUtils, spectra, errorChecks, combine, fileIO
from hiresExtract.config import glob, obj_names, config
import os

lst = [spectra.SciTarg(config[item]) for item in obj_names]
paths=list(set([item.raw.path for item in lst]))
```

```
if glob.extract:  #extract the spectra
    for qso in lst:
        qso.stack_cals()
        errorChecks.checkImageSize(qso.std.raw.fullname,qso.raw.fullname)
        qso.test_names()
        qso.makee()      #extract the science target and std star

if glob.flux: #flux the spectra
#to ensure that something isn't trimmed more than once, add done items to list
    trimmed=[]
    for qso in lst:
        #do fluxcals for each ccd
        os.chdir(qso.raw.path)
        if glob.verbose: print('    fluxing '+qso.raw.base)

        #trim 2D spec to desired size off the end
        if glob.extract:
            for item in [qso.Object, qso.std.Object,
                         qso.Sky, qso.Error, qso.std.Error]:
                for j in [0,1,2]:
                    if not item[j].fullname in trimmed:
                        spectra.Spec.trim2D(item[j].fullname,col=int(glob.cols))
                        trimmed.append(item[j].fullname)
        qso.fluxCal()
        qso.combine()
        qso.std.combine()
        makeeUtils.run('combine','-loglin',
            input_files=[qso.SkyFluxed[i].fullname for i in [0,1,2]],
            of=qso.SkyFinal.fullname, disp=str(glob.disp))
        try:
#flag areas with no data so they aren't included in the coadding
```

```
            spectra.Spec.check_ranges(qso,interactive=False)
        except:
            print("no ranges specified...ignoring")

if glob.combine:  #combine the spectra.  May want to check quality first
    spectra.Spec.align_lst(lst)
    os.chdir(glob.homepath)
    for qso in lst:
        qso.crop_waves()
    combine.combineSpec(lst)
```

which reads from a user-specified configuration file:

```
[global]
name: J0744+2059
ssdbpath: /path/to/makee/ssdb
homepath: /path/to/output/data
disp: 2.1
loglin: yes
flux: no
extract: no
combine: yes
snrwave: 4463.
verbose: yes
skysub: no
wavelength_range:3145,5994
linebottoms:
ncols: 5
match_levels: no
ascii_dump: no

[object_ID_name]
```

```
raw: /path/to/source/object_ID_name.fits
std: standard_star_spectrum_name
arc: arc_lines_spectrum_name
flats:  flat01-flatXX
bwr: standard_star_bad_wavelength_region.bwr
biases: bias01-biasXX
#wavelength pairs of regions to cuts
wave_cut: 3190.8,3194.5, 3670.2,3670.4

[256]
raw: /media/scott/FantomHD/data/KI1209/hires0256.fits
std: hires0253
arc: hires0130
flats:  hires0206-hires0216
bwr: f34.bwr
biases: hires0508-hires0517, hires0519-hires0527
wave_cut: 4860.6,4866,5077,5126.8,4075,4127.5
```

Following traditional procedures, the data is first extracted, wavelength calibrated, fluxed, and then if more than one spectra are present, combined. It is important to mention that after running the pipeline, it is prudent that the user does some quality checking of both the final output spectra as well as the intermediate images. It is this reason that all intermediate steps are saved and given their own respective naming convention (see section A.6.2). These data are then organized into all data relevant to our science targets and for our standard stars for flux calibration.

Data Structures and API

Spectrum data types

`spectra.py` defines classes for data processing. `Spec` which contains the most commonly used methods for interacting with spectrum data. `SciTarg` and `Std` inherit from `Spec` and have more specialized utilities for the science targets and standard stars respectively.

```
>>> import spectra
>>> from config import glob, obj_names, config
>>> #import global data, target names and configuration data
>>> sp=spectra.SciTarg(config['123'])
```

Here, we initialize a `SciTarg` Object named '123'. After initializing, we can run the utility functions to proceed with extraction and fluxing.

```
>>> sp.stack_cals()
>>> #stack flat and bias frames.
>>> sp.makee()
>>> #calls makee through the shell. Options determined in data/input.cfg
```

At this point, it would be prudent to check the quality of the unfluxed spectra. If satisfactory, then proceed with flux calibration.

```
>>> type(sp.std) #upon invocation, SciTarg instantiates its standard star
<class 'spectra.Std'>
>>> qso.fluxCal()  #perform flux calibration
>>> qso.combine()  #combine constituent spectra, from HIRES mosaic
>>> qso.std.combine() #combine constituent standard star spectra.
```

Defining Custom `filetype` Classes

Typically, a user will keep a copy of the data at each step during the extraction and reduction process for quality control purposes. `MAKEE` has a default naming convention for each of these steps, so the naming of a file will indicate its purpose. Naming and assigning the correct location for data files is then very important. Additionally, a user may wish to add their own extended functionality, which would then complicate matters further.

To address this issue, the user may define custom classes, or alter the naming convention for any data class by altering `data/filetypes.cfg`. Each section header describes the primary function of the files: Input, Output, Verification, FluxCal and Custom for the input data, output data, data used for quality control, intermediate flux calibration data and several custom defined types, respectively. `data/filetypes.cfg` is of the form:

```
# each section header (‘[Output]‘ for example) describes a parent class for each
# file type which will become its own directory.
#
# some file types will have a suffix denoting ("_1", "_2", "_3").  This is
# ignored here but will be automatically entered in the code.
# for example:  a file called "foo_1.fits" will simply be called "foo.fits" here
# but will be added later in the code
#
# split up for each CCD.  (For example, Flux-###_1.fits, Flux-###_2.fits,
# Flux-###_2.fits)
# the rest indicate a filetype that will be encountered and implemented as its
# own class in the code.
#
# see MAKEE documentation for descriptions of file types
```

```
[Output]
#MAKEE standard outputs

splitraw : hires
Object : Flux-
Error : Err-
Sky : Sky-
FlatOut : flat_out
BiasOut : bias_out
S2N : s2n-
DN : DN-
Sum: Sum-
ArcOut : Arc-
ArcLines : Arc-, .ids
ArcSkyLineShift : Arc-, -sky.ps


[Verification]
#MAKEE verification files

Var: Var-
Log : hires, .log
Trace : trace-, .ps
Profile : profiles-, .ps
SkylineShift : Flux-, -skyshift.ps
Arcfr : Arc-, -fr.ps
ArcCorrelation : Arc-, -cf.ps
ArcResiduals : Arc-, .res
```

```
[Input]
#other types.  input type will be like hires####.fits.
#here we will rename for ease of lookup post-extraction.
#ex.  item.std.name=stdXXXX.fits
std : std
raw : raw
flat : flat
arc : arc
bias : bias

[FluxCal]
#types created during flux calibration

Zero : Flux-, -zero
Response : Resp-
Smoothed : Resp-, -smooth
Fluxed : Flux-final-
Fluxede : Err-final-

SkyFluxed:SkyF-
SkyFluxede:SkyE-

[Custom]
ascii:ascii_, .dat
asciiE:asciiE_, .dat
SkyFinal:sky_final_
SkyFinale:sky_final, e
final:final_
finale:final_, e
```

Upon invocation, `filetypes.py` will instantiate each of the elements of

these sections as a new class where the key is the class name and the value is the file naming convention. For example:

```
>>> type(item)
spectra.Spec
>>> item.std.name
'std1234.fits'
>>> item.Fluxed[0].name
'Flux-final-1234_1.fits'
>>> item.Flux[0].path
'path/to/all/other/FluxCal/subclass/types'
```

You can access the class with one of two dictionaries: for the parent classes, which do not ever get explicitly instantiated

```
>>> from filetypes import File
>>> parent=File.parents['FluxCal']
>>> type(parent)
<class 'type'>
```

and for the subclasses, which you will instantiate

```
>>> type(File.all_type['raw'])
<class 'type'>
```

You may even define a custom type on the command line:

```
>>> new_type=File.class_factory('new_type_name', parent)
>>> type(new_type)
<class 'type'>
>>> File.all_types['new_type_name'] is new_type
True
```

Note that here, the class names are stored in either File.parents for the parent classes (`Input`, `Output`, `Verification`, `FluxCal`, `Custom`) or `File.all_types`, for the children (subclasses).

To create and instance of that particular class:

```
>>> new_file=File.factory(filetype=new_type,filename='name')
```

Or by class name,

```
>>> another_new_file=File.factory(filetype='new_type_name',filename='name')
>>> type(new_file)==type(another_new_file)==new_type
True
```

Correcting Residual Flux

In both J1201+0116 and J0744+2059, certain saturated absorption lines were had significantly non-zero line bottoms. This is thought to have come from incomplete sky subtraction within `MAKEE`. This can be adequately corrected with tools from `sky_subtract.py`.

```
import wavelength
import astropy.io.fits as fits
from sky_subtract import *

"""
Script to correct unsubtracted flux using sky_subtract.  'regions.dat'
specifies saturated absorption lines to sample and is formatted as
4123,4124
4325,4327
...
...
etc.
```

```
"""

if __name__ == "__main__":
    filename="fits_file_to_be_corrected.fits"

    beg, end=np.loadtxt("regions.dat", unpack=True)
    region_list = list(zip(beg.tolist(), end.tolist()))

    order = 1 #order of polynomial fitting regions

    x,y = wavelength.xy(filename)  #get wavelength, flux
    hdu = fits.open(filename)
    hdu[0].data = sky_subtract(x,y, region_list, order=order)
    hdu.writeto("new.fits")
    hdu.close()
```

This correction is accomplished by sampling a range of saturated absorption lines. The code then measures the offset from zero for each of these and calculates a flux correction function. By default, the code uses linear regression to determine this flux correction function, however, if the correction is non-linear, then some higher-order polynomial fit can be chosen when invoking `sky_subtract.sky_subtract` using the keyword argument `order`.

Bibliography

Gabriel Altay, Tom Theuns, Joop Schaye, Neil HM Crighton, and Claudio Dalla Vecchia. Through thick and thin—h i absorption in cosmological simulations. *The Astrophysical Journal Letters*, 737(2):L37, 2011.

M. Asplund, N. Grevesse, A. J. Sauval, and P. Scott. The Chemical Composition of the Sun. *ARA&A*, 47:481–522, September 2009. doi: 10.1146/annurev.astro.46.060407.145222.

E. Aver, K. A. Olive, and E. D. Skillman. The effects of He I λ10830 on helium abundance determinations. *J. Cos.& Astroparticle Phys.*, 7:011, July 2015. doi: 10.1088/1475-7516/2015/07/011.

Y. Avni. Energy spectra of X-ray clusters of galaxies. *Astrophys. J.*, 210:642–646, December 1976. doi: 10.1086/154870.

SA Balashev, EO Zavarygin, AV Ivanchik, KN Telikova, and DA Varshalovich. The primordial deuterium abundance: subdla system at zabs= 2.437 towards the qso j 1444+ 2919. *Monthly Notices of the Royal Astronomical Society*, 458(2): 2188–2198, 2016.

J. Bechtold. Quasar Absorption Lines. *ArXiv Astrophysics e-prints*, December 2001.

George D Becker, Michael Rauch, and Wallace LW Sargent. The evolution of optical depth in the lyα forest: Evidence against reionization at z˜ 6the observations were made at the wm keck observatory, which is operated as a scientific partnership between the california institute of technology and the university of california; it was made possible by the generous support of the wm keck foundation. *The Astrophysical Journal*, 662(1):72, 2007.

George D Becker, James S Bolton, Martin G Haehnelt, and Wallace LW Sargent. Detection of extended he ii reionization in the temperature evolution of the intergalactic medium. *Monthly Notices of the Royal Astronomical Society*, 410

(2):1096–1112, 2011.

George D Becker, Paul C Hewett, Gábor Worseck, and J Xavier Prochaska. A refined measurement of the mean transmitted flux in the lyα forest over $2 < z < 5$ using composite quasar spectra. *Monthly Notices of the Royal Astronomical Society*, 430(3):2067–2081, 2013.

C. L. Bennett, D. Larson, J. L. Weiland, N. Jarosik, G. Hinshaw, N. Odegard, K. M. Smith, R. S. Hill, B. Gold, M. Halpern, E. Komatsu, M. R. Nolta, L. Page, D. N. Spergel, E. Wollack, J. Dunkley, A. Kogut, M. Limon, S. S. Meyer, G. S. Tucker, and E. L. Wright. Nine-year Wilkinson Microwave Anisotropy Probe (WMAP) Observations: Final Maps and Results. *Astrophys. J., Suppl. Ser.*, 208: 20, October 2013. doi: 10.1088/0067-0049/208/2/20.

Mariangela Bernardi, Ravi K Sheth, Mark Subbarao, Gordon T Richards, Scott Burles, Andrew J Connolly, Joshua Frieman, Robert Nichol, Joop Schaye, Donald P Schneider, et al. A feature at z 3.2 in the evolution of the lyα forest optical depth. *The Astronomical Journal*, 125(1):32, 2003.

Elisa Boera, Michael T Murphy, George D Becker, and James S Bolton. The thermal history of the intergalactic medium down to redshift z= 1.5: a new curvature measurement. *Monthly Notices of the Royal Astronomical Society*, 441 (3):1916–1933, 2014.

James S Bolton, Martin G Haehnelt, Matteo Viel, and Volker Springel. The lyman a forest opacity and the metagalactic hydrogen ionization rate at z 2–4. *Monthly Notices of the Royal Astronomical Society*, 357(4):1178–1188, 2005.

James S Bolton, S Peng Oh, and Steven R Furlanetto. The evolution of the lyα forest effective optical depth following he ii reionization. *Monthly Notices of the Royal Astronomical Society*, 396(4):2405–2418, 2009a.

James S Bolton, S Peng Oh, and Steven R Furlanetto. Photoheating and the fate of hard photons during the reionization of he ii by quasars. *Monthly Notices of the Royal Astronomical Society*, 395(2):736–752, 2009b.

James S Bolton, George D Becker, Martin G Haehnelt, and Matteo Viel. A consistent determination of the temperature of the intergalactic medium at redshift $< z >= 2.4$. *Monthly Notices of the Royal Astronomical Society*, 438(3): 2499–2507, 2014.

JS Bolton, M Viel, T-S Kim, MG Haehnelt, and RF Carswell. Possible evidence for

an inverted temperature–density relation in the intergalactic medium from the flux distribution of the lyα forest. *Monthly Notices of the Royal Astronomical Society*, 386(2):1131–1144, 2008.

Greg L Bryan and Marie E Machacek. The b distribution of the lyα forest: Probing cosmology and the intergalactic medium. *The Astrophysical Journal*, 534(1):57, 2000.

S. Burles and D. Tytler. The Deuterium Abundance toward Q1937-1009. *Astrophys. J.*, 499:699–712, May 1998a.

S. Burles and D. Tytler. The Deuterium Abundance toward QSO 1009+2956. *Astrophys. J.*, 507:732–744, November 1998b. doi: 10.1086/306341.

S. Burles, D. Kirkman, and D. Tytler. Deuterium toward Quasar Q0014+813. *Astrophys. J.*, 519:18–21, July 1999. doi: 10.1086/307331.

F Calura, E Tescari, V D'Odorico, M Viel, S Cristiani, T-S Kim, and JS Bolton. The lyman α forest flux probability distribution at z¿ 3. *Monthly Notices of the Royal Astronomical Society*, 422(4):3019–3036, 2012.

Alain Coc, Patrick Petitjean, Jean-Philippe Uzan, Elisabeth Vangioni, Pierre Descouvemont, Christian Iliadis, and Richard Longland. New reaction rates for improved primordial d/h calculation and the cosmic evolution of deuterium. *Physical Review D*, 92(12):123526, 2015.

R. Cooke and M. Pettini. The primordial abundance of deuterium: ionization correction. *MNRAS*, 455:1512–1521, January 2016. doi: 10.1093/mnras/stv2343.

R. Cooke, M. Pettini, C. C. Steidel, G. C. Rudie, and P. E. Nissen. The most metal-poor damped Lyα systems: insights into chemical evolution in the very metal-poor regime. *Mon. Not. R. Astron. Soc.*, 417:1534–1558, October 2011. doi: 10.1111/j.1365-2966.2011.19365.x.

R. J. Cooke, M. Pettini, R. A. Jorgenson, M. T. Murphy, and C. C. Steidel. Precision Measures of the Primordial Abundance of Deuterium. *Astrophys. J.*, 781:31, January 2014. doi: 10.1088/0004-637X/781/1/31.

N. H. M. Crighton, J. K. Webb, A. Ortiz-Gil, and A. Fernández-Soto. Deuterium/hydrogen in a new Lyman limit absorption system at z= 3.256 towards PKS1937-1009. *Mon. Not. R. Astron. Soc.*, 355:1042–1052, December 2004. doi: 10.1111/j.1365-2966.2004.08390.x.

R. H. Cyburt, B. D. Fields, K. A. Olive, and T.-H. Yeh. Big Bang Nucleosynthesis: 2015. *ArXiv e-prints*, May 2015.

R. H. Cyburt, B. D. Fields, K. A. Olive, and T.-H. Yeh. Big bang nucleosynthesis: Present status. *Reviews of Modern Physics*, 88(1):015004, January 2016. doi: 10.1103/RevModPhys.88.015004.

Aldo Dall'Aglio, Lutz Wisotzki, and Gábor Worseck. An unbiased measurement of the uv background and its evolution via the proximity effect in quasar spectra. *Astronomy & Astrophysics*, 491(2):465–481, 2008.

S. Dodelson. *Modern Cosmology*. Academic Press. Academic Press, 2003. ISBN: 9780122191411.

I. Dvorkin, E. Vangioni, J. Silk, P. Petitjean, and K. A. Olive. Evolution of dispersion in the cosmic deuterium abundance. *MNRAS*, 458:L104–L108, May 2016. doi: 10.1093/mnrasl/slw028.

Tyler M Evans and Michael T Murphy. A new method for detecting velocity shifts and distortions between optical spectra. *The Astrophysical Journal*, 778(2):173, 2013.

X. Fan, M. A. Strauss, R. H. Becker, R. L. White, J. E. Gunn, G. R. Knapp, G. T. Richards, D. P. Schneider, J. Brinkmann, and M. Fukugita. Constraining the Evolution of the Ionizing Background and the Epoch of Reionization with z˜6 Quasars. II. A Sample of 19 Quasars. *AJ*, 132:117–136, July 2006. doi: 10.1086/504836.

Claude-André Faucher-Giguere, Jason X Prochaska, Adam Lidz, Lars Hernquist, and Matias Zaldarriaga. A direct precision measurement of the intergalactic lyα opacity at $2 \leq z \leq 4.2$. *The Astrophysical Journal*, 681(2):831, 2008.

G. J. Ferland, R. L. Porter, P. A. M. van Hoof, R. J. R. Williams, N. P. Abel, M. L. Lykins, G. Shaw, W. J. Henney, and P. C. Stancil. The 2013 Release of Cloudy. *Rev. Mex. Astronomía y Astrofísica*, 49:137–163, April 2013.

B. D. Fields. The Primordial Lithium Problem. *Annual Review of Nuclear and Particle Science*, 61:47–68, November 2011. doi: 10.1146/annurev-nucl-102010-130445.

M. Fumagalli, J. M. O'Meara, and J. X. Prochaska. Detection of Pristine Gas Two Billion Years After the Big Bang. *Science*, 334:1245–, December 2011. doi: 10.1126/science.1213581.

Antonella Garzilli, JS Bolton, T-S Kim, S Leach, and Matteo Viel. The intergalactic medium thermal history at redshift z= 1.7–3.2 from the lyα forest: a comparison of measurements using wavelets and the flux distribution. *Monthly Notices of the Royal Astronomical Society*, 424(3):1723–1736, 2012.

K. Griest, J. B. Whitmore, A. M. Wolfe, J. X. Prochaska, J. C. Howk, and G. W. Marcy. Wavelength Accuracy of the Keck HIRES Spectrograph and Measuring Changes in the Fine Structure Constant. *Astrophys. J.*, 708:158–170, January 2010. doi: 10.1088/0004-637X/708/1/158.

F. Haardt and P. Madau. Radiative Transfer in a Clumpy Universe. IV. New Synthesis Models of the Cosmic UV/X-Ray Background. *Astrophys. J.*, 746:125, February 2012. doi: 10.1088/0004-637X/746/2/125.

G. Hinshaw, D. Larson, E. Komatsu, D. N. Spergel, C. L. Bennett, J. Dunkley, M. R. Nolta, M. Halpern, R. S. Hill, N. Odegard, L. Page, K. M. Smith, J. L. Weiland, B. Gold, N. Jarosik, A. Kogut, M. Limon, S. S. Meyer, G. S. Tucker, E. Wollack, and E. L. Wright. Nine-year Wilkinson Microwave Anisotropy Probe (WMAP) Observations: Cosmological Parameter Results. *ApJS*, 208:19, October 2013. doi: 10.1088/0067-0049/208/2/19.

L. Hui and N. Y. Gnedin. Equation of state of the photoionized intergalactic medium. *MNRAS*, 292:27, November 1997. doi: 10.1093/mnras/292.1.27.

L. Hui and R. E. Rutledge. The b Distribution and the Velocity Structure of Absorption Peaks in the Lyα Forest. *ApJ*, 517:541–548, June 1999. doi: 10.1086/307202.

AV Ivanchik, P Petitjean, SA Balashev, R Srianand, DA Varshalovich, C Ledoux, and P Noterdaeme. Hd molecules at high redshift: the absorption system at z= 2.3377 towards q 1232+ 082. *Monthly Notices of the Royal Astronomical Society*, 404(3):1583–1590, 2010.

YI Izotov, TX Thuan, and NG Guseva. A new determination of the primordial he abundance using the he i λ10830 å emission line: cosmological implications. *Monthly Notices of the Royal Astronomical Society*, 445(1):778–793, 2014.

T-S Kim, Robert F Carswell, Stefano Cristiani, Sandro D'Odorico, and Emanuele Giallongo. The physical properties of the lyα forest at z¿ 1.5. *Monthly Notices of the Royal Astronomical Society*, 335(3):555–573, 2002.

T-S Kim, JS Bolton, M Viel, MG Haehnelt, and RF Carswell. An improved

measurement of the flux distribution of the lyα forest in qso absorption spectra: the effect of continuum fitting, metal contamination and noise properties. *Monthly Notices of the Royal Astronomical Society*, 382(4):1657–1674, 2007.

D. Kirkman, D. Tytler, N. Suzuki, J. M. O'Meara, and D. Lubin. The Cosmological Baryon Density from the Deuterium-to-Hydrogen Ratio in QSO Absorption Systems: D/H toward Q1243+3047. *Astrophys. J., Suppl. Ser.*, 149:1–28, November 2003. doi: 10.1086/378152.

David Kirkman, David Tytler, Nao Suzuki, Carl Melis, Susan Hollywood, Kory James, Geoffrey So, Dan Lubin, Tridivesh Jena, Michael L Norman, et al. The h i opacity of the intergalactic medium at redshifts $1.6 < z < 3.2$. *Monthly Notices of the Royal Astronomical Society*, 360(4):1373–1380, 2005.

VV Klimenko, SA Balashev, AV Ivanchik, and DA Varshalovich. A new estimation of hd/2h2 at high redshift using the spectrum of the quasar j 2123-0050. In *Journal of Physics: Conference Series*, volume 661, page 012005. IOP Publishing, 2015.

K. M. Lanzetta, A. M. Wolfe, D. A. Turnshek, L. Lu, R. G. McMahon, and C. Hazard. A new spectroscopic survey for damped Ly-alpha absorption lines from high-redshift galaxies. *ApJS*, 77:1–57, September 1991. doi: 10.1086/191596.

C. Ledoux, P. Petitjean, and R. Srianand. The Very Large Telescope Ultraviolet and Visible Echelle Spectrograph survey for molecular hydrogen in high-redshift damped Lyman α systems. *MNRAS*, 346:209–228, November 2003. doi: 10.1046/j.1365-2966.2003.07082.x.

S. A. Levshakov, W. H. Kegel, and F. Takahara. The D/H ratio at z=0.7 toward Q 1718+4807. *A&A*, 336:L29–L32, August 1998a.

S. A. Levshakov, D. Tytler, and S. Burles. Deuterium to hydrogen towards QSO 1009+2956 from a mesoturbulent model. *ArXiv Astrophysics e-prints*, December 1998b.

S. A. Levshakov, M. Dessauges-Zavadsky, S. D'Odorico, and P. Molaro. Molecular Hydrogen, Deuterium, and Metal Abundances in the Damped Lyα System at z_{abs}=3.025 toward Q0347-3819. *ApJ*, 565:696–719, February 2002. doi: 10.1086/324722.

Adam Lidz, S Peng Oh, and Steven R Furlanetto. Have we detected patchy reionization in quasar spectra? *The Astrophysical Journal Letters*, 639(2):L47,

2006.

Adam Lidz, Claude-André Faucher-Giguère, Aldo Dall'Aglio, Matthew McQuinn, Cora Fechner, Matias Zaldarriaga, Lars Hernquist, and Suvendra Dutta. A measurement of small-scale structure in the $2.2 \leq z \leq 4.2$ lyα forest. *The Astrophysical Journal*, 718(1):199, 2010.

Jeffrey L Linsky, Alexander Brown, Ken Gayley, Athanassios Diplas, Blair D Savage, Thomas R Ayres, Wayne Landsman, Steven N Shore, and Sara R Heap. Goddard high-resolution spectrograph observations of the local interstellar medium and the deuterium/hydrogen ratio along the line of sight toward capella. *The Astrophysical Journal*, 402:694–709, 1993.

Jeffrey L Linsky, Athanassios Diplas, Brian E Wood, Alexander Brown, Thomas R Ayres, and Blair D Savage. Deuterium and the local interstellar medium properties for the procyon and capella lines of sight. *The Astrophysical Journal*, 451:335, 1995.

Jeffrey L Linsky, Bruce T Draine, HW Moos, Edward B Jenkins, Brian E Wood, Cristina Oliveira, William P Blair, Scott D Friedman, Cecile Gry, David Knauth, et al. What is the total deuterium abundance in the local galactic disk? *The Astrophysical Journal*, 647(2):1106, 2006.

Limin Lu, Wallace LW Sargent, Thomas A Barlow, Christopher W Churchill, and Steven S Vogt. Abundances at high redshifts: The chemical enrichment history of damped lyα galaxies. *The Astrophysical Journal Supplement Series*, 107(2): 475, 1996.

G. Mangano, G. Miele, S. Pastor, T. Pinto, O. Pisanti, and P. D. Serpico. Relic neutrino decoupling including flavour oscillations. *Nuclear Physics B*, 729:221–234, November 2005. doi: 10.1016/j.nuclphysb.2005.09.041.

F. Matteucci, D. Romano, and P. Molaro. Light and heavy elements in the galactic bulge. *Astron. Astrophys.*, 341:458–468, January 1999.

Patrick McDonald, Jordi Miralda-Escudé, Michael Rauch, Wallace LW Sargent, Tom A Barlow, and Renyue Cen. A measurement of the temperature-density relation in the intergalactic medium using a new lyα absorption-line fitting methodthe observations were made at the wm keck observatory, which is operated as a scientific partnership between the california institute of technology and the university of california; it was made possible by the generous support of the wm keck foundation. *The Astrophysical Journal*, 562(1):52, 2001.

I. D. McGreer, A. Mesinger, and V. D'Odorico. Model-independent evidence in favour of an end to reionization by z $\approx$ 6. *MNRAS*, 447:499–505, February 2015. doi: 10.1093/mnras/stu2449.

Matthew McQuinn, Adam Lidz, Matias Zaldarriaga, Lars Hernquist, Philip F Hopkins, Suvendra Dutta, and Claude-André Faucher-Giguère. He ii reionization and its effect on the intergalactic medium. *The Astrophysical Journal*, 694(2): 842, 2009.

D. C. Morton. Atomic data for resonance absorption lines. I - Wavelengths longward of the Lyman limit. *ApJS*, 77:119–202, September 1991. doi: 10.1086/191601.

ME Mosquera and O Civitarese. Calculation of primordial abundances of light nuclei including a heavy sterile neutrino. *Journal of Cosmology and Astroparticle Physics*, 2015(08):038, 2015.

K. M. Nollett and G. P. Holder. An analysis of constraints on relativistic species from primordial nucleosynthesis and the cosmic microwave background. *ArXiv e-prints*, December 2011.

P Noterdaeme, P Petitjean, C Ledoux, R Srianand, and A Ivanchik. Hd molecules at high redshift-a low astration factor of deuterium in a solar-metallicity dla system at z= 2.418. *Astronomy & Astrophysics*, 491(2):397–400, 2008.

P. Noterdaeme, S. López, V. Dumont, C. Ledoux, P. Molaro, and P. Petitjean. Deuterium at high redshift. Primordial abundance in the $z_{abs} = 2.621$ damped Ly-α system towards CTQ 247. *A&A*, 542:L33, June 2012. doi: 10.1051/0004-6361/201219453.

Keith A Olive, Patrick Petitjean, Elisabeth Vangioni, and Joseph Silk. Higher d or li: probes of physics beyond the standard model. *Monthly Notices of the Royal Astronomical Society*, 426(2):1427–1435, 2012.

J. M. O'Meara, D. Tytler, D. Kirkman, N. Suzuki, J. X. Prochaska, D. Lubin, and A. M. Wolfe. The Deuterium to Hydrogen Abundance Ratio toward a Fourth QSO: HS 0105+1619. *Astrophys. J.*, 552:718–730, May 2001. doi: 10.1086/320579.

J. M. O'Meara, S. Burles, J. X. Prochaska, G. E. Prochter, R. A. Bernstein, and K. M. Burgess. The Deuterium-to-Hydrogen Abundance Ratio toward the QSO SDSS J155810.16-003120.0. *Astrophys. J., Lett.*, 649:L61–L65, October 2006. doi: 10.1086/508348.

D. E. Osterbrock, R. T. Waters, T. A. Barlow, T. G. Slanger, and P. C. Cosby. Faint Emission Lines in the Blue and Red Spectral Regions of the Night Airglow. *PASP*, 112:733–741, May 2000. doi: 10.1086/316568.

C. Péroux, R. G. McMahon, L. J. Storrie-Lombardi, and M. J. Irwin. The evolution of Ω_{HI} and the epoch of formation of damped Lyman α absorbers. *MNRAS*, 346: 1103–1115, December 2003. doi: 10.1111/j.1365-2966.2003.07129.x.

M. Pettini and D. V. Bowen. A New Measurement of the Primordial Abundance of Deuterium: Toward Convergence with the Baryon Density from the Cosmic Microwave Background? *Astrophys. J.*, 560:41–48, October 2001. doi: 10.1086/322510.

M. Pettini, B. J. Zych, M. T. Murphy, A. Lewis, and C. C. Steidel. Deuterium abundance in the most metal-poor damped Lyman alpha system: converging on $\Omega_{b,0}\mathrm{h}^2$. *Mon. Not. R. Astron. Soc.*, 391:1499–1510, December 2008a. doi: 10.1111/j.1365-2966.2008.13921.x.

M. Pettini, B. J. Zych, C. C. Steidel, and F. H. Chaffee. C, N, O abundances in the most metal-poor damped Lyman alpha systems. *Mon. Not. R. Astron. Soc.*, 385:2011–2024, April 2008b. doi: 10.1111/j.1365-2966.2008.12951.x.

Planck Collaboration. Planck 2015 results. XIII. Cosmological parameters. *ArXiv e-prints*, February 2015.

N. Prantzos. The evolution of D and ˆ3ˆHe in the Galactic disk. *Astron. Astrophys.*, 310:106–114, June 1996.

William H Press, George B Rybicki, and Donald P Schneider. Properties of high-redshift lyman alpha clouds i. statistical analysis of the ssg quasars. *arXiv preprint astro-ph/9303016*, 1993.

J. X. Prochaska, S. Herbert-Fort, and A. M. Wolfe. The SDSS Damped Lyα Survey: Data Release 3. *ApJ*, 635:123–142, December 2005. doi: 10.1086/497287.

J Xavier Prochaska and Arthur M Wolfe. On the (non) evolution of hi gas in galaxies over cosmic time. *The Astrophysical Journal*, 696(2):1543, 2009.

Michael Rauch, Jordi Miralda-Escude, Wallace LW Sargent, Tom A Barlow, David H Weinberg, Lars Hernquist, Neal Katz, Renyue Cen, and Jeremiah P Ostriker. The opacity of the lyα forest and implications for ωb and the ionizing backgroundthe observations were made at the wm keck observatory, which is operated as a

scientific partnership between the california institute of technology and the university of california; it was made possible by the generous support of the wm keck foundation. *The Astrophysical Journal*, 489(1):7, 1997.

H. Reeves, J. Audouze, W. A. Fowler, and D. N. Schramm. On the Origin of Light Elements. *Astrophys. J.*, 179:909–930, February 1973. doi: 10.1086/151928.

Massimo Ricotti, Nickolay Y Gnedin, and J Michael Shull. The evolution of the effective equation of state of the intergalactic medium. *The Astrophysical Journal*, 534(1):41, 2000.

S. Riemer-Sørensen, J. K. Webb, N. Crighton, V. Dumont, K. Ali, S. Kotuš, M. Bainbridge, M. T. Murphy, and R. Carswell. A robust deuterium abundance; re-measurement of the z = 3.256 absorption system towards the quasar PKS 1937-101. *MNRAS*, 447:2925–2936, March 2015. doi: 10.1093/mnras/stu2599.

Donatella Romano, Monica Tosi, Cristina Chiappini, and Francesca Matteucci. Deuterium astration in the local disc and beyond. *Monthly Notices of the Royal Astronomical Society*, 369(1):295–304, 2006.

Gwen C. Rudie, Charles C. Steidel, and Max Pettini. The temperature-density relation in the intergalactic medium at redshift z = 2.4. *The Astrophysical Journal Letters*, 757(2):L30, 2012. URL http://stacks.iop.org/2041-8205/757/i=2/a=L30.

J. Schaye, T. Theuns, A. Leonard, and G. Efstathiou. Measuring the equation of state of the intergalactic medium. *MNRAS*, 310:57–70, November 1999. doi: 10.1046/j.1365-8711.1999.02956.x.

J. Schaye, T. Theuns, M. Rauch, G. Efstathiou, and W. L. W. Sargent. The thermal history of the intergalactic medium*. *MNRAS*, 318:817–826, November 2000. doi: 10.1046/j.1365-8711.2000.03815.x.

Joop Schaye. Model-independent insights into the nature of the lyα forest and the distribution of matter in the universe. *Astrophys. J.*, 559(2):507, 2001. URL http://stacks.iop.org/0004-637X/559/i=2/a=507.

D. P. Schneider, X. Fan, P. B. Hall, S. Jester, G. T. Richards, C. Stoughton, M. A. Strauss, M. SubbaRao, D. E. Vanden Berk, S. F. Anderson, W. N. Brandt, J. E. Gunn, J. Gray, J. R. Trump, W. Voges, B. Yanny, N. A. Bahcall, M. R. Blanton, W. N. Boroski, J. Brinkmann, R. Brunner, S. Burles, F. J. Castander, M. Doi, D. Eisenstein, J. A. Frieman, M. Fukugita, T. M. Heckman, G. S. Hennessy, Ž. Ivezić, S. Kent, G. R. Knapp, D. Q. Lamb, B. C. Lee, J. Loveday, R. H.

Lupton, B. Margon, A. Meiksin, J. A. Munn, H. J. Newberg, R. C. Nichol, M. Niederste-Ostholt, J. R. Pier, M. W. Richmond, C. M. Rockosi, D. H. Saxe, D. J. Schlegel, A. S. Szalay, A. R. Thakar, A. Uomoto, and D. G. York. The Sloan Digital Sky Survey Quasar Catalog. II. First Data Release. *AJ*, 126:2579–2593, December 2003. doi: 10.1086/379174.

D. P. Schneider, P. B. Hall, G. T. Richards, M. A. Strauss, D. E. Vanden Berk, S. F. Anderson, W. N. Brandt, X. Fan, S. Jester, J. Gray, J. E. Gunn, M. U. SubbaRao, A. R. Thakar, C. Stoughton, A. S. Szalay, B. Yanny, D. G. York, N. A. Bahcall, J. Barentine, M. R. Blanton, H. Brewington, J. Brinkmann, R. J. Brunner, F. J. Castander, I. Csabai, J. A. Frieman, M. Fukugita, M. Harvanek, D. W. Hogg, Ž. Ivezić, S. M. Kent, S. J. Kleinman, G. R. Knapp, R. G. Kron, J. Krzesiński, D. C. Long, R. H. Lupton, A. Nitta, J. R. Pier, D. H. Saxe, Y. Shen, S. A. Snedden, D. H. Weinberg, and J. Wu. The Sloan Digital Sky Survey Quasar Catalog. IV. Fifth Data Release. *AJ*, 134:102–117, July 2007. doi: 10.1086/518474.

J Michael Shull, Kevin France, Charles W Danforth, Britton Smith, and Jason Tumlinson. Hst/cos observations of the quasar he 2347–4342: Probing the epoch of he ii patchy reionization at redshifts z= 2.4-2.9. *The Astrophysical Journal*, 722(2):1312, 2010.

R. Srianand, N. Gupta, P. Petitjean, P. Noterdaeme, and C. Ledoux. Detection of 21-cm, H_2 and deuterium absorption at $z > 3$ along the line of sight to J1337+3152. *Mon. Not. R. Astron. Soc.*, 405:1888–1900, July 2010. doi: 10.1111/j.1365-2966.2010.16574.x.

G. Steigman. Neutrinos And Big Bang Nucleosynthesis. *ArXiv e-prints*, July 2012.

N. Suzuki, D. Tytler, D. Kirkman, J. M. O'Meara, and D. Lubin. Relative Flux Calibration of Keck HIRES Echelle Spectra. *Publ.. Astron. Soc. Pac.*, 115:1050–1067, September 2003. doi: 10.1086/376849.

Tom Theuns, Joop Schaye, Saleem Zaroubi, Tae-Sun Kim, Panayiotis Tzanavaris, and Bob Carswell. Constraints on reionization from the thermal history of the intergalactic medium. *The Astrophysical Journal Letters*, 567(2):L103, 2002.

M. Tosi, G. Steigman, F. Matteucci, and C. Chiappini. Is High Primordial Deuterium Consistent with Galactic Evolution? *Astrophys. J.*, 498:226–235, May 1998. doi: 10.1086/305524.

J Tumlinson, AL Malec, RF Carswell, MT Murphy, R Buning, N Milutinovic,

SL Ellison, JX Prochaska, RA Jorgenson, W Ubachs, et al. Cosmological concordance or chemical coincidence? deuterated molecular hydrogen abundances at high redshift. *The Astrophysical Journal Letters*, 718(2):L156, 2010.

D. Tytler, X.-M. Fan, and S. Burles. Cosmological baryon density derived from the deuterium abundance at redshift z = 3.57. *Nature*, 381:207–209, May 1996. doi: 10.1038/381207a0.

David Tytler, David Kirkman, John M. O'Meara, Nao Suzuki, Adam Orin, Dan Lubin, Pascal Paschos, Tridivesh Jena, Wen-Ching Lin, Michael L. Norman, and Avery Meiksin. Cosmological parameters σ_8, the baryon density ω_b, the vacuum energy density ω_λ, the hubble constant and the uv background intensity from a calibrated measurement of h i $ly\alpha$ absorption at z = 1.9. *The Astrophysical Journal*, 617(1):1, 2004. URL http://stacks.iop.org/0004-637X/617/i=1/a=1.

David Tytler, Pascal Paschos, David Kirkman, Michael L Norman, and Tridivesh Jena. The effect of large-scale power on simulated spectra of the lyα forest. *Monthly Notices of the Royal Astronomical Society*, 393(3):723–758, 2009.

P. R. Upton Sanderbeck, A. D'Aloisio, and M. J. McQuinn. Models of the thermal evolution of the intergalactic medium after reionization. *MNRAS*, 460:1885–1897, August 2016. doi: 10.1093/mnras/stw1117.

DA Varshalovich, AV Ivanchik, P Petitjean, R Srianand, and C Ledoux. Hd molecular lines in an absorption system at redshift z= 2.3377. *Astronomy Letters*, 27(11):683–685, 2001.

Matteo Viel, Martin G Haehnelt, and Volker Springel. Inferring the dark matter power spectrum from the lyman α forest in high-resolution qso absorption spectra. *Monthly Notices of the Royal Astronomical Society*, 354(3):684–694, 2004.

Matteo Viel, James S Bolton, and Martin G Haehnelt. Cosmological and astrophysical constraints from the lyman α forest flux probability distribution function. *Monthly Notices of the Royal Astronomical Society: Letters*, 399(1):L39–L43, 2009.

S. S. Vogt, S. L. Allen, B. C. Bigelow, L. Bresee, B. Brown, T. Cantrall, A. Conrad, M. Couture, C. Delaney, H. W. Epps, D. Hilyard, D. F. Hilyard, E. Horn, N. Jern, D. Kanto, M. J. Keane, R. I. Kibrick, J. W. Lewis, J. Osborne, G. H. Pardeilhan, T. Pfister, T. Ricketts, L. B. Robinson, R. J. Stover, D. Tucker, J. Ward, and M. Z. Wei. HIRES: the high-resolution echelle spectrometer on the Keck 10-m Telescope. In D. L. Crawford and E. R. Craine, editors, *Instrumentation*

in Astronomy VIII, volume 2198 of *Society of Photo-Optical Instrumentation Engineers (SPIE) Conference Series*, page 362, June 1994.

J. B. Whitmore and M. T. Murphy. Impact of instrumental systematic errors on fine-structure constant measurements with quasar spectra. *MNRAS*, 447:446–462, February 2015. doi: 10.1093/mnras/stu2420.

Jonathan B. Whitmore, Michael T. Murphy, and Kim Griest. Wavelength calibration of the vlt-uves spectrograph. *The Astrophysical Journal*, 723(1):89, 2010. URL http://stacks.iop.org/0004-637X/723/i=1/a=89.

Gábor Worseck, J. Xavier Prochaska, Matthew McQuinn, Aldo Dall'Aglio, Cora Fechner, Joseph F. Hennawi, Dieter Reimers, Philipp Richter, and Lutz Wisotzki. The end of helium reionization at z 2.7 inferred from cosmic variance in hst/cos he ii lyα absorption spectra. *The Astrophysical Journal Letters*, 733(2):L24, 2011. URL http://stacks.iop.org/2041-8205/733/i=2/a=L24.

Zheng Zheng and Jordi Miralda-Escudé. Self-shielding effects on the column density distribution of damped lyα systems. *The Astrophysical Journal Letters*, 568(2): L71, 2002.

Lin Zuo. A semi-analytic method for calculating da evolution. *Astronomy and Astrophysics*, 278:343–350, 1993.